Towards continuum gyrokinetic study of high-field mirrors

M. Francisquez,[1] M. H. Rosen,[2] N. R. Mandell,[1] A. Hakim,[1] C. B. Forest,[3] and G. W. Hammett[1]
[1)]*Princeton Plasma Physics Laboratory, Princeton, NJ 08540, USA.*
[2)]*Department of Astrophysics Sciences, Princeton University, Princeton, NJ 08540 USA.*
[3)]*Department of Physics, University of Wisconsin-Madison, Madison, WI 53706, USA.*

(*Electronic mail: mfrancis@pppl.gov)

High-temperature superconducting (HTS) magnetic mirrors under development exploit strong fields with high mirror ratio to compress loss cones and enhance confinement, and may offer cheaper, more compact fusion power plant candidates. This new class of devices could exhibit largely unexplored interchange and gradient-driven modes. Such instabilities, and methods to stabilize them, can be studied with gyrokinetics given the strong magnetization and prevalence of kinetic effects. Our focus here is to: a) determine if oft-used gyrokinetic models for open field lines produce the electron-confining (Pastukhov) electrostatic potential; b) examine and address challenges faced by gyrokinetic codes in studying HTS mirrors. We show that a one-dimensional limit of said models self-consistently develops a potential qualitatively reaching the analytical Pastukhov level. Additionally, we describe the computational challenges of studying high mirror ratios with open field line gyrokinetic solvers, and offer a force softening method to mitigate small time steps needed for time integration in colossal magnetic field gradients produced by HTS coils, providing a 19X speedup.

I. MOTIVATION & BACKGROUND

The world's energy needs, the time scale on which clean energy sources are needed, and existing financial structures all favor fusion power plants that can be deployed quickly in the coming decades and with the lowest possible capital cost[1]. This ecosystem has incentivized R&D of tokamaks[2] and stellarators[3,4] that use emerging technologies and manufacturing techniques to shorten the time frame and reduce the cost of bringing fusion energy to the grid. Non-toroidal devices striving to achieve similar goals with less time and fewer resources are also being explored. One such candidate is the axisymmetric magnetic mirror, a device consisting primarily of two coils cylindrically aligned to magnetically confine a plasma between them. Recent years have seen renewed interest in mirror-based fusion due to a number of reasons (see [5–9] and references therein), some of which we briefly review here. Amongst them is the realization of magnetohydrodynamic (MHD) stability and keV electron temperatures in one such mirror, the Gas Dynamic Trap (GDT) at the Budker Institute[5,10]. These findings have also coincided with the arrival of new heating and superconducting technologies, motivating new proposals for mirror-based fusion[7].

Amongst the technological advances modern mirrors can exploit is the emergence of high-temperature superconductors (HTS) based on REBCO tapes[11]. HTS coils can operate at higher temperatures and current density, both desirable in fusion applications, and generate much stronger magnetic fields, which in the context of the mirror means smaller loss cones and synergistic operation with modern RF heating systems. These are some of the advantages the Wisconsin HTS Axisymmetric Mirror (WHAM), now under construction at the University of Wisconsin, intends to leverage as it demonstrates the operation of an HTS mirror. WHAM will consist of two HTS coils ≈2 m apart, producing magnetic fields with a peak amplitude of ≈17 T; field lines extend past the coils to expander regions where they flare out.

Along this magnetic field, an electric field that confines the electrons and mitigates parallel particle and heat losses is expected to appear, as in previous mirrors[12]. This "ambipolar" field results from light and collisional electrons in the mirror rapidly scattering into velocity space loss cones and attaining velocities that allow them to escape to the expander and eventually collide with the wall. The ions, however, stay behind because they are heavy and slow, and scatter much more slowly into the loss cone; hence a positive potential begins to build in the plasma. This rising potential increasingly decelerates outgoing electrons and accelerates the ions, and is arrested when a quasineutral equilibrium with equal ion and electron particle fluxes (ambipolarity) is reached. Analytical calculations of the particle loss rates, and the potential to support them, were first done by Pastukhov[13] and soon after corrected by others[14,15]. They consisted of approximate solutions to the kinetic equation with the Landau/Rosenbluth collision operator (LRO), using a simplified bounce averaging with a step-function magnetic field model and neglecting expanders. Despite their simplifications, the resulting potential drops ($\Delta\phi$) from the center of the plasma to the location with the maximum magnetic field amplitude (the mirror throat) of $e\Delta\phi/T_e \sim 4-5$ overlapped with contemporaneous numerical calculations giving $e\Delta\phi/T_e \sim 4-6$ (T_e is the electron temperature)[12,16,17]. Since then, many other experimental[6,18–22], numerical and semi-analytic[23–25] studies have characterized the ambipolar potential in similar or related scenarios. They generally find $e\Delta/T_e \sim 1-6$, although the precise height and shape of the ambipolar potential depend on numerous factors such as mirror ratio, confinement scheme, plasma parameters, geometry, and heating methods. The presence of high-energy "sloshing ions" produced by oblique neutral beam incidence can also modify the potential since their more distant turning points cause the density to peak off-center[5]. Amongst such previous works one stands out for contributing a particularly relevant semi-analytic calculation using WHAM parameters, finding $e\Delta\phi/T_e \approx 5-6$[25].

In addition to developing a sufficiently strong ambipolar potential to diminish the electron parallel particle and energy transport, mirrors have to mitigate several other phenomena that can degrade confinement. For example, there are gradient-driven drift modes like electron and ion temperature-

gradient modes (ETG, ITG) and trapped particle modes. These lower frequency modes produce transport across field lines and deteriorate confinement. Most worryingly owing to its short, microsecond time scale, is the severe interchange flute instability caused by the charge separation induced by the azimuthal ∇B drift of ions and electrons and its resulting $E \times B$ drift that reinforces initial azimuthal perturbations. Strategies like good-curvature[5], kinetic[26], active feedback[27] and vortex[28] stabilization have been developed to suppress this mode's growth. The latter uses electrical biasing between a ring limiter in the plasma and concentric rings at the far end of the expander to generate radially sheared azimuthal flows. These flows can suppress the growth of radial perturbations in the same way shear-flow stabilization does in tokamaks[29], or similar to how biasing-induced azimuthal flows reduce cross-field transport in LAPD[30]. In contrast to tokamaks, where reduction of ITG heat transport by flow shearing is done indirectly via a complex relationship between actuators and turbulence, a potential advantage of the mirror is that these flows may be tailored directly via end-plate biasing.

The effectiveness of biasing in controlling interchange and ITG modes and the expected magnitude of the turbulent cross-field transport produced by these and other low-frequency instabilities is not well characterized in WHAM or other future HTS mirrors. Luckily the tokamak community has spent decades maturing computational tools that can allow us to explore these phenomena through, for example, continuum[31–34] and PIC[35,36] gyrokinetic[37] simulation. These codes may be capable of providing a first-principles estimation of the microinstability characteristics and the effects end-plate biasing has on them. Their design, however, was not meant for an HTS mirror environment where, for example, magnetic fields are open-ended and have large parallel gradients. Luckily in recent years, the `Gkeyll` code[38] pioneered continuum gyrokinetic modeling in open field lines, which may provide a sound foundation on which to build capabilities to perform first-principles simulations of low-frequency turbulence in HTS mirrors akin to the way the community has for tokamaks in the last 20 years. A hint at what this may look like can be seen in `Gkeyll` simulations of LAPD in which biasing was shown to reduce cross-field turbulent transport[39].

Hence, in this work, we explore two stepping-stone issues toward achieving predictive capability over HTS mirror turbulence. The first issue is whether the gyrokinetic model in the `Gkeyll` code (also present in other gyrokinetic codes[40,41]) is consistent with and capable of producing the Pastukhov ambipolar potential, an essential requirement for mirror-based fusion since electron parallel heat losses need to be curtailed. We point out that the main subject of a gyrokinetic code like `Gkeyll` is short time scale turbulence, rendering it inefficient at calculating the Pastukhov potential, which evolves and saturates on a much longer time scale. A bounce-averaged code is much faster for this task, but demonstrating that a gyrokinetic model is consistent with the Pastukhov potential and qualitatively reproduces it on a shorter time scale is an important initial test. The second issue concerns the computational challenges brought about by the HTS mirror environment, to which tokamak-oriented codes would need to adapt and develop solutions to. Examples include extreme time step constraints from the colossal mirror force, and the high mirror ratio that increases resolution requirements and compute time (e.g. a mirror ratio of 20 requires increasing the velocity-space resolution by about a factor of 20 to resolve the loss cone). These topics are addressed in the following sections: section II introduces the physics models employed in this work, section III describes some of the computational challenges in carrying out continuum gyrokinetic simulations of an HTS mirror, section IV presents our results, and section V summarizes this work.

II. EQUILIBRIUM & GYROKINETIC MODELS USED

The simulations presented in the next section are produced with the following model magnetic equilibrium and three different kinetic models, each detailed in this section.

A. Magnetic equilibrium model

We use a model magnetic mirror that resembles the proposed WHAM experiment, including the expanders where flux expansion and good magnetic curvature occur. This model magnetic equilibrium is composed of a radial and an axial component, $\boldsymbol{B} = B_R\hat{\boldsymbol{R}} + B_Z\hat{\boldsymbol{Z}}$, each of which is given by a magnetic flux function $\psi(R,Z)$ as $B_R = -(1/R)\partial_Z\psi$ and $B_Z = (1/R)\partial_R\psi$. In our model, the magnetic flux function consists of a double Lorentzian:

$$\psi = \frac{R^2\mathscr{B}}{2\pi\gamma}\left\{\left[1+\left(\frac{Z-Z_m}{\gamma}\right)^2\right]^{-1} + \left[1+\left(\frac{Z+Z_m}{\gamma}\right)^2\right]^{-1}\right\}, \tag{1}$$

which has a good description of the field between mirror coils but is less accurate in the expanders. This simple three-parameter model ($\mathscr{B}$ controls the strength of the magnetic field, γ the width of the of the peaks and $\pm Z_m$ the location of the coils) was tuned to generate a magnetic field similar to that aimed for WHAM. The resulting field lines and magnetic field magnitudes in the R-Z plane are shown in figure 1(a) for the parameters $\{\mathscr{B},\gamma,Z_m\} = \{6.51292, 0.124904, 0.98\}$, and can be compared with those obtained by the Pleiades code[42] in figure 1(b). The field is quite similar in the central region where the plasma is confined, but this Lorentzian model does not precisely capture the curvature of the field lines in the expanders. The on-axis field is shown in figure 1(c), illustrating that this model is reasonable as a first step in this study. Comparison of several equilibrium metrics for the Pleiades-computed field and the model used here is given in table I. The $R_m = B_m/B_p = 32$ mirror ratio for our model, although higher than the $R_m = 20$ in the Pleiades calculation, is within the $R_m = 20-50$ range that WHAM plans to explore so we did not try to improve this field further at this time. Note that this $R_m = 32$ is significantly higher than other recent mirror simulations[23,24,43]. A bigger discrepancy exists in the magnetic field at the expander wall ($B(Z = \pm L/2) = B_w$), `Gkeyll`'s being is 2.6 times larger than Pleiades' and larger than what will

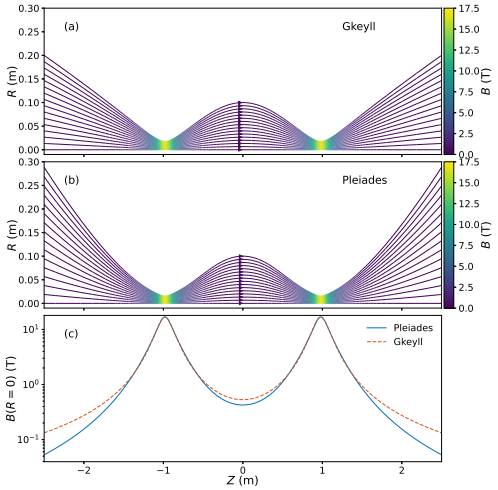

FIG. 1. Comparison of equilibrium magnetic field in the model used in `Gkeyll` (a) and as computed by the Pleiades code for the coils in WHAM (b). The magnetic field on axis given by the model is very similar to that in the planned experiment (c).

TABLE I. Mirror equilibrium in WHAM compared to our model

parameter	description	WHAM	`Gkeyll`
L	Machine length	5 m	5 m
L_m	Distance between mirror coils	1.8 m	1.96 m
a_m	Mirror radius (at mirror coils)	0.0275 m	0.018 m
a_p	Plasma radius	0.1 m	0.1 m
a_w	Expander radius at wall	0.35 m	0.2 m
B_m	Mirror field strength	17 T	17.016 T
B_p	Plasma field strength	0.85 T	0.53 T
B_w	Field strength at expander wall	0.05 T	0.1327 T

be found on WHAM. In the future we will perform studies with more accurate magnetic fields computed by Pleiades or other equilibrium tools.

B. Gyrokinetic models

`Gkeyll`[38] solves a long-wavelength full-f gyrokinetic model, either electrostatic or electromagnetic (i.e. with $\boldsymbol{B}_\perp$ fluctuations[44]), to determine the evolution of the distribution function of species s, $f_s(\boldsymbol{x}, v_\parallel, \mu, t)$, as a function of time t, guiding-center position $\boldsymbol{x} = (x, y, z)$, velocity parallel to the background magnetic field $v_\parallel$ and magnetic moment $\mu = m_s v_\perp^2/(2B)$. The model evolves f_s by solving

$$\frac{\partial B_\parallel^* f_s}{\partial t} + \nabla \cdot B_\parallel^* \dot{\boldsymbol{x}} f_s + \frac{\partial}{\partial v_\parallel}\left(B_\parallel^* \dot{v}_\parallel f_s\right) = B_\parallel^* C[f_s] + B_\parallel^* S_s \quad (2)$$

in the electrostatic limit, where $\boldsymbol{B}^* = \boldsymbol{B} + (m_s v_\parallel/q_s)\nabla \times \hat{\boldsymbol{b}}$ and we approximate $B_\parallel^* = \hat{\boldsymbol{b}} \cdot \boldsymbol{B}^* \approx B$. The terms $C[f_s]$ and S_s stand for collisions and sources, respectively. Collisions are modeled via a Dougherty operator[45], which has been improved to better model multispecies collisions[46]. The phase-space characteristics are defined by $\dot{\boldsymbol{x}} = \{\boldsymbol{x}, H\}$ and $\dot{v}_\parallel = \{v_\parallel, H\}$ in terms of the Poisson bracket

$$\{F, G\} = \frac{\boldsymbol{B}^*}{m_s B_\parallel^*} \cdot \left(\nabla F \frac{\partial G}{\partial v_\parallel} - \nabla G \frac{\partial F}{\partial v_\parallel}\right) - \frac{\hat{\boldsymbol{b}}}{q_s B_\parallel^*} \times \nabla F \cdot \nabla G, \quad (3)$$

and the Hamiltonian

$$H = \frac{1}{2} m_s v_\parallel^2 + \mu B + q_s \phi - \frac{1}{2} m_s |\boldsymbol{v}_{\boldsymbol{E}}|^2 \quad (4)$$

including the higher order term associated with the kinetic energy due to $E \times B$ drifts[47,48] of velocity $\boldsymbol{v}_{\boldsymbol{E}} = \boldsymbol{E} \times \hat{\boldsymbol{b}}/B$.

The gyrokinetic evolution described by equations 2-4 is coupled to the long-wavelength Poisson equation (i.e. quasineutrality) given by

$$-\nabla \cdot \sum_s \frac{n_s m_s}{B^2} \nabla_\perp \phi = \sum_s q_s n_s \quad (5)$$

where we refer to n_s as the guiding center number density, defined as the zeroth velocity moment of f_s: $n_s = \int \mathrm{d}\boldsymbol{w}\, B_\parallel^* f_s$ with $\mathrm{d}\boldsymbol{w} = (2\pi/m_s)\mathrm{d}v_\parallel\, \mathrm{d}\mu$. In general, the spatially and time-dependent density is used in the left side of equation 5, in contrast to the linearized polarization density or Boussinesq approximation commonly employed in other full-f gyrokinetic[40] and fluid[49] codes. The last term in the Hamiltonian (equation 4) is kept to guarantee energy conservation when the Boussinesq approximation is not made, demonstrated in the 1D limit in appendix A.

The model given by equations 2-5 is cast in field-aligned coordinates, which in this case, we choose to be the equilibrium magnetic flux ψ, the azimuthal angle θ and the length along the field line ℓ, i.e. our guiding center coordinates are $\boldsymbol{x} = (x, y, z) = (\psi, \theta, \ell)$. `Gkeyll` requires that we provide the mapping $\boldsymbol{X}(\boldsymbol{x})$ from field-aligned $(\boldsymbol{x})$ to Cartesian $(\boldsymbol{X} = (X, Y, Z))$ coordinates, from which the metric coefficients $g_{ij} = (\partial \boldsymbol{X}/\partial u^i) \cdot (\partial \boldsymbol{X}/\partial u^j)$ (for $u^i \in \{x, y, z\}$) and the position-space Jacobian J are computed using automatic differentiation routines in the SciLua package[50]. Given our choice of (ψ, θ) (or (x, y)), $R(x, Z)$ can be obtained by inverting equation 1. Lastly, we obtained the mapping $Z(\boldsymbol{x})$ for a given (x, y) by considering the field line equation $\mathrm{d}(\boldsymbol{X}(z))/\mathrm{d}z|_{\text{along } B} = \boldsymbol{B}/B$ which after dotting with $\hat{\boldsymbol{Z}}$ can be rearranged into

$$z(Z) = \int_0^Z \mathrm{d}s \frac{B(x, s)}{B_Z(s)}. \quad (6)$$

In general, the solution to this equation may not be analytic, but we integrate and invert it numerically to obtain $Z(\boldsymbol{x})$.

Although our ultimate goal is to study the three-dimensional dynamics of WHAM, in this work, we constrain ourselves to a one-dimensional exploration of parallel dynamics along a single field line across the entire machine. Our

TABLE II. Reference plasma parameters used in simulations

parameter	description	value
n_0	Number density	3×10^{19} m^{-3}
T_{e0}	Electron temperature	940 eV
T_{i0}	Ion temperature	8.361 keV
m_i	Ion mass	$m_{\text{deuterium}}$

scope is thus more comprehensive than previous ones that only focused on "nozzles" or a single coil region[23,24,51]. We solve a 1D limit of the above model on the field line going through $(R,Z)=(0.1\,\text{m},0)$, where the evolution of the distribution function $f_s(z,v_\parallel,\mu,t)$ is given by

$$\frac{\partial B_\parallel^* f_s}{\partial t}+\frac{1}{J}\frac{\partial}{\partial z}\left(JB_\parallel^*\dot{z}f_s\right)+\frac{\partial}{\partial v_\parallel}\left(B_\parallel^*\dot{v}_\parallel f_s\right)=B_\parallel^* C[f_s]+B_\parallel^* S_s, \tag{7}$$

the Jacobian J is now evaluated at $(\psi(R=0.1\,\text{m}),\theta=0)$, and the guiding-center equations of motion are now obtained with the simpler Poisson bracket

$$\{F,G\}=\frac{1}{m_s JB_\parallel^*}\left(\frac{\partial F}{\partial z}\frac{\partial G}{\partial v_\parallel}-\frac{\partial G}{\partial z}\frac{\partial F}{\partial v_\parallel}\right). \tag{8}$$

The kinetic equation in this 1D limit is often referred to as the drift-kinetic equation; we continue to call it the gyrokinetic equation because it is a 1D limit of our higher dimensional (long-wavelength) gyrokinetic model and because, as it is shown below, we use a Poisson equation to obtain the electrostatic potential as one does in higher dimensional gyrokinetics.

As a starting point, we only consider the study of the thermal plasma with the reference parameters in table II and do not directly model beam ions; this is because the use of ∼25 keV neutral beams introduces an energetic sloshing population that is more computationally expensive to account for. Sloshing ions modify the potential profile due to their off-center peaked density, as mentioned in section I, and although we have ideas on how we will mitigate this expense in the future, we first want to understand the challenges associated with the thermal population and explore the Pastukhov potential formation for which the beam ions are not essential. For now we use a particle and heat source at the center of the field line to mimic the combined effect of beam ions slowing down on the thermal population, ionization particle sources and microwave heating. Such source has the following shape:

$$S_s(z)=\frac{\mathscr{N}}{(2\pi\mathscr{T}_s/m_s)^{3/2}}\exp\left(-\frac{v_\parallel^2+2\mu B}{2\mathscr{T}_s/m_s}\right), \tag{9}$$

and uses the source density rate and temperature

$$\mathscr{N}=\begin{cases}\max\left(\mathscr{N}_{\text{floor}},\ \frac{\mathscr{N}_0}{\sqrt{2\pi\sigma^2}}e^{-z^2/(2\sigma^2)}\right) & |Z|\le Z_m\\ \mathscr{N}_{\text{floor}} & |Z|>Z_m\end{cases} \tag{10}$$

$$\mathscr{T}_s=\begin{cases}\mathscr{T}_{s0} & |z|\le 2\sigma\\ \mathscr{T}_{\text{floor},s} & |z|>2\sigma\end{cases} \tag{11}$$

with the following parameters: $\mathscr{N}_{\text{floor}}=10^{-16}\,\text{m}^{-3}\text{s}^{-1}$, $\mathscr{N}_0=3.96\times10^{22}\ \text{m}^{-3}\text{s}^{-1}$, $\sigma=Z_m/4$, $\mathscr{T}_{\text{floor},s}=\mathscr{T}_{s0}/8$, $\mathscr{T}_{s0}=1.25T_{s0}$. The small density source floor ($\mathscr{N}_{\text{floor}}$) is included to reduce the risk of having negative distribution functions, which the code does not forbid. Still, we try to keep it at sufficiently low levels so it does not affect the physics results. For example, in simulations presented in section IV less than 5% of cells had a distribution function with an amplitude lower than -10^{-8} times the maximum (positive) distribution at that location in z; moreover, all velocity moments that should be positive (e.g. density, temperature) are indeed positive at all locations.

In addition to sources, the right side of the kinetic equation 7 includes a collision term that, in this study, only accounts for intra-species collisions, using a spatially constant and time-independent collision frequency[52] computed using the reference parameters in table II. Future studies will include the effect of multispecies collisions with an improved Dougherty operator[46]. Additionally, the homogeneous collisionality causes the expanders to be more collisional than they should be since $\nu_s\propto n_s/T_s^{3/2}$ and the density drops precipitously there, but that is something we could relax in future work. Perhaps the fact that our simplified operator lacks the $1/v^3$ dependence of the LRO is of greater importance; more precisely, the pitch-angle scattering part of the Dougherty operator corresponds to a collision frequency scaling as $1/v^2$ instead of the $1/v^3$ scaling in the LRO[53]. Such scaling leads to somewhat larger scattering rates at high energies and different equilibrium potentials. Improving the model to incorporate the $1/v^3$ scaling and implementing the LRO are subjects of ongoing work.

Alongside the Dougherty operator, the sources in equations 9-11 complete the definition of the kinetic equation we evolve. Integration, however, also requires boundary (BCs) and initial (ICs) conditions. As for BCs, the field line in our domain terminates at the sheath entrance since the sheath is a non-neutral region beyond the scope of gyrokinetics. At this location, we apply a conducting sheath BC[54], in which the potential ϕ is determined by the field model (below) and particles with $m_s v_\parallel^2/2<-q_s\phi$ are reflected (assuming zero wall potential) while the rest are absorbed by the wall. At velocity space boundaries, we apply zero-flux BCs, as needed for our model, to conserve moments of f_s. Such BCs are applied in every step from $t=0$, at which time we begin from Maxwellian ICs (see figure 2) with the following moments:

$$n_s(z,t=0)=A(z;n_0,n_m), \tag{12}$$

$$T_s(z,t=0)=A(z;T_{s0},T_{sm}), \tag{13}$$

$$u_{\parallel s}(z,t=0)=c_{sm}\,z/z_m \tag{14}$$

in terms of the helper functions

$$A(z;h_0,h_m)=\begin{cases}h_0 L(z) & |Z|\le Z_{bt},\\ h_0 L(z)^5 & Z_{bt}<|Z|\le Z_m,\\ h_m\sqrt{B(z)/B_m} & Z_m<|Z|,\end{cases} \tag{15}$$

$$L(z)=1-\left[\left(R(z)-R_{bt}\right)/a_{\text{lim}}\right]^2. \tag{16}$$

The function $A(z;h_0,h_m)$ is chosen such that the density increases from $(R=0.1\,\text{m},Z=0)$, where we assume parti-

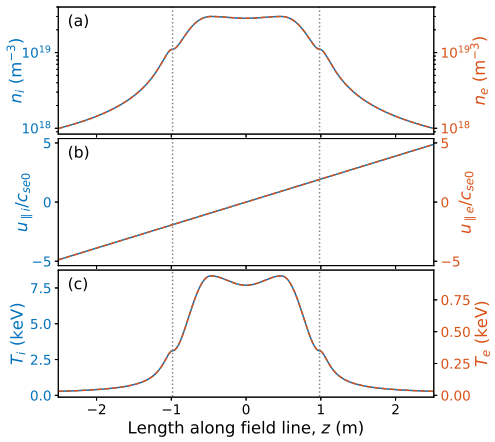

FIG. 2. Initial number density (a), parallel drift speed (b) normalized to $c_{se0} = \sqrt{T_{e0}/m_i}$, and temperature (c) for ions (solid blue) and electrons (dashed orange).

cles are injected at a 45-degree angle, towards the turning point of trapped orbits at ($R_{bt} = 0.07\,\mathrm{m}, Z_{bt} = 0.47\,\mathrm{m}$), where $B(z) = 2B_p$ (from conservation of kinetic energy and μ). A limiter radius of $a_{\mathrm{lim}} = 0.125\,\mathrm{m}$ is assumed. The profiles in the expander would preferably follow the ratio $B(z)/B_p$ rather than its square root, but the latter was chosen to ease numerical transients earlier in the simulation; $A(z;h_0,h_m)$ in $Z_{bt} < |Z| \leq Z_m$ is simply chosen as a polynomial connection between the other two regions. These profiles give initial densities and temperatures at the mirror throats given by n_m and T_{sm}, respectively, from which one can define the parameter $c_{sm} = \sqrt{T_{em}(1+T_{i0}/T_{e0})/m_i}$. We note that these are only simple choices for a first attempt at this problem to limit the severity of initial transients. They are lacking in notably two ways: first, they lead to $\phi(t=0) = 0$ in the kinetic electron case via field models in sections II B 1-II B 2 while we know to expect a potential several T_e/e at equilibrium, and second, the Maxwellian velocity dependence does not incorporate some basic kinetic expectations such as anisotropy and loss cones. Future simulations will use improved ICs as discussed in section III C.

Lastly, to close the model in equations 7-11 a field equation for ϕ is needed. Three different field models were employed to build confidence in the results and for computational reasons explained in section III. We also tried to use a fourth, zero-current field model akin to what was originally proposed for kinetic MHD[55], where the parallel electric field is obtained via a sum of the first moment of our kinetic equations 7 and assuming vanishing parallel currents. This model results in the field equation:

$$-\sum_s \frac{q_s^2 n_s}{m_s B_\parallel^*}\frac{\partial \phi}{\partial z} = \sum_s q_s \left[\frac{\partial}{\partial z}\left(\frac{M_{2\parallel s}}{B_\parallel^*}\right) + \frac{1}{2B}\frac{\partial B}{\partial z}\frac{M_{2\perp s}}{B_\parallel^*}\right], \tag{17}$$

with the moments

$$\begin{aligned} M_{2\parallel s} &= \int \mathrm{d}\boldsymbol{w}\; v_\parallel^2 B_\parallel^* f_s, \\ M_{2\perp s} &= \int \mathrm{d}\boldsymbol{w}\; (2\mu B/m_s) B_\parallel^* f_s. \end{aligned} \tag{18}$$

Similar approaches have been used in previous modeling of a tokamak scrape-off layer[56,57]. However, we did not find a stable numerical method for integrating the gyrokinetic model with this field equation. Two challenges with this approach are that: a) equation 17 was implemented in a cell-wise sense, which is not consistent with the weak form of the gyrokinetic equation coupling three cells in each direction and using an upwind numerical flux, and b) energy conservation requires that exact preservation of quasineutrality ($n_e = n_i$), which discretely may not be the case unless special precautions are taken. An in-depth discussion of these difficulties, and their solutions are beyond the scope of this manuscript. For the moment, we have proceeded with the three field models described below because they worked and represent challenges that persist in 3D, which we wish to first understand and overcome in 1D.

1. *Kinetic e⁻ with linear polarization*

In the spirit of taking a 1D limit of our long-wavelength gyrokinetic model, we create a proxy of the quasineutrality equation 5 by replacing the nablas with a user-defined $ik_\perp$ parameter. This is an approach that has been used in, for example, explorations of an ELM pulse in the scrape-off layer of tokamaks[58]. Later, we also show a scan of the assumed value of $k_\perp$. Furthermore, we use a linear polarization or Boussinesq approximation to replace the n_s/B^2 factor in the polarization density with the homogeneous, constant value n_0/B_p^2. Therefore in this field model, we compute the potential using

$$k_\perp^2 \sum_s \frac{n_0 m_s}{B_p^2}\phi = \sum_s q_s n_s. \tag{19}$$

The use of constant factors in the polarization density appears in other full-f gyrokinetic codes[40], and is often done to simplify, amongst other things, the linear solver required for this operation (i.e. the stiffness or left-side matrix becomes time-independent and is only factorized once). When this field model is used, we also drop the last term in equation 4, as it is not needed to have a consistent, energy preserving scheme (see appendix A).

2. *Kinetic e⁻ with nonlinear polarization*

When the constraint on the time step needed for time integration due to mirror forces is mitigated, the time step can

then be set by the ω_H or electrostatic shear Alfvén mode (see section III). In order to ameliorate such constraint while continuing to obtain sufficiently high potential profiles, we tried to use a field model similar to that in equation 19 but with a larger $k_\perp$ and keeping the spatial and temporal dependence of the density factor in the polarization density. That is, the potential was obtained from

$$k_\perp^2 \sum_s \frac{n_s m_s}{B_p^2}\phi = \sum_s q_s n_s. \tag{20}$$

For the model to conserve energy, the $E\times B$ energy term in the Hamiltonian needs to be kept (equation 4) and computed using $|\boldsymbol{v}_{\boldsymbol{E}}|^2 = (k_\perp\phi/B_p)^2$ (see appendix A). For higher accuracy, one could also keep the spatial dependence of $B(z)$ and $k_\perp(z)$, using a proxy model $k_\perp \sim \pi/a(z) \propto \sqrt{B(z)}$, where a is the plasma minor radius. But the dominant variation in the polarization term is the density's, as we will see in section IV, so we used $k_\perp/B^2 = $ constant for now.

3. Boltzmann, isothermal e^- with ambipolar sheath

This model follows earlier work[58], which assumes that electrons have Boltzmann behavior and are isothermal, such that when we impose ambipolarity at the sheath entrance (equality of electron and ion particle fluxes), one obtains an equation for the sheath potential

$$\phi_s = \phi(z=\pm L_z/2) = \frac{T_{e0}}{e}\ln\left(\frac{n_i v_{te0}}{\sqrt{2\pi}\Gamma_i}\right)\bigg|_{z=\pm L_z/2} \tag{21}$$

in terms of the kinetic ion fluxes (Γ_i) at the sheath entrances $z=\pm L_z/2$ for the computational domain $z\in[-L_z/2, L_z/2]$. Equation 21 assumed quasineutrality and used $v_{te0}^2 = T_{e0}/m_e$. Having obtained the sheath potential, quasineutrality and a Boltzmann electron response, $n_e = C\exp[e(\phi-\phi_s)/T_{e0}]$ (where C is a constant determined by $n_i(z=\pm L_z/2) = n_e(z=\pm L_z/2)$), combine assuming zero wall potentials to produce the field equation

$$\phi = \phi_s + \frac{T_{e0}}{e}\ln\left(\frac{n_i}{n_{is}}\right), \tag{22}$$

where n_{is} is the ion density at the sheath entrance. Only the ion gyrokinetic equation is evolved in this model, increasing the time step needed in time integration by roughly a factor of $\sqrt{m_i/m_e}\sim 60$ and making the calculations much cheaper.

Note that electrons trapped inside the mirror bounce back and forth many times and are confined long enough to thermalize, developing a Maxwellian velocity dependence and exhibiting a Boltzmann response to the potential. But in the expander f_e has a significant beam-like population of cold electrons that escaped the mirror. Electrons in this region thus have a non-Maxwellian character and may reach the wall before they have time to thermalize; i.e. the expanders are collisionless and not expected to follow a Maxwellian distribution[59]. Furthermore, even inside the mirror the electron temperature is expected to drop precipitously near the throat, and hence the isothermal electron assumption is likely to cause further departures from the more realistic kinetic electron case. The validity of this Boltzmann electron model is thus limited, and we merely employ it as a tool to make iterative exploration possible (given its lower cost) and to help us understand the computational challenges of modeling ion dynamics in high-field mirrors.

III. COMPUTATIONAL CHALLENGES AND TECHNIQUES

The gyrokinetic model in equations 7-16 with the field models in sections II B 1-II B 3 are discretized with a discontinuous Galerkin (DG) method and time-integrated with an explicit strong-stability-preserving third order Runge-Kutta scheme in the `Gkeyll` code[38]. The spatial discretization is carried out on a multidimensional, uniform grid over the domain $(z, v_\parallel, \mu)\in[-L_z/2, L_z/2]\times\left[-v_{\parallel\max}, v_{\parallel\max}\right]\times[0,\mu_{\max}]$ using $N_z\times N_{v_\parallel}\times N_\mu$ cells with a piecewise polynomial basis of order p within each cell. We will primarily discuss results obtained with $(N_z, N_{v_\parallel}, N_\mu) = (288, 64, 192)$ and $p=1$, corresponding to >28 million degrees of freedom per species, z limits obtained from equation 6 for $Z\in[-2.5\,\mathrm{m}, 2.5\,\mathrm{m}]$, $v_{\parallel\max} = 3.75 v_{ts0} = 3.5\sqrt{T_{s0}/m_s}$ and $\mu_{\max} = m_s(3v_{ts0})^2/(2B_p^2)$. These grids may seem highly resolved, but they are in fact marginally sufficient. For example, we found that the simulations were not stable with fewer than 256 cells along the field line. The resolutions used here are the outcome of a convergence analysis discussed in appendix C.

A couple of features motivate high velocity-space resolution. One reason for the seemingly extreme μ resolution is the location of the trapped-passing boundary. Consider that particles at this boundary in the center of the mirror ($z=0$) with $v_\parallel = v_{ts0}$ have $\mu = \mu_{tp} = m_s v_{ts0}^2/(2B_m)$ in the large R_m limit. Defining a thermal $\mu = \mu_t = m_s v_{ts0}^2/(2B_p)$ at $z=0$, we see that the trapped-passing boundary μ_{tp} is quite small by comparison: $\mu_{tp}/\mu_t = B_p/B_m = 1/20$ for the Pleiades WHAM case in figure 1. For the choice of $\mu_{\max} = 9\mu_t$ to handle the high velocity part of a Maxwellian, and a grid spacing of $\Delta\mu = \mu_{tp}$ to resolve the trapped passing boundary, we see that $N_\mu = 180$ cells or more are needed. While this $\Delta\mu = \mu_{tp}$ is marginal, this is alleviated some by the fact that a DG algorithm with p order polynomials is equivalent to $p+1$ optimally-located Gaussian quadrature points per cell in each direction. So the resolution capability of a $p=1$ DG code with N cells is comparable to a low-order grid with approximately $2N$ grid points. Also, as the electrostatic potential builds up to confine electrons, the trapped passing boundary shifts to higher energy, which is easier to resolve.

The combination of uniform velocity grids and large temperature variation is another feature calling for high velocity resolution. Typically continuum simulations have fixed (in $\boldsymbol{x}$) velocity grids with extents $v_{\parallel\max}\geq 4v_{ts0}$ (and an equivalent $\mu_{\max}$). For a plasma with temperatures that vary weakly in z, such grids are sufficient to resolve f_s well at all z and maintain f_s small near the boundary by a factor of $\lesssim$

$\exp\left[-v_{\parallel\max}^2/(2v_{ts0}^2)\right] \sim 10^{-4}$, so we can safely employ zero-flux BCs there. An HTS mirror, unlike the tokamak core that gyrokinetic models and codes have historically been developed for, has large temperature gradients along the field line. This means that a velocity grid that may seem sufficient in the cool expander would be far too small in extent for the plasma at $z = 0$ or vice-versa, a velocity grid that is appropriate in the center would be far too large and coarse for the expander. Continuum gyrokinetic codes, like `Gkeyll`, are then forced to either use a large grid with many cells at all z, or to compromise with grids that are smaller and more over-resolved than necessary at $z = 0$, and are fine enough to provide a reasonable description near and past the throat without being overly expensive. This compromise resulted in the grids used in this work.

It is worth interjecting with the caveat that two other approaches to support large temperature variations in kinetic simulations have been pursued elsewhere. One of them is to use multiblock grids where each block along z has a different $v_{\parallel\max}$ or resolution[60]. The second technique involves mapping velocity coordinates to ones normalized by the local thermal speed, e.g. $\widehat{v_\parallel} = v_\parallel/v_{ts}(z)$ and $\hat{\mu} = \mu/(m_s v_{ts}^2(z)/(2B_p))$[61]. Although these strategies may be further developed to work for our purposes, they can both suffer from diffusion in the μ direction either due to the inter-block interpolations or the numerical diffusion in the fluxes along μ that arise from the extra terms that normalizing μ introduces. Such diffusion would violate exact μ conservation, which is paramount in accurately depicting mirror processes. Additionally, multiblock velocity grids have only been used in one δf code, leaving us with the uncertainty of how boundaries in the direction of other blocks but not abutting other blocks must be treated in full-f codes.

The compromise that we have made for the grids is only half of the challenge; the other half is the duration that one intends to simulate and what time step (Δt) the numerical methods call for (thus determining the number of time steps needed). We leave the latter question for section III A below and discuss two time scales of interest. As stated in section I, one of our primary objectives is to determine whether our gyrokinetic model is consistent with a Pastukhov equilibrium. That is because in the future, when we study microstability and perpendicular transport, we would like to start from such an equilibrium and evolve the turbulence without potentially problematic macro-rearrangements of the plasma caused by the search for a different equilibrium. The Pastukhov potential, however, arises from a difference in the electron and ion collision times, which for the parameters in this work are nominally $\tau_{ee} \simeq 18\,\mu$s and $\tau_{ii} \simeq 36$ ms. Thus, to form this potential from a state away from equilibrium could take at many τ_{ee} or a τ_{ii}, which for the small Δt required could take millions to billions of time steps. In the following subsections, we describe the origin of this small Δt, and some ways to overcome it, yet reiterate that in the future, we will begin from a Pastukhov equilibrium estimated elsewhere (e.g. with semi-analytic methods or bounce-averaged Fokker-Planck codes).

A. Time step constraints

Given that the collisionality is relatively low for the plasmas of interest, the two primary constraints on Δt arise from the need to resolve the mirror acceleration and the electrostatic shear Alfvén (or ω_H) mode, the latter only arising in kinetic electron simulations. When integrated with explicit methods, the mirror acceleration, contained in the third term on the left side of equation 7, imposes the Courant-Friedrichs-Lewy (CFL) stability limit

$$\frac{\Delta t}{\Delta v_\parallel/(2p+1)} \max\left[\frac{1}{m_s}\frac{\partial(\mu B)}{\partial z}\right] \lesssim C, \tag{23}$$

where $\Delta v_\parallel = 2v_{\parallel\max}/N_{v_\parallel}$ is the cell length in $v_\parallel$ and C is an order unity number. Thus, the fine $v_\parallel$ grids needed to resolve f_s near and beyond the mirror throat, the small electron mass, the large $\mu_{\max}$ needed to capture f_s in the center, and the large gradients in B due to the HTS coils all conspire to give a small Δt. For the physical and computational parameters in sections II-III, equation 23 yields $\nu_{ee}\Delta t \simeq 1/(6\times 10^6)$, meaning that around 6 million time steps with large grids would be needed to reach a single τ_{ee}, and many more to build the equilibrium potential from $\phi = 0$.

When the limitation in equation 23 is overcome, say by using an implicit method or with the technique described in section III B, Boltzmann electron simulations are primarily limited by the parallel ion advection CFL, i.e.

$$\max\left(v_{\parallel i}k_\parallel\right)\Delta t \lesssim C, \tag{24}$$

typically an easily met criteria ($k_\parallel$ is the wavenumber along the field line). On the other hand, kinetic electron simulations are limited by the need to resolve the ω_H mode, the electrostatic branch of the shear Alfvén wave[62]. In the uniform slab with a linearized polarization, this constraint reads

$$\omega_H\Delta t = \frac{v_{te0}k_{\parallel\max}}{k_\perp\rho_{s0}}\sqrt{\frac{n_{e0}(z,t)}{n_0}}\Delta t \lesssim C. \tag{25}$$

Here $\rho_{s0} = c_{se0}/\omega_{ci}$ is the reference ion sound gyroradius, with $c_{se0} = \sqrt{T_{e0}/m_i}$ and $\omega_{ci} = q_iB_p/m_i$ the ion gyrofrequency. The linear analysis that leads to the frequency in equation 25 is done around the instantaneous and local equilibrium density $n_{e0}(z,t)$ (see appendix B 1). This high frequency also becomes harder to resolve as we refine the z-grid, which is needed in order to capture the field-aligned variation near and outside of the mirror throats since $k_{\parallel\max} \simeq \pi(p+1)/\Delta z = \pi(p+1)N_z/L_z$.

As we will see in section IV, there is some indication that decreasing $k_\perp$ can produce larger potential drops that are closer to the Pastukhov level and the Boltzmann' electron result. However, a decrease in $k_\perp$ entails a drop in Δt, if the mirror-force constraint is mitigated, and can make the simulation intolerably expensive. If $k_\perp\rho_{s0} = 0.01$, then our base parameters produce an ω_H frequency with a time step requirement, $\nu_{ee}\Delta t \simeq 1/(8.3\times 10^6)$, which is quite close to that demanded by the mirror force.

We are considering semi-implicit methods to bypass equation 25, but in the meantime, we have instead opted to utilize a larger $k_\perp$ and instead obtain a suitably peaked potential by incorporating the variation of the density in the polarization as described in section II B 2. In that case, the ω_H constraint becomes (see appendix B 2)

$$\omega_H \Delta t = \frac{v_{te0} k_\parallel}{k_\perp \rho_{s0}} \sqrt{\frac{n_{e0}(z,t)}{n_{i0}(z,t)}} \Delta t \lesssim C. \tag{26}$$

This $\sqrt{n_{e0}(z,t)/n_{i0}(z,t)}$ factor is everywhere very close to 1, in contrast to equation 25 where the $\sqrt{n_{e0}(z,t)/n_0}$ factor drops off in the expander. At first glance, this change would indicate that the nonlinear polarization model would need a smaller Δt, and all things being equal, it does. However, in the confined plasma where the pressure is largest, these factors are both close to 1 and the $\sqrt{n_{e0}(z,t)/n_{i0}(z,t)}$ factor in equation 26 will be offset by our increasing $k_\perp$ tenfold. We intend for this larger $k_\perp$ to produce reasonable ϕ profiles still, thanks to the natural decrease in $n_s(z,t)$ away from the center introduced into the polarization equation 20. These changes ought to lead to the friendlier approximate time step $\nu_{ee}\Delta t \simeq 1/(8.3\times 10^5)$.

B. Mitigating the mirror Δt by force softening

Upon closer examination of equation 23 we notice the smallest Δt is called for by the region of phase space with large μ and $\partial_z B$. The magnetic field gradient is maximized as one approaches the mirror throat, but at the same time, particles with larger μ are reflected by mirror forces. So in those same regions where $\max[\partial_z(\mu B)]$ occurs, we expect f_s to be very small (figure 3(a)). It is thus unfortunate that explicit time integration demands a tiny Δt from a region in which f_s is many orders of magnitude smaller and makes a possibly negligible contribution to the system's dynamics.

One way to mitigate this CFL constraint is to soften the mirror force in those regions of negligible f_s, inspired by the way high-speed particles are slowed down in some particle-in-cell methods[63]. Our approach here, to maintain the Hamiltonian structure of the system, is to introduce a softened Hamiltonian

$$H = \frac{1}{2} m_s v_\parallel^2 + \Pi(z,\mu)\, \mu B + q_s \phi - \frac{1}{2} m_s |\boldsymbol{v}_{\boldsymbol{E}}|^2, \tag{27}$$

where we multiplied the term giving rise to the mirror force by a phase-space factor $\Pi(z,\mu)$. We intend to use this factor to modify the advection speed in the $v_\parallel$ direction so that the mirror force term, given the Poisson bracket in equation 8,

$$\dot{v}_{\parallel\,\mathrm{mirror}} = -\frac{1}{m_s J B_\parallel^*} \frac{\partial}{\partial z} (\Pi(z,\mu)\mu B) = -\frac{\chi(z,\mu)}{m_s J B_\parallel^*} \mu \frac{\partial B}{\partial z} \tag{28}$$

is weakened by a factor $\chi(z,\mu)$ of our choosing. Once $\chi(z,\mu)$ is defined, the Hamiltonian softener $\Pi(z,\mu)$ can be obtained by integrating equation 28 from $z=0$ with the boundary values $\Pi(z=0,\mu) = \chi(z=0,\mu) = 1$. A weaker μB term in the Hamiltonian changes the CFL constraint due to the mirror forces from equation 23 to

$$\frac{\Delta t}{\Delta v_\parallel/(2p+1)} \max\left[\frac{\chi(z,\mu)}{m_s} \frac{\partial(\mu B)}{\partial z}\right] \lesssim C. \tag{29}$$

The $\chi(z,\mu)$ factor is chosen to remain 1 where f_s is appreciable but vanishes in regions limiting Δt despite their negligible f_s. One possibility is to choose $\chi(z,\mu) = 1$ in most places of interest and $\chi(z,\mu) \propto \mu_t(z)/\mu$ where f_s is negligibly small, with $\mu_r(z)$ being a threshold adiabatic moment beyond which we soften the Hamiltonian. However, $\chi(z,\mu)$ decays too slowly in that case, so we instead opt for

$$\chi(z,\mu) = \begin{cases} 1 & \mu \le \mu_t(z), \\ \frac{1}{2}\left[1 + \tanh\left(\frac{\mu_t(z) + 2.5w - \mu}{w/2}\right)\right] & \mu > \mu_t(z), \end{cases} \tag{30}$$

with $w = \mu_t(z)/10$. We define $\mu_t(z)$ as the largest adiabatic moment that is accessible at each z, $\mu_t(z) = \mu_{max} B_p / B(z)$, according to energy conservation but disregarding collisions, parallel kinetic energy (a relatively small correction for this high-field mirror) and the electrostatic potential because we do not know it a priori.

The softening function $\chi(z,\mu)$ in equation 30, used for some results in section IV, is plotted in figure 3(b). Notice, by comparison with figure 3(a), that the regions where the distribution function is many orders of magnitude smaller coincide with regions where $\chi(z,\mu) \to 0$. This correspondence

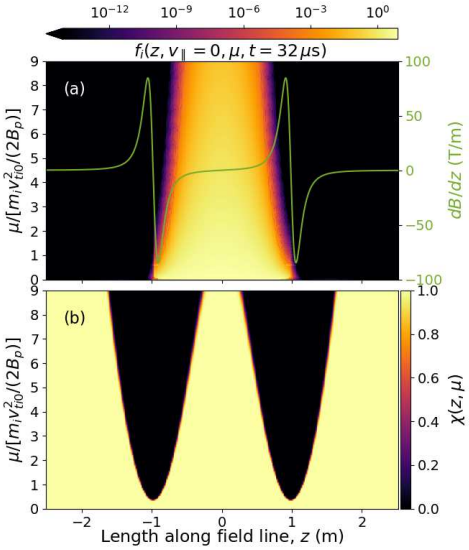

FIG. 3. (a) Ion distribution function at $v_\parallel = 0$ and $t = 32\,\mu$s (negative cells multiplied by -1 for simplicity of viewing) and the magnetic field gradient (green line). (b) Softening function $\chi(z,\mu)$ in equation 30.

is not exact, since other physics, like electrostatic forces, also shape the regions of small f_s. Additionally, electrostatic acceleration is signed and modifies the regions of small f_i and f_e differently. Therefore the optimal $\chi(z,\mu)$ will look slightly different for each species. In the future, we can incorporate estimates of the potential profile $\phi(z)$ in the definition of $\mu_t(z)$ to produce a more suitable softening function. Nonetheless, in section IV, we show results obtained with this $\chi(z,\mu)$ are sufficiently close to those without force softening and were obtained 19.5 times faster.

C. Further computational improvements

For Boltzmann electron simulations, force softening is sufficient to attain large time steps that result in simulations where the potential is built from scratch (i.e. $\phi(t=0)=0$) to a level comparable to the Pastukhov estimate in a matter of hours (on 288 cores). This is a nearly 20X speedup over simulations without force softening. However, kinetic electron simulations can still have a Δt too small for building the potential from scratch, especially if a linearized polarization is employed. Therefore, additional measures must be taken to further reduce the cost of these simulations if kinetic electron physics is of interest.

Assuming that it is, there are five modifications to the approach presented in this work that we are currently pursuing. These are:

1. Simulation time: As mentioned earlier and illustrated in section IV, developing the (Pastukhov) equilibrium potential from $\phi(t=0)=0$ can take many ν_{ee}^{-1} to $\sim\nu_{ii}^{-1}$, which requires costly simulations with millions or billions of time steps and large grids. However, the ultimate goal of mirror gyrokinetics is to examine the stability of gradient-driven modes (e.g. interchange) and perpendicular turbulent transport, which occurs on a much smaller time scale than that of the equilibrium evolution. For example, for the parameters used in this work, the potential takes on the order of $100\,\mu$s to reach the Pastukhov estimate, while the interchange time scale is $\sim z_m/(2v_{ti0})\lesssim 1\,\mu$s[64]. Therefore, studies of interchange stability and transport will time integrate for a $\sim$10X shorter period and result in $\sim$10X cheaper simulations (assuming ideal perpendicular parallelism).

2. Improved ICs: For both 1D and higher-dimensional simulations, one could start from ICs closer to the final (Pastukhov) equilibrium than those in equations 12-16 to shorten the required simulation time. Such ICs could be obtained with semi-analytical[25] or analytical (under development) methods that compute the equilibrium more quickly. Another approach is to first perform a Boltzmann electron simulation, which is $\sim\sqrt{m_i/m_e}\approx 60$ times faster, and use that result as the IC of a kinetic electron simulation.

3. Nonuniform grids: the cost of these simulations can be reduced by using nonuniform grids with higher resolution only where needed. For example, in `Gkeyll` one could use a coordinate mapping $(z,v_\parallel,\mu)=(z(\xi),v_\parallel,\mu(\eta))$, where ξ and η are the computational coordinates along the field line and along μ, respectively, to place more degrees of freedom (DOFs) near the mirror throats and at low μ (DOFs uniformly spaced in ξ and η). We estimate that this could reduce the number of DOFs, and thus speed up the code, by a factor of 10-15 – a factor of 2-3 from using a nonuniform z grid and a factor of 5 from a proportional μ grid[65].

4. Positivity preservation: A novel, rigorous method for preserving positivity of the particle distribution function while conserving energy in Hamiltonian systems has been developed[66] and implemented in another branch of `Gkeyll`. Ensuring $f_s\geq 0$ would improve robustness of simulations on coarser grids, and thus reduce computational cost.

5. Improved parallelization: The results in this manuscript were produced with an earlier version of `Gkeyll`; since then, additional parallelization strategies have been implemented. Specifically, these simulations can now be performed on GPUs, parallelizing over velocity space and species. Parallelization over species alone reduces the time to solution by 2X, and similar reductions are found from GPUs and velocity space parallelization.

Most of these improvements are ready for use. Hence we expect that future work will take advantage of such capabilities to perform simulations at a small fraction of the cost of the simulations reported here. Additionally, we may use such enhancements to do more complex studies like parameter scans, 3D simulations, or simulations with sloshing ions.

IV. RESULTS

In this section, we report on results from three types of simulations we carried out; namely those using

- Boltzmann electrons with & without force softening,
- kinetic electrons with linearized polarization without force softening, and
- kinetic electrons with nonlinear polarization & force softening.

These results can be reproduced using the `Gkeyll` input files found under version control at https://github.com/ammarhakim/gkyl-paper-inp/tree/master/2023_PoP_gkwham1x2v. As stated earlier, our two-fold intention here is to examine the computational challenges in modeling an HTS mirror with a continuum gyrokinetic code and to determine if these models develop the (Pastukhov) electrostatic potential expected for such machines.

We can obtain an approximation for the potential drop between the center of the plasma and the mirror throat by considering the collisional electron loss rate computed by Pastukhov[13] and later corrected by others[14,15]:

$$\frac{dn_e}{dt}=-\frac{4}{\sqrt{\pi}}A_p\frac{\nu_{ee}n_e}{G(R_m)}\left(\frac{e\phi}{T_{e0}}\right)^{-1}e^{-e\phi/T_{e0}}I(T_{e0}/e\phi) \quad (31)$$

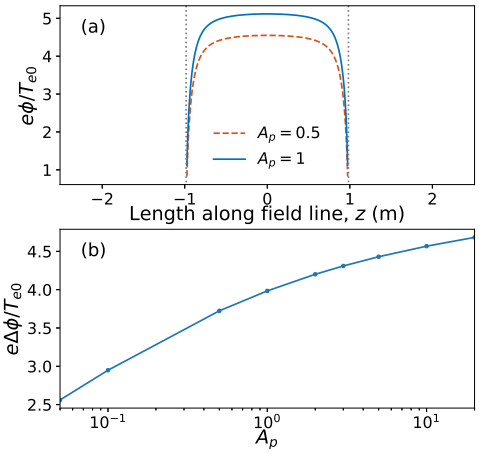

FIG. 4. (a) Estimated Pastukhov potential profile for the mirror using parameters in tables I-II and equations 31-33, absent in the expanders because the assumptions are not valid there. Vertical dotted lines indicate the mirror throat locations. (b) Potential drop between the mirror center ($z = 0$) and the mirror throat ($z = z_m = 0.98$ m) in the Pastukhov estimate as a function of an electron collision frequency scaling factor (A): $\nu_{ee} \to A\,\nu_{ee}$.

in terms of the functions

$$G(x) = \frac{2x+1}{2x}\ln(4x+2),$$
$$I(x) = 1 + 0.5\sqrt{\pi x}\,e^{1/x}\mathrm{erfc}\left(\sqrt{1/x}\right). \tag{32}$$

We have introduced a scaling factor A_p for several reasons. First, we want to observe the change in the potential drop as one scans the collision frequency. Second, the Pastukhov-Chernin-Cohen approximation incorporates electron-electron and electron-ion collisions, but our kinetic electron simulations only account for electron-electron collisions for now. By itself, this would make it more appropriate to compare our kinetic results with the analytic Pastukhov estimate using a scaling factor of $A_p = 0.5$, but there are other effects that may make the effective A_p greater than 1. There is also an issue with differences between the velocity dependence of the collision frequency in the Dougherty (this work) and LRO (used by Pastukhov) operators, as explained in section II B. These effects would increase A_p, though the final impact on the potential depends on the relative importance of pitch-angle and velocity scattering for electrons and ions. Future code validation will employ the equivalent of Pastukhov's calculation using the Dougherty operator (under development), but for now we see below that the exact results depend weakly on A_p.

From equation 31 we may calculate an electron particle confinement time $\tau_{pe} = n_e/(dn_e/dt)$. The ion particle confinement time, however, is much longer because ions are collisionally scattered less frequently and is of the order $\tau_{pi} = \nu_{ii}^{-1}\log R_m$ according to analytical and numerical study of the LRO equation[12]. Since electrons are scattered into the loss cone and thus exit to the expander and the sheath more quickly, they leave behind the ions, and an electrostatic potential begins to build. This potential starts to decelerate electrons and accelerate ions until the loss rates for both species equalize and

$$\tau_{pe} = \tau_{pi}. \tag{33}$$

Said differently, a potential develops to maintain quasineutrality. The so-called Pastukhov potential ϕ that satisfies equation 33 may be numerically solved for via root finding. Doing so at each z with $R_m = B_m/B(z)$ using the reference plasma parameters in tables I-II, we obtain the potential given in figure 4(a). The assumptions that lead to equation 31 are not valid in the expander due to, for example, the large mean flow velocities and weak collisionality therein; for this reason figure 4(a) only shows ϕ inside the mirror.

A key metric for mirrors is the potential drop between the central plasma ($z = 0$) and the mirror throat ($z = z_m = 0.98$m), since a sufficiently large electric field is needed to elecrostatically confine the electrons and reduce parallel electron heat convection. In this Pastukhov estimate, the potential drop normalized to the reference electron temperature is $e\Delta\phi/T_{e0} = 3.98$ (3.72) for $A_p = 1$ (0.5), which is in the range of those numerical and experimental results mentioned in section I. Additionally, since this potential arises from the difference in scattering rate between ions and electrons, if the electrons scatter more frequently (increasing ν_{ee}), a larger potential drop will develop to contain them and maintain quasineutrality. This phenomenon explains the trend in figure 4(b), for which we computed the potential drop corresponding to a series of scaled electron collision frequencies. The increase in $e\Delta\phi/T_{e0}$ with ν_{ee} will partially explain some differences between Boltzmann and kinetic electron simulations presented below.

A. Boltzmann electrons

The Boltzmann electron model evolves the ion distribution function $f_i(z, v_\parallel, \mu)$ according to equation 7 and the field model in section II B 3. The initial condition consists of a Maxwellian f_i and has potential profile that drops from $\phi(z = 0, t = 0) \approx 3.2$kV to $\phi(z = \pm L_z/2, t = 0) = 0$ because no ion fluxes have crossed the sheath entrance at that time yet. As we integrate the model in time, ions are lost from the central region to the expander and sheath via pressure relaxations and collisional scattering. The ions in the expander are also further accelerated by the mirror force pointing towards the sheath, where they are lost by the sheath BCs that absorb all arriving ions. The result is an ion density that decreases away from the central region and increases the potential drop from the center to the wall via equation 22. The potential that develops works against the mirror force to accelerate ions through the mirror throat and towards the sheath, thus enhancing the loss of ions. These losses are eventually balanced by the plasma source near $z = 0$, at which point the simulation reaches a steady state.

Reaching this steady state of the ion profiles likely requires time-integrating the system to $O(\nu_{ii}^{-1})$ seconds. Our goal, however, is only to integrate it long enough to see if it reaches the Pastukhov estimate. We did so for nearly $4\nu_{ee}^{-1}$ at first, requiring 73.52 hours on 288 cores when using the $288\times64\times192$ grids mentioned in section III that were chosen as a result of a resolution scan described in appendix C. The spatio-temporal evolution of ϕ, for example, is shown in figure 5. We see that the initial potential from ICs becomes more peaked and continues to rise in amplitude as one approaches $t=\nu_{ee}^{-1}=18\,\mu$s. It is only coincidental that much of the $\phi(z=0)$ amplitude is built within one electron collision period, as the Boltzmann electron model does not contain the ν_{ee}^{-1} time scale. The initial rapid rise in the potential is likely associated with transient effects from ions originally in the loss cone traversing the machine and escaping on the ion transit time ($L/(2v_{ti0})\approx4\,\mu$s). On a longer time scale the ions in the loss cone are replenished by pitch angle scattering of ions that are initially in the trapped part of velocity space into the loss cone. This will not fully come to equilibrium until an ion collision period ($\nu_{ii}^{-1}\approx35$ ms), but since we start with a high density of ions in the trapped region, comparable to what is expected in the final steady state, this is probably a major source of ions in the loss cone in these simulations after a few ion transit times when the initial ions there have already escaped. Our Maxwellian source also injects some ions directly into the loss cone, but most of the source is into the trapped part of phase space. The ambipolar potential hole also increases as the potential rises, augmenting another mechanism for ions to escape. By the time $t\approx(8/3)\nu_{ee}^{-1}=48\,\mu$s is reached, the central potential reaches $e\phi(z=0)/T_{e0}=11.28$ and its growth appears to slow down considerably.

Near this final state, at $t=32\,\mu\text{s}\approx1.78\nu_{ee}^{-1}$, the ion fluid moments have developed to those in figure 6 (solid lines). The ion density remains peaked near the reference density n_0, demonstrating confinement of the plasma; the density drops by over 4 orders of magnitude from the center to the sheath entrance, a decrease much faster than $B(z)/B_p$. The ion mean parallel flow speed in figure 6 exhibits a relative stagnation in the confinement region and a rapid acceleration to $u_{\parallel i}=c_{se0}$ near the mirror throats. This increase in $u_{\parallel i}$ continues in the expander due to combined contributions from the parallel electric field, the mirror forces and conservation of mass (e.g. as in a nozzle). In terms of the local sound speed, $c_s=\sqrt{(T_{e0}+3T_{\parallel i})/m_i}$, the ions also become supersonic at $z=z_m$ but are instead accelerated to $u_{\parallel i}/c_s\approx2-3$ by the time they reach the sheath. This is reminiscent of the accelerating solution obtained for low (source) injection velocities in recent PIC simulations[24]. Lastly, figure 6 also demonstrates the strong anisotropy of this scenario throughout the whole device, especially near the throat where $T_{\perp i}$ is considerably larger than $T_{\parallel i}$ (40 times larger in fact) as one would expect from conservation of energy and μ.

The temperature can be sensitive to velocity-space features of the distribution function, and one such feature explains why this Boltzmann electron simulation was not continued past $\nu_{ee}t=8/3$. Figure 7 presents the ion distribution function at $z=\{0,z_m,L_z/2\}$, i.e. the center, throat and sheath entrance. The first panel shows the archetypal mirror plot, except that due to the strong magnetic field in this device and the fact that

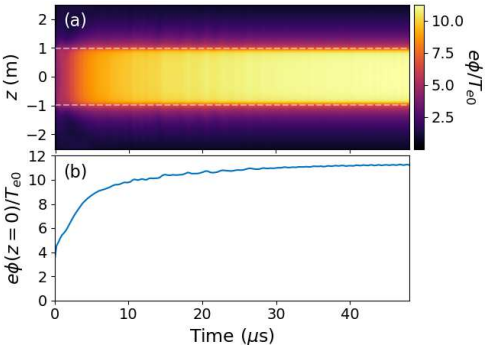

FIG. 5. (a) Electrostatic potential $\phi(z,t)$ in the case with Boltzmann electrons (mirror throats indicated with white dashed lines), and (b) central electrostatic potential for $t=0-48\,\mu\text{s}=0-(8/3)\nu_{ee}^{-1}$.

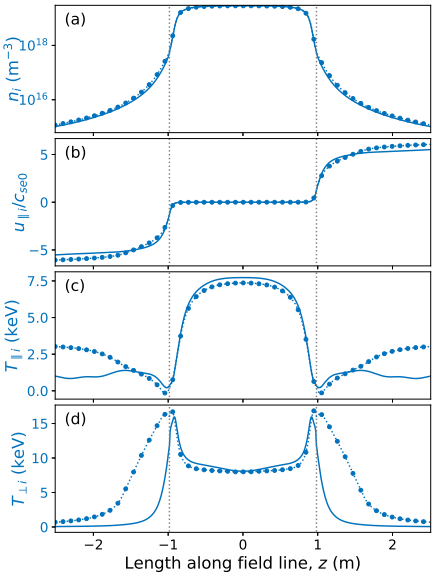

FIG. 6. (a) Ion guiding center density (n_i), (b) mean drift speed ($u_{\parallel i}$) normalized to $c_{se0}=\sqrt{T_{e0}/m_i}$, and (c) parallel and (d) perpendicular temperatures ($T_{\parallel i}$, $T_{\perp i}$) at $t=32\,\mu\text{s}\approx1.78\nu_{ee}^{-1}$ in Boltzmann electron simulation without (solid) and with (dotted with circles) force softening. Vertical dotted lines indicate the mirror throat locations.

it is shown in $v_\parallel - \mu$ coordinates, the loss cone appears narrow and parabolic. Nonetheless, the simulation's $f_i(z=0, v_\parallel, \mu)$ follows the (dotted white) contour of the trapped boundary given by

$$\frac{\mu B_p}{\mu B_p + m_s v_\parallel^2/2 + q_s \delta\phi} \geq \frac{1}{R_m}, \tag{34}$$

including the contribution of the self-consistently generated potential ($\delta\phi = \phi(z=0) - \phi(z=z_m)$) that leads to the ambipolar hole near the origin. As one approaches and passes through the mirror throat, only low-μ particles that were not mirror confined can be found, and f_i becomes very localized near $\mu = 0$. This makes it challenging to resolve f_i in these regions if we use uniform grids, as `Gkeyll` and some other gyrokinetic codes do. In this case, the distribution function is perhaps only marginally resolved at the throat, where f_i is only appreciable in a few cells along μ. In the last panel, located at the sheath entrance, we see an f_i that slants towards higher $v_\parallel$ and μ. This is a result of an acceleration of particles due to the Yushmanov potential (i.e. combined mirror and electrostatic potential). We can estimate the $v_\parallel$ to which particle just inside the loss cone at $(z, v_\parallel, \mu) = (0, 2.5 v_{ti0}, 0.2374 m_i v_{ti0}^2/(2B_p))$, where f_i is only 100 times smaller than near the origin, is accelerated to by the time it reaches the sheath entrance from conservation of energy:

$$v_\parallel = 2.5 v_{ti0} + \left[2\frac{e\delta\phi + \mu\delta B}{m_i}\right]^{1/2} = 4.09 v_{ti0}, \tag{35}$$

and $\delta Q = Q(z=0) - Q(z=L_z/2)$. But our velocity grid only goes up to $v_{\parallel\max} = 3.75\, v_{ti0}$ causing these particles to run into our $v_\parallel$ boundary, producing an accumulation of f_i (with a very large $\partial_{v_\parallel} f_i$) near the boundary due to the zero-flux BCs in velocity directions. This is the origin of the small bright spot near $(z, v_\parallel, \mu) = (L_z/2, 3.75 v_{ti0}, 0.5776 m_i v_{ti0}^2/(2B_p))$ in figure 7(c). This is not a numerical instability itself, because the maximum f_i at the boundary grows only linearly in time, and it can be delayed significantly by increasing $v_{\parallel\max}$ (at some computational cost). This artifact is not noticeable in most of our simulations for the time duration that we ran them, and is worse here because of the large potential drop in the expander region for the Boltzmann electron case. But if the simulation continued for very long times ($\nu_{ee} t > 8/3$ for this Boltzmann electron case with these parameters), this numerical artifact can get so large that it triggers an instability of some sort, and the simulation quickly crashes. This problem should be solved by a combination of improvements: a rigorous positivity-preserving scheme[66], non-uniform velocity grids to more easily extend $v_{\parallel\max}$, or perhaps most rigorously by extending $v_{\parallel\max}$ to infinity and using exponential weighted basis functions there[39]. For the time being, we shall see in the next subsection that our force softening technique also has a beneficial effect in this regard.

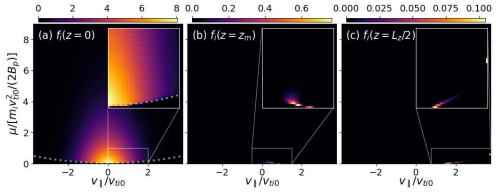

FIG. 7. Ion distribution function in Boltzmann electron simulation at $t = 48\,\mu\text{s} = 8\nu_{ee}^{-1}/3$ at three locations along the field line: (a) the center, (b) the mirror throat, (c) the sheath entrance in the expander.

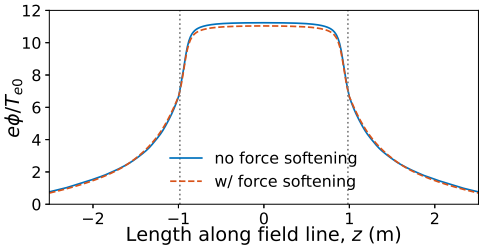

FIG. 8. Electrostatic potential at $\nu_{ee} t \approx 8/3$ in Boltzmann electron simulations with (dashed orange) and without (solid blue) force softening. Note that the $\phi(z)$ variation is not accurate for $|z| > z_m$ because Boltzmann assumptions break down in the expanders.

Force softening benchmark

We carried out the same Boltzmann electron simulation employing the force softening technique described in section III B in order to overcome the CFL condition that makes Δt small. This strategy allowed us to run the same simulation up to $t = 48\,\mu\text{s} = 8\nu_{ee}^{-1}/3$ in approximately 3.76 hours (on 288 cores), denoting a 19.5X speedup. When we compare the potential profile of these two simulations (figure 8) we find that the two agree very well. The small disagreement in the confined region is negligible considering that there are other shortcomings of our model that likely have a larger impact (e.g. collision model, neglect of beam ions, resolution, Boltzmann assumption).

Other quantities also exhibit agreement between the base Boltzmann electron simulation and that with force softening. For example, the ion number density and parallel fluid speed are very close in these two simulations, albeit a $\approx 9\%$ difference in the expander $u_{\parallel i}$ (compare solid and dotted-circled lines in figures 6(a)-(b)). Also, in figure 6, we appreciate that force softening did not change the temperatures in the confined plasma much. It does lead to higher $T_{\parallel,\perp i}$ in the expander, particularly near the throats where $T_{\perp i}$ is significantly larger. Note that the perpendicular temperature in force softened simulations is calculated using the softened Hamiltonian, that is $T_{\perp s} = n_s^{-1} \int \mathrm{d}\boldsymbol{w}\, \Pi(z,\mu) \mu B B_\parallel^* f_s$. These elevated temperatures can be a result of force softening allowing higher en-

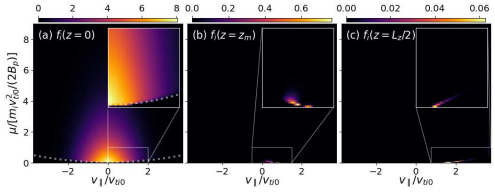

FIG. 9. Ion distribution function in Boltzmann electron simulation with force softening at $t = 48\,\mu\text{s} = 8\nu_{ee}^{-1}/3$ at three locations along the field line: (a) the center, (b) the mirror throat, (c) the sheath entrance in the expander.

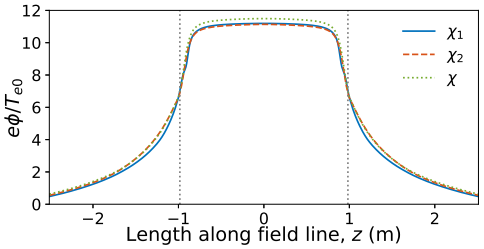

FIG. 10. Electrostatic potential at $\nu_{ee}t \approx 5.56$ in Boltzmann electron simulations, using three types of softening factors (equations 30 and 36).

ergy particles out to the expander than the experiment (or the simulation without force softening) does, which have a larger effect on the temperature than on the lower velocity moments. The density near the throats and in the expander also get very low, so the accuracy with which temperatures are computed is compromised. Nonuniform grids (see section III C) will help us qualify these properties more accurately in subsequent studies.

Good qualitative agreement between simulations with and without force softening is seen in the ion distribution function, shown in figure 9 at the same three locations as in figure 7. The most notable difference is that the numerical anomaly previously present near $(z, v_\parallel, \mu) = (L_z/2, 3.75v_{ti0}, 0.5776 m_i v_{ti0}^2/(2B_p))$ is now absent. Now that the distribution function is monotonically decaying near the velocity boundary and that the simulation advances faster than without force softening, we can time integrate for longer periods of time. Moreover, we performed the simulation to $t = 100\,\mu\text{s} \approx 5.56\nu_{ee}^{-1}$ with two other softening factors,

$$\chi_1(z,\mu) = \begin{cases} 1 & \mu \le \mu_t(z), \\ \mu_t(z)/\mu & \mu > \mu_t(z), \end{cases}$$
$$\chi_2(z,\mu) = \begin{cases} 1 & \mu \le \mu_t(z), \\ \frac{1}{2}\left[1 + \tanh\left(\frac{\mu_t(z)-\mu}{\mu_t(z)/20}\right)\right] & \mu > \mu_t(z), \end{cases} \tag{36}$$

in order to assess how sensitive the result may be to this choice. We see in figure 10 that for the three softening factors used, the resulting potential is almost the same in each case. Additionally, note by comparing figures 8 and 10 that the profiles have changed little from $\nu_{ee}t = 8/3$ to $\nu_{ee}t = 5.56$; most of the potential profile in Boltzmann electron simulations is built within a few ion transit times.

Another important thing to note about this potential profile is that the potential drop between the plasma center and the mirror throat is $e\Delta\phi/T_{e0} = 4.47$. This indicates that there is strong electrostatic confinement of the electrons and that the potential drop is close to yet exceeds the Pastukhov estimate of $e\Delta\phi/T_{e0} = 3.72$ in figure 4. One possible explanation for the increased potential drop is that the Boltzmann approximation essentially implies highly collisional electrons, for which the Pastukhov calculation can yield potentials above $\simeq e\Delta\phi/T_{e0} = 4.47$ (see figure 4(b)). It is also apparent that according to this model, there is an additional, strong potential drop in the expander of $e(\phi(z = z_m) - \phi(z = \pm L_z/2))/T_{e0} = 6.39$ that further confines the electrons. As mentioned earlier the Pastukhov calculation is not valid in the expander, so this Boltzmann electron simulation is a first rough estimate of what the potential profile may be in that region. At the same time, we know that the isothermal, Boltzmann electron assumption is invalid in the expander since we would expect large temperature drops, relatively collisionless plasma (due to the rapid drop in density), and non-Maxwellian distributions[59] therein. Other recent semi-analytic estimates of this potential structure actually produce little to no potential drop in the expander[25]. More accurate estimations of the profile may be attained by relaxing the isothermal, Boltzmann assumption or using kinetic electrons.

B. Kinetic electrons

The kinetic electron model evolves the gyrokinetic equation 7 for both ions and electrons, and computes the electrostatic potential using a Poisson equation with either a linearized polarization (equation 19) or a nonlinear polarization (equation 20); we present results for both field models in this section.

Linear polarization

Kinetic electron simulations with a linear polarization were performed with the $288 \times 64 \times 192$ grid mentioned in section III, which was deemed the most suitable according to the resolution scan in appendix C. These simulations require the choice of the parameter $k_\perp$ in equation 19, and thus one of our first tasks was to examine the effect this parameter has on the resulting potential. In principle, the lowest possible value of $k_\perp\rho_s$ would be preferable in order to approximate the $k_\perp\rho_s \to 0$ limit we are interested in, given our choice of 1D models. Additionally, as we would expect from equation 19, smaller $k_\perp\rho_s$ would lead to larger potentials, possibly as large as those seen in previous experiments or the Pastukhov potential estimate at the beginning of this section. Such an increase in ϕ with decreasing $k_\perp\rho_s$

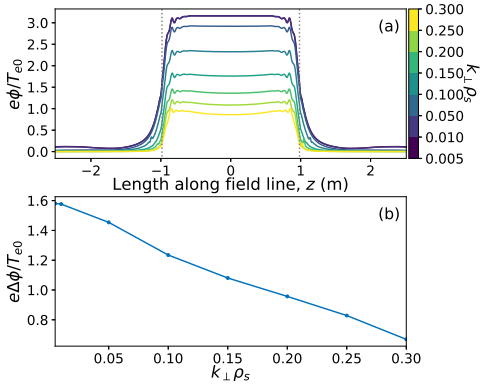

FIG. 11. (a) Electrostatic potential profiles in kinetic electron simulations with linearized polarization, and (b) the potential drop from the center ($z=0$) to the mirror throat ($z=z_m$) normalized to T_{e0}/e at $t=8\,\mu$s as a function of $k_\perp\rho_s$.

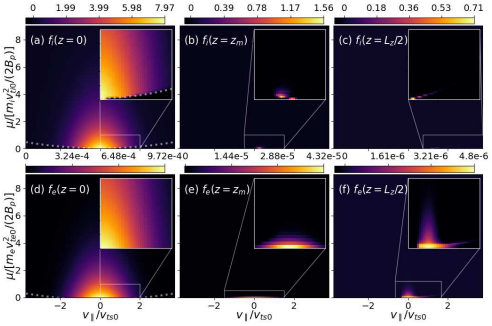

FIG. 12. Ion (top row) and electron (bottom row) distribution functions in kinetic electron simulation with linearized polarization at $t=32\,\mu\text{s}\approx 1.78\nu_{ee}^{-1}$ and three locations along the field line: (a,d) the center, (b,e) the mirror throat, (c,f) the sheath entrance in the expander.

is precisely what we see in figure 11(a), showing the potential at $t=8\,\mu$s. Precisely how fast the potential increases with $(k_\perp\rho_s)^{-1}$ can be seen in figure 11(b), where we provide the potential drop between the center and the mirror throats ($\Delta\phi$) for each $k_\perp\rho_s$. Extrapolating to $k_\perp\rho_s=0$ or examining the points at $k_\perp\rho_s=\{0.005, 0.01\}$ on may conclude that the asymptotic limit has been reached by $k_\perp\rho_s=0.01$, although it is difficult to claim that with certainty at this point. We would have liked to continue this study at lower $k_\perp\rho_s$, but as explained in section III A the ω_H frequency increases with $(k_\perp\rho_s)^{-1}$ and therefore makes the simulations impractically expensive for $k_\perp\rho_s<0.005$. One can also estimate that in WHAM (with $B_p=0.86$, $R_m=20$) $\rho_s=5.17\times10^{-3}$ m, and the smallest perpendicular mode that fits in a $2a_{\text{lim}}$-diameter plasma is $k_\perp\approx\pi/(2a_{\text{lim}})$ such that $k_\perp\rho_s=0.06$. If one further considers that $B(z)\,a(z)^2$ is a constant along z, with $a(z)$ being the minor radius of the plasma, $k_\perp\rho_s$ can be 0.015 (keeping temperature constant) or smaller near the mirror throat.

Based on such $k_\perp\rho_s$ scan, we decided to time integrate the kinetic electron simulation with $k_\perp\rho_s=0.01$ for a longer period of time. As these simulations are run longer, the oscillations seen near the mirror throats in figure 11(a) vanish since they result from the relaxation of initial profiles. By employing 288 cores for 1,019 hours, this kinetic electron simulation was advanced to $t=32\,\mu\text{s}\approx 1.78\nu_{ee}^{-1}$, at which point the ion and electron distribution functions at the center, mirror throat and sheath entrance looked as shown in figure 12(a-c). Through comparison with figure 7 we see that the structure of f_i is similar to that in the Boltzmann electron simulations. The ion distribution function obeys the expected trapped passing boundary at $z=0$, and has a slanted arrangement at the sheath entrance caused by the decreasing Yushmanov potential. It is notable, however, that in this case, we do not see an accumulation of f_i near the $v_\parallel$ boundary as we did in the Boltzmann electron case. That is because, as we show below, in the expander of the kinetic electron model the potential drop is very small and leads to a much weaker electrostatic acceleration of the ions.

A kinetic electron simulation also gives us insight into the phase space structure of the electrons, and we provide a snapshot of it in figure 12(d-f). A first observation of this f_e makes it apparent that although electrons seem Maxwellian in the confined plasma, consistent with the Boltzmann model, they acquire non-Boltzmann features as one moves into the expander and approaches the sheath entrance. This is direct evidence of the limitations of the Boltzmann model, and may also help us derive better reduced electron models. The electron distribution function in the mirror center ($z=0$) also obeys the expected trapped-passing boundary given in equation 34. However, it can be difficult to discern in figure 12(d) for three reasons. First, the electrostatic force pushes these boundaries away from the origin so that some particles with $\mu=0$ (and no mirror confinement) are still confined. Second, in $v_\parallel-\mu$ space, the loss cone is actually a parabola, making it harder to discern the familiar cone. The HTS coils and the electrostatic potential also provide such good electron confinement that the loss cones are very narrow and far from $v_\parallel=0$. And third, where the loss cones appear in this $v_\parallel-\mu$ space, f_e is so small that it is difficult to appreciate its details (unless one plots in other ways and sacrifices visualizing other features). In the expander (figure 12(f)) we also see some signs of Yushmanov acceleration (the branch of f_e that extends towards higher $v_\parallel$ and μ). And in contrast to the ions, the electrons have a population that propagates back towards the machine (i.e. $f_e(v_\parallel<0)$) resulting from the reflection by the sheath potential and is truncated at $v_\parallel\approx(2e\phi(z=L_z/2)/m_e)^{1/2}$ as we would expect from our sheath BCs[54].

The sheath potential at this time, $e\phi(z=\pm L_z/2)/T_{e0}=0.0552$ is considerably smaller than the $e\phi(z=\pm L_z/2)/T_{e0}=0.7924$ produced by Boltzmann electrons (see figure 13(b)). This is partly because the latter results from ambipolar sheath

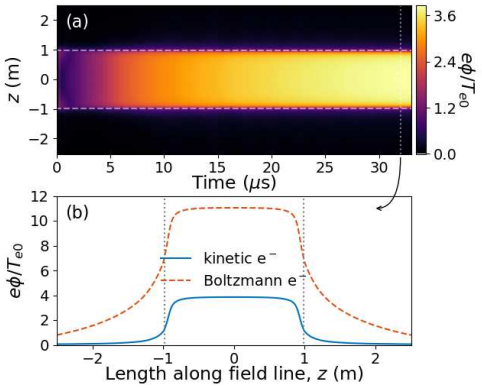

FIG. 13. (a) Electrostatic potential $\phi(z,t)$ in simulation with kinetic electrons and linearized polarization (mirror throats indicated with white dashed lines), and (b) electrostatic potential profile at $t = 32\,\mu\text{s} \approx 1.78\nu_{ee}^{-1}$. Note that the $\phi(z)$ variation in the Boltzmann electron case is not accurate for $|z| > z_m$ because Boltzmann assumptions break down in the expanders.

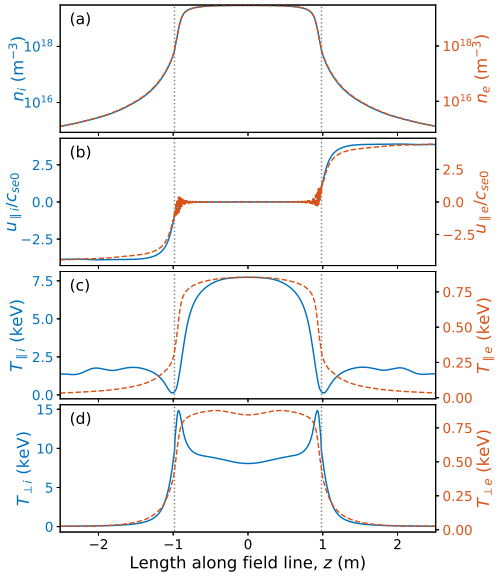

FIG. 14. Number density (a), mean flow speed (b), parallel (c) and perpendicular (d) temperature of the ion (solid blue) and electron (dashed orange) distribution functions at $t = 32\,\mu\text{s} \approx 1.78\nu_{ee}^{-1}$ in kinetic electron simulation with linearized polarization.

fluxes and the Boltzmann approximation, while the former is established by the separation of ion and electron guiding center charge density in the Poisson equation. The difference between Boltzmann and kinetic electron particle dynamics in the expander, which sets the potential therein, is also partly due to the short electron transit time that precludes thermalization in the kinetic electron case (see section II B 3). That is, the Boltzmann electron expander has thermalized electrons by design, while the kinetic electron model has non-Maxwellian electrons that escaped the confined region and traverse the expander before they have time to thermalize.

In addition to these differences between Boltzmann and kinetic electron models, comparison of these cases should also keep in mind that they may approach steady state at different rates, and that neither has yet reached such point. This limitation is apparent in figure 13(a), which shows that by the end of the kinetic electron simulation ($\nu_{ee}t \approx 1.83$) the electrostatic potential continues to rise. When we analyze the potential profiles away from the sheath, we see that the potential drop between the center and the mirror throats ($e\Delta\phi/T_{e0} \approx 2.57$) is lower than that obtained with Boltzmann electrons ($e\Delta\phi/T_{e0} \approx 3.94$). Furthermore, there is a large potential drop in the expander seen with Boltzmann electrons that is absent with kinetic electrons. Differences like these are to be expected, though, given that the isothermal and Boltzmann electron assumptions are invalid in the expander and near the mirror throat, as discussed in section II B 3. We simply employ the Boltzmann model an intermediate tool that may be honed in future work.

It is also interesting to examine the velocity moments of this kinetic electron model, provided in figure 14. Although given at a slightly different time, these ion moments are similar to those in the Boltzmann electron simulation (figure 6). The main difference is the lower mean flow speed ions are accelerated to in the expander of the kinetic electron simulation, $u_{\parallel i} \approx \pm 4c_{se0}$ vs. $u_{\parallel i} \approx \pm 5.5c_{se0}$ with Boltzmann electrons. Ion densities and temperatures are nearly the same in both cases. Additionally, we can also see the resulting electron moments now. The first two of these moments, n_e and $u_{\parallel e}$, resemble their ion counterparts. A notable distinction is the oscillatory behavior in $u_{\parallel e}$ near the mirror throats; we think this is purely numerical as we have seen them vanish and get replaced by smooth profiles following the average of these oscillations when using a piecewise quadratic ($p = 2$) basis (not shown here). The electron temperatures, however, are much lower and similar to each other, indicating much higher levels of isotropy than it is found for the ions. This is to be expected based on the large ν_{ee}/ν_{ii} ratio, the fact that we have evolved the system for $1 < \nu_{ee}t \ll \nu_{ii}t$, that the electron collision period is much longer than the electron bounce period ($\sim \nu_{ee}^{-1}v_{te0}/L_m \approx 118$), and previous theory and simulation yielding essentially Maxwellian electrons in the confined plasma[17].

Nonlinear polarization and force softening

The linear polarization model did not allow time integration for longer periods because, even if one used force softening,

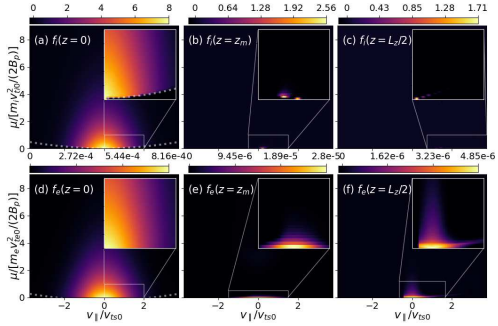

FIG. 15. Ion (top row) and electron (bottom row) distribution functions in kinetic electron simulation with nonlinear polarization at $t = 32\,\mu\text{s} \approx 1.78\nu_{ee}^{-1}$ and three locations along the field line: (a,d) the center, (b,e) the mirror throat, (c,f) the sheath entrance in the expander.

the ω_H mode frequency was very large for $k_\perp\rho_s = 0.01$ and made the time step very small. Our second alternative to explore potential formation with kinetic electrons is to use the nonlinear polarization model (equation 20) with force softening. At first, we attempted to use the same $288 \times 64 \times 192$ grid employed for previous Boltzmann and kinetic electron simulations, reaching $t = 32\,\mu\text{s} \approx 1.78\nu_{ee}^{-1}$ with 288 cores in 107.72 hours (a >9X improvement in performance). However, shortly after this phase the simulation became unstable, possibly due to insufficient resolution near the mirror throat and in the expander. We therefore carried out a second kinetic electron simulation with nonlinear polarization and force softening but using a $288 \times 96 \times 192$ grid, i.e. $N_{v_\parallel}$ was increased by 50%. This section focuses on this second, higher resolution simulation.

The kinetic electron simulation with nonlinear polarization reached $t = 32\,\mu\text{s} \approx 1.78\nu_{ee}^{-1}$ in approximately 213 hours on 288 cores. At this time the distribution functions at the center, mirror throat and sheath entrance looked very similar to those in the simulation with linearized polarization (compare figures 12 and 15). The distributions at the center of the device exhibit the expected loss paraboloids (dotted white lines in figures 15(a,d)), and in the sheath entrance f_e is truncated at the cutoff velocity corresponding to the sheath potential. Although hard to appreciate, this cutoff is at a lower $v_\parallel$ in figure 12(f) than in figure 15(f), suggesting that the sheath potential is higher in the nonlinear polarization simulation. More noticeable differences are seen in the velocity moments, at least between kinetic electron simulations with linear (figure 14) and nonlinear polarization (figure 16). There is slightly more separation between the guiding center densities in the nonlinear polarization case than in the linear polarization, although the logarithmic scales obscure it; such separation foretells a taller potential profile, as shown below. The ion parallel mean speed raises to the same amplitude in both simulations near or past the mirror throat, but in both cases, it is inferior to its value in the Boltzmann electron case (figure 7). On the other hand, $u_{\parallel e}$ saw a considerable increase in the nonlinear polarization model. Focusing on the temperatures next, we observe that although some differences appear in the tails of $T_{\parallel i}$ (solid blue in figure 16(c)), the profile is nearly identical to that obtained in the Boltzmann electron simulation with force softening (dotted line with circles in figure 6(c)). Likewise, the $T_{\perp i}$ profile in figure 16(d) is different in that it is augmented in the near-expander compared to the linearized polarization case (figure 14(d)), but the former is likely affected by force softening since such profiles follow the same trends as those in dotted-circle blue lines in figure 6.

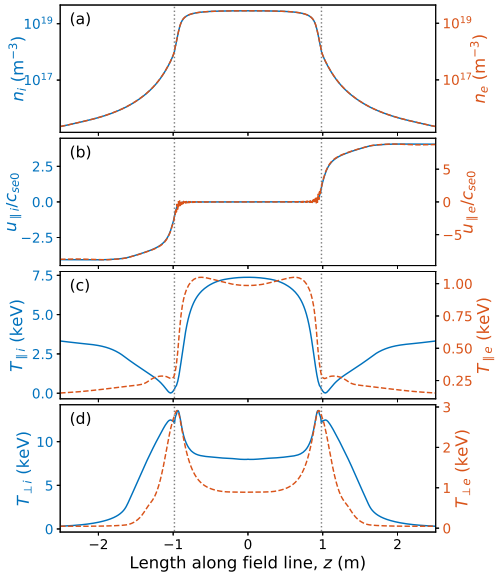

FIG. 16. Number density (a), mean flow speed (b), parallel (c) and perpendicular (d) temperature of the ion (solid blue) and electron (dashed orange) distribution functions at $t = 32\,\mu\text{s} \approx 1.78\nu_{ee}^{-1}$ in kinetic electron simulation with nonlinear polarization and force softening.

The difference in guiding center densities mentioned above is only responsible for a slight increase in the height of the potential profile, as shown by solid blue and green dotted lines in figure 17. At this time, the linear and nonlinear polarization simulations produce nearly identical profiles. In that same figure, we also compare the ϕ profiles with that obtained by the Boltzmann electron simulation. The potential drop between the center and the throat is somewhat similar in the Boltzmann electron and nonlinear polarization simulations, $3.87T_{e0}/e$ and $3.09T_{e0}/e$ (or $3.12T_e(z=0)/e$), respectively. The largest difference is in the value of the sheath potential and the potential drop seen in the expander ($|z| > z_m = 0.98\,\text{m}$). The absence of a potential drop in the expander is unlike what is seen in some GDT experiments,

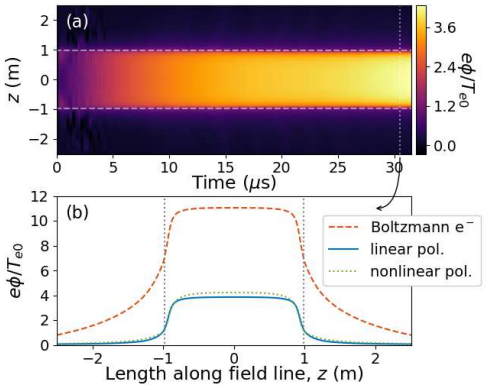

FIG. 17. (a) Electrostatic potential $\phi(z,t)$ in simulation with kinetic electrons, nonlinear polarization and force softening (mirror throats indicated with white dashed lines), and (b) electrostatic potential profile at $t = 32\,\mu\text{s} \approx 1.78\nu_{ee}^{-1}$, with the profiles from Boltzmann electron and linearized polarization kinetic electron simulations given for comparison. Note that the $\phi(z)$ variation in the Boltzmann electron case is not accurate for $|z| > z_m$ because Boltzmann assumptions break down in the expanders.

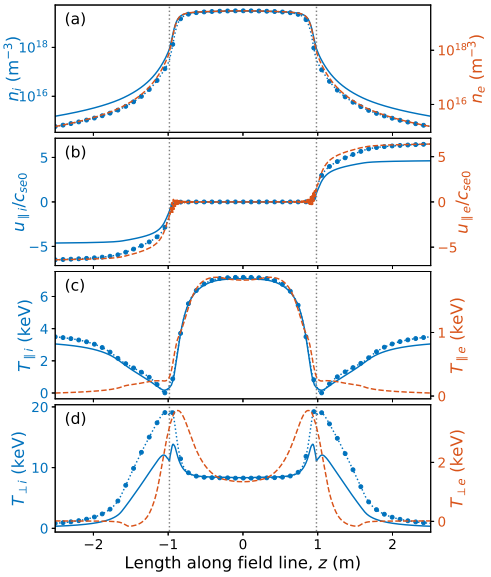

FIG. 18. (a) Guiding center density (n_s), (b) mean drift speed ($u_{\|s}$) normalized to $c_{se0} = \sqrt{T_{e0}/m_i}$, and (c) parallel and (d) perpendicular temperatures ($T_{\|s}$, $T_{\perp s}$) in kinetic electron simulation with nonlinear polarization (solid blue, dashed orange), and Boltzmann electron simulation (dotted blue with circles) at $t = 100\,\mu\text{s} \approx 5.56\nu_{ee}^{-1}$, both with force softening. Dotted vertical lines indicate mirror throats.

where $\phi(z = z_m) - \phi(z = L_z/2)$ carries most of the drop across the device depending on the expansion ratio of the magnetic field therein ($K_w = B_m/B(L_z/2)$)[20]. The Boltzmann electron model may be more accurate for the more collisional GDT, but is not suitable for the large K_w and collisionless regimes in WHAM[59], as discussed in section II B 3. Therefore the lack of a potential drop in the expander of kinetic electron simulations is not necessarily incorrect, although at this time ($t = 32\,\mu\text{s} = 1.78\nu_{ee}^{-1}$) the profiles have not stopped evolving, as can be appreciated from figure 17(a). And even in the recent work that estimated WHAM's $\phi(z)$ using semi-analytical methods[25], no potential drop was seen in the expander.

C. Ambipolar potential development

One of the beneifts of the Boltzmann electron model and kinetic electron models with force softening is the ability to run them for a much longer time due to their lower computational cost. This allows better assessments of what the steady state profiles look like and better approximations of an equilibrium that could be used for 3D turbulence calculations in the future. We thus time-integrated these two models up to $t = 100\,\mu\text{s} \approx 5.56\nu_{ee}^{-1}$. As noted in the previous section, the resolution along $v_\|$ had to be increased in the nonlinear polarization simulation, bringing the cost of this longer simulation to 749.8 hours on 288 cores. And to make a fairer comparison, we ran a second Boltzmann electron simulation with the same $288 \times 96 \times 192$ resolution as the nonlinear polarization simulation for 14.73 hours on 288 cores (a little less than a factor of $\sqrt{m_i/m_e} \approx 60$ difference).

These two simulations developed similar ion guiding center density and parallel temperature profiles (solid blue and dotted-circled blue in figures 18(a,c)), aside from a larger drop in the expander n_i of the Boltzmann electron simulation. Additional quantitative differences are found in the speed ions accelerate to within the expander, and in $T_{\perp i}$ near the mirror throats which as explained below may be affected by force softening. One of the most contrasting results is the large $T_{\perp e}/T_{\|e}$ ratio near the mirror throats given that, owing to their frequent collisions, we would expect the electron f_s to be close to isotropic. Near the center of the plasma, this ratio, $1.35/1.82 \approx 0.74$, is not far from unity, but at the mirror throat, it rises to $3.76/0.9 \approx 4.18$. It is possible, although it remains to be shown, that since the structure of f_e in $z - \mu$ is different to f_i the force softening function χ that does not incorporate the effect of the electrostatic potential is causing some of this modification of $T_{\perp e}$ near the mirror throat. Future numerical experiments are planned to explore this possibility.

Another noticeable feature of the electron temperatures in figure 18(c,d) is that the scalar temperature, $T_e = (T_{\|e} + 2T_{\perp e})/3$, has risen considerably over the $T_{e0} = 940\,\text{eV}$ reference temperature. And this phenomenon has an impact on a vital metric of this study, quantifying whether the ambipolar potential developed is strong enough to confine the elec-

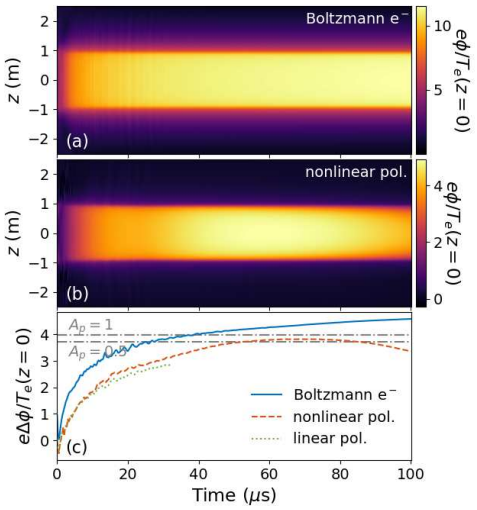

FIG. 19. Spatio-temporal evolution of the electrostatic potential in Boltzmann electron simulation (top), and kinetic electron simulation with nonlinear polarization (middle). The potential drop between the mirror center and throats ($\Delta\phi$) normalized by the central electron temperature ($T_e(z=0)$) is shown as a function of time (bottom). The $\Delta\phi$ estimated from the Pastukhov loss rates are indicated with horizontal grey dash-dot lines.

trons. Figure 19 shows the evolution of the ϕ profiles for the Boltzmann and nonlinear polarization simulations. The bottom panel provides the potential drop between the center and the throats normalized to the local electron temperature. The first thing to notice is that the Boltzmann electron model surpasses the semi-analytic estimate of $e\Delta\phi/T_{e0} = 3.98$ obtained at the beginning of section IV. As discussed previously, Boltzmann electrons imply high collisionality and can thus lead to larger potential drops, hence why the solid blue line surpasses the grey dash-dot $A_p = 1$ line in figure 19(c). On the other hand, the nonlinear polarization simulation (dashed orange line) also attained a $\Delta\phi$ comparable to the $3.72T_{e0}/e$ estimate obtained earlier (with $A_p = 0.5$) by $t \approx 50\,\mu\text{s} \approx 2.78\nu_{ee}^{-1}$. However, we see this curve downturn later and dip below this semi-analytic estimate. Although it is still within the expected range of several T_e/e, this dip is because the electron temperature in the nonlinear polarization simulation continues to increase at this time. If we instead had normalized $e\Delta\phi$ to T_{e0} in figure 19, we would have seen the orange dashed curve follow a similar trend as the blue curve for the Boltzmann electron simulation. We also include the potential drop in the linear polarization kinetic electron simulation in dotted green, which was not time-integrated as long due to its increased computational cost but seems to follow a similar trend to the nonlinear polarization model.

The tentative conclusion here is that both the Boltzmann electron and the kinetic electron models develop a potential profile with sufficient height to confine the electrons, with two caveats. First, as discussed in section IV A, the build up of the Boltzmann electron potential appears to happen on the ion transit time scale and is thus associated with the escape of particles that where initially places in the loss cone, and that are injected into the loss cone by the source. Even though it is caused by a different mechanism, this potential is comparable to the Pastukhov estimate. Furthermore, since the early rise in $e\Delta\phi/T_e(z=0)$ has a similar qualitative aspect in the kinetic electron simulation it is possible that the $\phi(z)$ profile there is built by a similar phenomenon. As mentioned in section III C, reproducing the Pastukhov mechanism will require much longer simulations with computational improvements that we intend to leverage in subsequent work. The second caveat is that the kinetic electron simulation continues to heat, an aspect that will be investigated in detail in future work.

V. SUMMARY

In this work we strove to understand the computational challenges of studying high-field mirrors with large mirror ratios using a continuum gyrokinetic model, and to determine if the model used produces the ambipolar potential (ϕ) necessary to confine the electrons (i.e. comparable to a Pastukhov potential estimate). High accuracy estimations of ϕ require longer simulations (of $O(\nu_{ii}^{-1})$ seconds) for which bounce-averaged Fokker-Planck or implicit methods are better suited, so that particle loss rates reach steady state in the presence of a self-consistent potential. Our main interest is to eventually simulate low-frequency turbulence (along with possible stabilization mechanisms) that saturates on much shorter time scales. In this vein, we employed the long wavelength gyrokinetic solver in the `Gkeyll` code since it is capable of future higher dimensional, turbulence simulations. Three different approaches to computing the potential were used: isothermal Boltzmann electrons with ambipolar sheaths, kinetic electrons with a linearized polarization, and kinetic electrons with a nonlinear polarization. This work is unique in that, compared to other efforts, it uses realistic WHAM parameters, simulates the entire plasma, including the expanders, incorporates the effects of collisions and contains kinetic electron simulations (including a sheath model).

This manuscript also presents a novel Hamiltonian-structure-preserving force softening strategy to mitigate the small time step associated with the strong mirror force produced by HTS coils. This technique accelerated Boltzmann electron simulations by a factor of 19.5 and had the added benefit of removing a numerical accumulation of f_i resulting from the finite velocity space extents. It was shown that the resulting ambipolar potential with and without force softening was the same, buttressing justification for its use. However, other metrics like the perpendicular temperature exhibit modifications that may be attributed to the use of force softening. Future work will explore these modifications further; one improvement, for example, is to include an estimate of the potential profile (e.g. obtained through other codes or semianalytic

methods) in the design of the softening function χ.

Other computational challenges encountered in applying the `Gkeyll` continuum gyrokinetic solver to the HTS mirror environment include the long integration times to build the equilibrium potential, the high-resolution grids needed to resolve colossal changes in the distribution function across the entire machine, and the small time step that the ω_H mode also imposes. In future 1D and higher dimensional simulations, we will start from an equilibrium obtained via faster means, either `Gkeyll` Boltzmann electron simulations, semi-analytic methods[25], or bounce-averaged Fokker-Planck codes. In that case, 1D simulations can verify that the system stays close to such an equilibrium, and higher dimensional simulations will integrate for much shorter time periods (e.g. the interchange time scale $\sim 1\,\mu$s). Additional algorithmic improvements are also being implemented in `Gkeyll`, such as nonuniform grids and additional parallelism, which we estimate can speed up the code by a factor of 10-15. Lastly, there are semi-implicit algorithms that could be explored to overcome the ω_H restriction on Δt.

All in all, the Boltzmann electron and nonlinear polarization kinetic electron simulations with force softening were performed out to $t = 100\,\mu\text{s} \approx 5.56\nu_{ee}^{-1}$. It was shown that they developed an electrostatic potential comparable to the analytic Pastukhov estimate[13–15]. This means that the gyrokinetic model used does evolve towards an equilibrium that confines the electrons and that, in the future, when we pursue turbulence studies about an externally computed equilibrium, the system will not deviate from such equilibrium. Note, however, that initial rapid buildup of the potential is due to slowing down electron losses (in either the Boltzmann or the kinetic electron case) to match the escaping ions that were originally in the loss cone in the initial condition. After several ion transit times, the potential continues to rise in order to balance ions that are lost by pitch angle scattering from the trapped part of phase space into the loss cone and some ions directly injected into the loss cone by the Maxwellian, though fully getting to steady state would require simulations that last for an ion collision period. Another caveat is that the nonlinear polarization kinetic electron simulation exhibited late-stage electron heating, causing $e\Delta\phi/T_e(z=0)$ to decrease some; exploring the origin of this heating is planned for our immediate future work. Additionally, as an extra check on these two simulations, we also pursued kinetic electron simulations with a linearized polarization and no force softening. However, this simulation required a much smaller Δt and was only advanced for a third of the time of the other two. Thus far, the linearized polarization model appears to track the nonlinear polarization model, providing some confidence in the nonlinear polarization result. Finally, we remind the reader that beyond the computational and field model improvements discussed, the physics model may need considerable enhancements to achieve predictive capabilities. For example, an essential ingredient of WHAM dynamics is the presence of sloshing ions due to their modification of the pressure and potential profiles and their effect on plasma instabilities. The current collision model (Dougherty) may also need improvement in order to more closely approximate the physics captured by the LRO. These are left for future work.

ACKNOWLEDGMENTS

We thank Ian Abel and Felix Parra for sharing their insights on this topic and express our gratitude towards other members of the `Gkeyll` and WHAM teams who aided this work. We used the Stellar cluster at Princeton University. M.F., A.H. and G.W.H. were supported by the Partnership for Multiscale Gyrokinetic Turbulence (MGK) and the High-Fidelity Boundary Plasma Simulation (HBPS) projects, part of the U.S. Department of Energy (DOE) Scientific Discovery Through Advanced Computing (SciDAC) program, and the DOE's ARPA-E BETHE program, via DOE contract DE-AC02-09CH11466 for the Princeton Plasma Physics Laboratory.

DATA AVAILABILITY STATEMENT

Raw data were generated at PPPL/Princeton University Stellar computer cluster. The derived data suppporting this study's findings are openly available in Zenodo[67] at https://doi.org/10.5281/zenodo.8125802.

Appendix A: Energy conservation of 1D gyrokinetic models

The kinetic electron models in section II B conserve the total energy[47]

$$W_{\text{tot}} = W_H - L_f = \sum_s \int \mathrm{d}^3\boldsymbol{z}\, JB_\parallel^* f_s H_s - L_f, \qquad \text{(A1)}$$

where $\mathrm{d}^3\boldsymbol{z} = \mathrm{d}z\mathrm{d}\boldsymbol{w}$ and L_f is the field part of the Lagrangian. This part, and the Hamiltonian H, needs to be suitably defined depending on which field model is used, as shown below. Note that in both cases L_f does not include the familiar term proportional to $\varepsilon_0|\boldsymbol{E}|^2/(8\pi)$ because we order that as small in the Poisson equation and use quasineutrality instead.

1. Linear polarization

When using the gyrokinetic model consisting of equations 7-8, 19, we employ the lower order Hamiltonian $H = m_s v_\parallel^2/2 + \mu B + q_s\phi$. However to obtain a field equation for ϕ and have a conserved total energy, one must employ the field Lagrangian $L_f = \sum_s \int \mathrm{d}z J[m_s n_0/(2B_p^2)]\,|\nabla_\perp\phi|^2$, such that the total conserved energy is

$$W_{\text{tot}} = W_H - \int \mathrm{d}z J \frac{\varepsilon_\perp}{2}\,|\nabla_\perp\phi|^2, \qquad \text{(A2)}$$

where the linear polarization model uses $\varepsilon_\perp = \sum_s m_s n_0/B_p^2$ and replaces $\nabla_\perp\phi \to -k_\perp\phi$ in the last term. The time evolution of W_H given by

$$\frac{dW_H}{dt} = \int \mathrm{d}z J \sum_s \left(\int \mathrm{d}\boldsymbol{w}\, B_\parallel^* \frac{\partial f_s}{\partial t} H_s + q_s n_s \frac{\partial\phi}{\partial t} \right). \qquad \text{(A3)}$$

The contribution from the first term can be obtained by multiplying the gyrokinetic equation 7 by H and integrating over all phase space (disregarding collisions since they conserve energy[45])

$$\sum_s \int \mathrm{d}^3\boldsymbol{z}\, JB_\parallel^* \frac{\partial f_s}{\partial t} H_s = \sum_s \int \mathrm{d}^3\boldsymbol{z} \left[-\frac{\partial}{\partial z}\left(v_\parallel f_s\right) + \frac{1}{m_s}\frac{\partial H_s}{\partial z}\frac{\partial f_s}{\partial v_\parallel} + JB_\parallel^* S_s \right] H_s. \tag{A4}$$

Integrating the second term by parts leads us to

$$\sum_s \int \mathrm{d}^3\boldsymbol{z}\, JB_\parallel^* \frac{\partial f_s}{\partial t} H_s = \sum_s \int \mathrm{d}^3\boldsymbol{z} \left[-\frac{\partial}{\partial z}\left(v_\parallel f_s\right) + JB_\parallel^* S_s \right] H_s + \sum_s \frac{2\pi}{m_s^2} \int \mathrm{d}z\, \mathrm{d}\mu \frac{\partial H_s}{\partial z} f_s H_s \Big|_{v_{\parallel\min}}^{v_{\parallel\max}} - \sum_s \int \mathrm{d}^3\boldsymbol{z} \frac{\partial H_s}{\partial z}\frac{f_s}{m_s}\frac{\partial H_s}{\partial v_\parallel}. \tag{A5}$$

The second term on the right side vanishes due to zero-flux BCs along $v_\parallel$, and the expression can be consolidated into

$$\sum_s \int \mathrm{d}^3\boldsymbol{z}\, JB_\parallel^* \frac{\partial f_s}{\partial t} H_s = \sum_s \int \mathrm{d}^3\boldsymbol{z} \left[-v_\parallel \frac{\partial}{\partial z}\left(f_s H_s\right) + JB_\parallel^* S_s H_s \right] = -\sum_s \int \mathrm{d}\boldsymbol{w}\, v_\parallel f_s H_s \Big|_{-L_z/2}^{L_z/2} + \sum_s \int \mathrm{d}^3\boldsymbol{z}\, JB_\parallel^* S_s H_s. \tag{A6}$$

With the use of equations A3 and A6, the time derivative of equation A2 yields the following total energy time rate of change

$$\frac{dW_{\mathrm{tot}}}{dt} = -\sum_s \int \mathrm{d}\boldsymbol{w}\, v_\parallel f_s H_s \Big|_{-L_z/2}^{L_z/2} + \sum_s \int \mathrm{d}^3\boldsymbol{z}\, JB_\parallel^* S_s H_s + \int \mathrm{d}z J \sum_s q_s n_s \frac{\partial \phi}{\partial t} - \int \mathrm{d}z J \varepsilon_\perp k_\perp \phi \frac{\partial}{\partial t} k_\perp \phi. \tag{A7}$$

Now replace $\sum_s q_s n_s$ using the field equation 19 causing the last two terms to cancel each other, and obtain

$$\frac{dW_{\mathrm{tot}}}{dt} = -\sum_s \int \mathrm{d}\boldsymbol{w}\, v_\parallel f_s H_s \Big|_{-L_z/2}^{L_z/2} + \sum_s \int \mathrm{d}^3\boldsymbol{z}\, JB_\parallel^* S_s H_s. \tag{A8}$$

Therefore, any change in the total energy of the system is only caused by the energy fluxes through the sheath entrance (first term in equation A8) or by the sources (second term in equation A8).

2. Nonlinear polarization

The energy theorem for the model with a nonlinear polarization density proceeds in a similar way, except that in this case $L_f = 0$ and we must use the higer-order Hamiltonian $H = m_s v_\parallel^2/2 + \mu B + q_s\phi - m_s\left(k_\perp\phi/B_p\right)^2/2$. Therefore the time rate of change of the total energy is therefore

$$\frac{dW_H}{dt} = \int \mathrm{d}z J \sum_s \left[\int \mathrm{d}\boldsymbol{w}\, B_\parallel^* \frac{\partial f_s}{\partial t} H_s + n_s \left(q_s - m_s \frac{k_\perp^2 \phi}{B_p^2} \right) \frac{\partial \phi}{\partial t} \right]. \tag{A9}$$

Similar arguments as in the previous subsection reduce the first term on the right to the right side of equation A6, such that our total energy rate of change in this case is

$$\frac{dW_{\mathrm{tot}}}{dt} = -\sum_s \int \mathrm{d}\boldsymbol{w}\, v_\parallel f_s H_s \Big|_{-L_z/2}^{L_z/2} + \sum_s \int \mathrm{d}^3\boldsymbol{z}\, JB_\parallel^* S_s H_s + \int \mathrm{d}z J \sum_s n_s \left(q_s - m_s \frac{k_\perp^2 \phi}{B_p^2} \right) \frac{\partial \phi}{\partial t}. \tag{A10}$$

Using the field equation 20 to replace $\sum_s q_s n_s$ in the term on the right causes the round bracket to vanish, and we arrive at equation A8 again, i.e. energy change is only caused by boundary fluxes or sources.

Appendix B: Electrostatic shear Alfvén or ω_H modes

1. Linear polarization

In the electrostatic limit the equations in our model contain a high frequency wave mode that is usually named the electrostatic shear Alfvén or ω_H mode. In order to get an estimate of its frequency, we consider the electrostatic, collisionless slab limit of equation 7 without sources and gradients in B. That is:

$$\frac{\partial f_s}{\partial t} + \frac{\partial}{\partial z}\left(v_\parallel f_s\right) - \frac{\partial}{\partial v_\parallel}\left(\frac{q_s}{m_s}\frac{\partial \phi}{\partial z} f_s \right) = 0. \tag{B1}$$

By linearizing this equation about an instantaneous Maxwellian equilibrium (f_{s0}) with zero electrostatic potential ($\phi_0 = 0$), we obtain an equation for the perturbation f_{s1}:

$$\frac{\partial f_{s1}}{\partial t} + \frac{\partial}{\partial z}\left(v_\parallel f_{s1}\right) - \frac{\partial}{\partial v_\parallel}\left(\frac{q_s}{m_s}\frac{\partial \phi_1}{\partial z} f_{s0} \right) = 0. \tag{B2}$$

We assumed that the spatial variation in the Maxwellian f_{s0} with density $n_{s0}(z,t)$ and temperature T_{s0} is very weak compared to the strong inhomogeneity induced by this mode, i.e. $k_\parallel n_{s0}(z,t)/\left|\partial_z n_{s0}(z,t)\right| \gg 1$, where $k_\parallel$ is a mode wave number along the field line. The $v_\parallel$ derivative is trivially calculated given the Maxwellian form of f_{s0}, yielding

$$\frac{\partial f_{s1}}{\partial t} + \frac{\partial}{\partial z}\left(v_\parallel f_{s1}\right) + \frac{q_s}{m_s}\frac{\partial \phi_1}{\partial z}\frac{v_\parallel}{v_{ts0}^2} f_{s0} = 0. \tag{B3}$$

We can now employ the ansatz $f_{s1} = \hat{f}_{s1}\exp\left(-i\omega t + ik_\parallel z\right)$ and $\phi_1 = \hat{\phi}_1 \exp\left(-i\omega t + ik_\parallel z\right)$, to simplify equation B3 to

$$-i\omega f_{s1} + ik_\parallel v_\parallel f_{s1} + \frac{q_s}{m_s} ik_\parallel \phi_1 \frac{v_\parallel}{v_{ts0}^2} f_{s0} = 0. \tag{B4}$$

In order to make further progress the relationship between f_{s1} and ϕ_1 must be exploited. We assume electrons and ions are in quasineutral equilibrium. In that case, the field equation with a linearized polarization simply states that

$$k_\perp^2 \sum_s \frac{n_0 m_s}{B_p^2}\phi_1 = \sum_s q_s n_{s1}. \tag{B5}$$

We further assume (one may check a posteriori) that the ions are too heavy and slow to respond to this fast electrostatic wave so that we can assume that they are static. Thus only the electron evolution need be considered with equations B4-B5, which may be combined to yield

$$\left(\int \mathrm{d}\boldsymbol{w}\, B_\parallel^* \frac{q_e^2}{m_e v_{te0}^2} \frac{k_\parallel v_\parallel}{\omega - k_\parallel v_\parallel} f_{e0} - k_\perp^2 \frac{n_0 m_i}{B_p^2}\right) \phi_1 = 0. \quad \text{(B6)}$$

For this electrostatic wave to exist the term inside the brackets must vanish. Furthermore, we may perform the μ integral since the dependence on this variable is only through the Maxwellian equilibrium f_{e0}:

$$\frac{q_e^2}{m_e v_{te0}^2} \int \mathrm{d}v_\parallel \frac{k_\parallel v_\parallel}{\omega - k_\parallel v_\parallel} f_{e0\parallel} - k_\perp^2 \frac{n_0 m_i}{B_p^2} = 0, \quad \text{(B7)}$$

and $f_{e0\parallel}$ is a Maxwellian in $v_\parallel$ with $n_{e0}(z,t)$ and T_{e0} density and temperature, respectively. We can write this in terms of the plasma dispersion function

$$k_\perp^2 \frac{m_i}{B_p^2} + \frac{q_e^2}{m_e v_{te0}^2} \frac{n_{e0}(z,t)}{n_0} \left[1 + \frac{\omega}{\sqrt{2} v_{te0} k_\parallel} Z\left(\frac{\omega}{\sqrt{2} v_{te0} k_\parallel}\right)\right] = 0. \quad \text{(B8)}$$

Expanding the plasma dispersion function to first order in $\omega/(\sqrt{2} v_{te0} k_\parallel) \gg 1$, we obtain

$$\omega = \omega_H = \frac{v_{te0} k_\parallel}{k_\perp \rho_{s0}} \sqrt{\frac{n_{e0}(z,t)}{n_0}}. \quad \text{(B9)}$$

2. Nonlinear polarization

In this case we make a similar analysis as in the previous section, with the modification that we allow incorporate the instantaneous spatial variation of the density profiles into the polarization density:

$$k_\perp^2 \sum_s \frac{n_{s0}(z,t) m_s}{B_p^2} \phi_1 = \sum_s q_s n_{s1}. \quad \text{(B10)}$$

Again we highlight that the spatial and temporal variation implied by the arguments of $n_{s0}(z,t)$ is much weaker than that of the ω_H mode, allowing us to perform a strictly local linear analysis about the $n_{s0}(z,t)$ background density. The rest of the derivation proceeds as before, leading to the dispersion relation

$$k_\perp^2 \frac{m_i}{B_p^2} + \frac{q_e^2}{m_e v_{te0}^2} \frac{n_{e0}(z,t)}{n_{i0}(z,t)} \left[1 + \frac{\omega}{\sqrt{2} v_{te0} k_\parallel} Z\left(\frac{\omega}{\sqrt{2} v_{te0} k_\parallel}\right)\right] = 0, \quad \text{(B11)}$$

whose high frequency limit is

$$\omega = \omega_H = \frac{v_{te0} k_\parallel}{k_\perp \rho_{s0}} \sqrt{\frac{n_{e0}(z,t)}{n_{i0}(z,t)}}. \quad \text{(B12)}$$

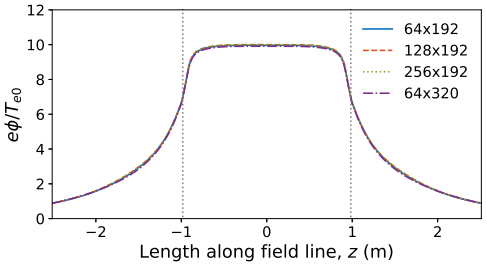

FIG. 20. Electrostatic potential profile at $t = 10.5\,\mu$s in Boltzmann electron simulations with $N_z = 288$ and several $N_{v_\parallel} \times N_\mu$ resolutions.

Appendix C: Resolution scan

In order to arrive at the lowest possible resolution that would produce acceptable results we tried several resolutions during the course of this work. We note that when we first attempted kinetic electron simulations, the simulations were not stable if $N_z < 256$. Catastrophic oscillations appeared near the mirror throats when we used fewer than 256 cells. This is presumably due to large gradients in f_s that occur with a high mirror ratio, leading to regions of $f_s < 0$. `Gkeyll` can tolerate some f_s negativity but, if it gets too strong, unphysical instabilities can arise and cause the simulation to diverge. A positivity-preserving algorithm, mentioned in section III C, would help prevent such instabilities and allow the use of coarser grids to produce useful results. It is possible that such instabilities were exacerbated by incorrect velocity resolutions used initially (more on this below), and that once a more appropriate $N_{v_\parallel} \times N_\mu$ was selected a lower N_z could be used. We have not yet explored that possibility, but will in the future. For this manuscript the number of cells along z was later increased to 288 because the simulations were carried out in nodes with 96 2.9 GHz Intel Cascade Lake cores, so this allowed us to parallelize across 3 nodes in a balanced manner with a minor increase in computational cost.

After establishing the position-space resolution, we performed a limited scan of the velocity space resolution. These simulations were only run for a few microseconds (see figure captions) given their considerable cost, especially at higher resolution. Four Boltzmann electron simulations with the resolutions $N_{v_\parallel} \times N_\mu = \{64 \times 192, 128 \times 192, 256 \times 192, 64 \times 320\}$ were performed up to $10.5\,\mu$s. As can be seen from figure 20 the electrostatic potential profile did not change for any of these resolutions. The velocity moments of the ion distribution (n_i, $u_{\parallel i}$, $T_{\parallel i}$ and $T_{\perp i}$) also were relatively unaffected by the various resolutions employed here (figure 21). We should note that these are ion profiles whose steady state is likely not reached at this point, but we had to make an assessment of the resolution requirements with the simulation time that our resources allowed.

Future Boltzmann electron simulations could possibly be run longer (incorporating computational improvements men-

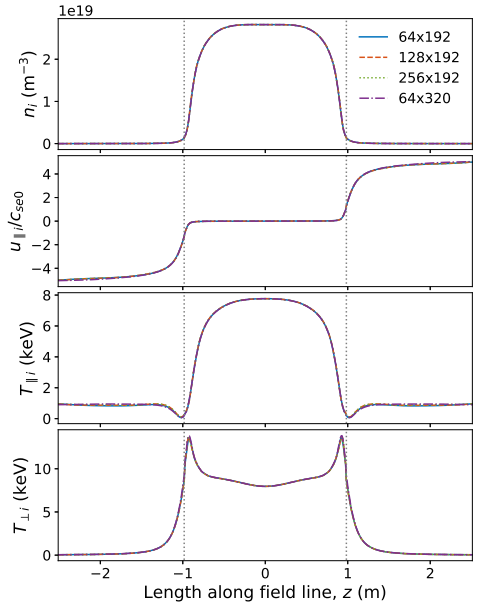

FIG. 21. Ion number density (n_i), mean parallel speed ($u_{\parallel i}$) normalized to $c_{se0} = \sqrt{T_{e0}/m_i}$, and parallel and perpendicular temperatures ($T_{\parallel i}$, $T_{\perp i}$) at $t = 10.5\,\mu$s in Boltzmann electron simulations with $N_z = 288$ and several $N_{v_\parallel} \times N_\mu$ resolutions.

tioned in section III C) or with lower resolution. For now we have opted to carry on with $N_z \times N_{v_\parallel} \times N_\mu = 288 \times 64 \times 192$ as our baseline, especially given some of the findings when scanning resolution with kinetic electrons. Our kinetic electron resolution scan used the linearized polarization model with $k_\perp \rho_s = 0.01$ (and no force softening), and were run until $t = 6\,\mu$s. Note that this is a more demanding $k_\perp \rho_s$ choice than the $k_\perp \rho_s = 0.06$ estimated for WHAM with $B_p = 0.86$ (see section IV B) due to the ω_H mode; nonlinear polarization with a higher $k_\perp \rho_s$ could be used in the future to carry out these convergence tests and other simulations much more quickly. Once again we kept the z resolution fixed at 288 cells, and proceeded to vary $N_{v_\parallel} \times N_\mu$. This scan produced the electrostatic potential profiles in figure 22; it shows that regardless of $N_{v_\parallel} = 64 - 384$, if the μ resolution is kept low (32 cells) a considerably higher central potential is produced. Only when $N_\mu \geq 64$ do we see $\phi(z = 0)$ begin to asymptote, but approaching convergence in the expander seems to further necessitate $N_\mu \geq 128$. An justification of such high resolution μ grids was offered in section III, and ideas to improve on this with variable μ grids were discussed in section III C.

The ion velocity moments were also examined for each of these simulations (figure 23). We first notice that unlike the Boltzmann electron simulations there is more variability with

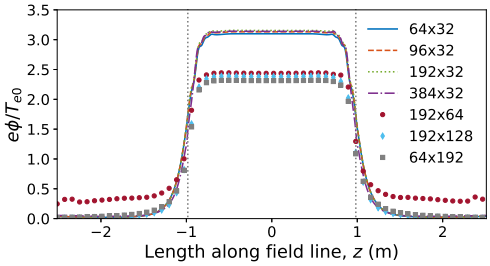

FIG. 22. Electrostatic potential profile at $t = 6\,\mu$s in linearized polarization kinetic electron simulations with $N_z = 288$ and several $N_{v_\parallel} \times N_\mu$ resolutions.

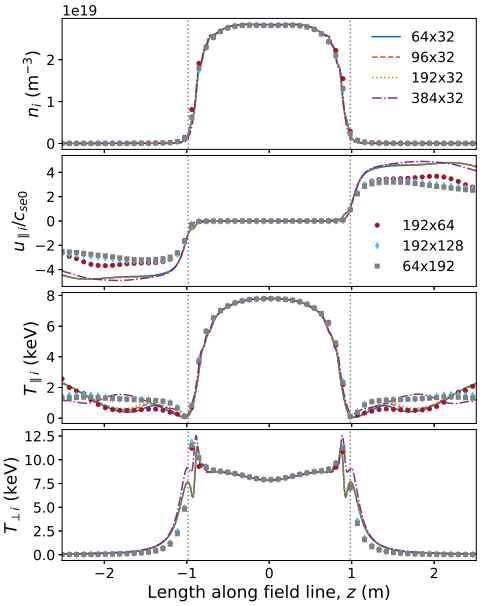

FIG. 23. Ion number density (n_i), mean parallel speed ($u_{\parallel i}$) normalized to $c_{se0} = \sqrt{T_{e0}/m_i}$, and parallel and perpendicular temperatures ($T_{\parallel i}$, $T_{\perp i}$) at $t = 6\,\mu$s in linearized polarization kinetic electron simulations with $N_z = 288$ and several $N_{v_\parallel} \times N_\mu$ resolutions.

resolution here, although it is possible that is simply caused by these snapshots being taken earlier in time. As with the potential profiles, we see that some features take a noticeable leap when going from $N_\mu = 32$ to $N_\mu = 64$; see for example the ion parallel speed in figure 23(b). An additional but smaller change is obtained when μ resolution is further increased to 128 cells. Similar trends are seen in the electron velocity moments (figure 24), which led us to conclude that a

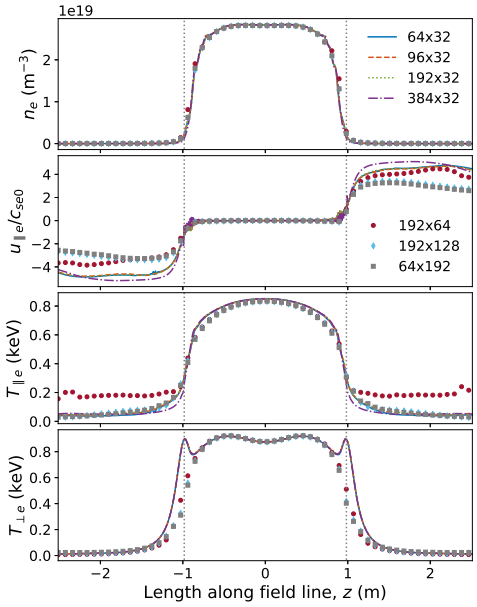

FIG. 24. Electron number density (n_e), mean parallel speed ($u_{\parallel e}$) normalized to $c_{se0} = \sqrt{T_{e0}/m_i}$, and parallel and perpendicular temperatures ($T_{\parallel e}$, $T_{\perp e}$) at $t = 6\,\mu$s in linearized polarization kinetic electron simulations with $N_z = 288$ and several $N_{v_\parallel} \times N_\mu$ resolutions.

$288 \times 64 \times 192$ grid was the most suitable for this study. Note that the velocity grids do not have to be the same for both species, and in the future it is possible that the cost can be further reduced by using a coarser mesh for ions.

[1] National Academies of Sciences, Engineering, and Medicine, "Bringing Fusion to the U.S. Grid," (2021), Washington, DC: The National Academies Press.

[2] A. J. Creely, M. J. Greenwald, S. B. Ballinger, D. Brunner, J. Canik, J. Doody, T. Fülöp, D. T. Garnier, R. Granetz, T. K. Gray, and et al., "Overview of the SPARC tokamak," Journal of Plasma Physics **86**, 865860502 (2020).

[3] R. Volberg, D. Anderson, J. Canik, P. Harris, and C. Hegna, "The high field stellarator path to commercial fusion energy," Bulletin of the American Physical Society (2022).

[4] T. Qian, M. Zarnstorff, D. Bishop, A. Chamblis, A. Dominguez, C. Pagano, D. Patch, and C. Zhu, "Simpler optimized stellarators using permanent magnets," Nuclear Fusion **62**, 084001 (2022).

[5] D. D. Ryutov, H. L. Berk, B. I. Cohen, A. W. Molvik, and T. C. Simonen, "Magneto-hydrodynamically stable axisymmetric mirrors," Physics of Plasmas **18**, 092301 (2011).

[6] T. C. Simonen, R. H. Cohen, D. L. Correll, K. Fowler, D. E. Post, H. L. Berk, W. Horton, E. B. Hooper, N. J. Fisch, A. B. Hassam, D. E. Baldwin, D. Pearlstein, G. B. Logan, B. Turner, R. W. Moir, A. W. Molvik, D. Ryutov, A. A. Ivanov, J. W. Kesner, B. I. Cohen, H. S. McLean, T. Tamano, X. Tang, and T. Imai, "The axisymmetric tandem mirror: A magnetic mirror concept game changer magnet mirror status study group," in *The Status of Research Regarding Magnetic Mirrors as a Fusion Neutron Source or Power Plant* (2008).

[7] T. Fowler, R. Moir, and T. Simonen, "A new simpler way to obtain high fusion power gain in tandem mirrors," Nuclear Fusion **57**, 056014 (2017).

[8] J. Anderson, M. Clark, C. Forest, B. Geiger, V. Mirnov, S. Oliva, J. Pizzo, O. Schmitz, J. Wallace, G. Kristofek, R. Mumgaard, E. Peterson, A. Ram, D. Whyte, J. . Wright, S. Wukitch, D. Green, R. Harvey, Y. V. Petrov, B. Srinivisan, and A. Hakim, "Introducing the Wisconsin HTS Axisymmetric Mirror," in *APS Division of Plasma Physics Meeting Abstracts*, APS Meeting Abstracts, Vol. 2020 (2020) p. CP20.003.

[9] D. Endrizzi, J. K. Anderson, P. Catto, K. Furlong, R. Harvey, Y. Petrov, J. Pizzo, T. Qian, K. Sanwalka, J. Wallace, M. Yu, and C. B. Forest, "Physics Basis of the Wisconsin HTS Axisymmetric Mirror (WHAM) on the Tandem Mirror path to Fusion," (2023), in preparation.

[10] P. A. Bagryansky, A. G. Shalashov, E. D. Gospodchikov, A. A. Lizunov, V. V. Maximov, V. V. Prikhodko, E. I. Soldatkina, A. L. Solomakhin, and D. V. Yakovlev, "Threefold increase of the bulk electron temperature of plasma discharges in a magnetic mirror device," Phys. Rev. Lett. **114**, 205001 (2015).

[11] D. Whyte, "Small, modular and economically attractive fusion enabled by high temperature superconductors," Philosophical Transactions of the Royal Society A: Mathematical, Physical and Engineering Sciences **377**, 20180354 (2019).

[12] D. E. Baldwin, "End-loss processes from mirror machines," Rev. Mod. Phys. **49**, 317–339 (1977).

[13] V. Pastukhov, "Collisional losses of electrons from an adiabatic trap in a plasma with a positive potential," Nuclear Fusion **14**, 3 (1974).

[14] R. Cohen, M. Rensink, T. Cutler, and A. Mirin, "Collisional loss of electrostatically confined species in a magnetic mirror," Nuclear Fusion **18**, 1229 (1978).

[15] D. Chernin and M. Rosenbluth, "Ion losses from end-stoppered mirror trap," Nuclear Fusion **18**, 47 (1978).

[16] J. Killeen, A. A. Mirin, and M. E. Rensink, "The solution of the kinetic equations for a multispecies plasma," in *Controlled Fusion*, Methods in Computational Physics: Advances in Research and Applications, Vol. 16, edited by J. Killeen (Elsevier, 1976) pp. 389–431.

[17] R. Post, "The magnetic mirror approach to fusion," Nuclear Fusion **27**, 1579 (1987).

[18] M. Yoshikawa, J. Kohagura, R. Ikezoe, M. Sakamoto, N. Ezumi, R. Minami, M. Hirata, A. Terakado, K. Nojiri, S. Jang, A. Tanaka, M. Ichimura, T. Imai, and Y. Nakashima, "Suppression of flute-like fluctuation by potential formation in GAMMA 10/PDX," Nuclear Fusion **59**, 076031 (2019).

[19] P. A. Bagryansky, A. V. Anikeev, M. A. Anikeev, A. Dunaevsky, E. D. Gospodchikov, A. A. Ivanov, A. A. Lizunov, O. A. Korobeynikova, M. S. Korzhavina, Y. V. Kovalenko, V. V. Maximov, S. V. Murakhtin, E. I. Pinzhenin, V. V. Prikhodko, V. Y. Savkin, A. G. Shalashov, E. I. Soldatkina, A. L. Solomakhin, D. V. Yakovlev, P. Yushmanov, and K. V. Zaytsev, "Recent progress of plasma confinement and heating studies in the gas dynamic trap," AIP Conference Proceedings **1771**, 020003 (2016).

[20] A. A. Ivanov and V. V. Prikhodko, "Gas-dynamic trap: an overview of the concept and experimental results," Plasma Physics and Controlled Fusion **55**, 063001 (2013).

[21] A. A. Ivanov and V. V. Prikhodko, "Gas dynamic trap: experimental results and future prospects," Physics-Uspekhi **60**, 509 (2017).

[22] A. Lizunov, V. Maximov, and A. Sandomirsky, "Evaluation of ambipolar potential barrier in the gas dynamic trap by doppler spectroscopy," Nuclear Fusion **62**, 076003 (2022).

[23] B. A. Wetherton, A. Le, J. Egedal, C. Forest, W. Daughton, A. Stanier, and S. Boldyrev, "A drift kinetic model for the expander region of a magnetic mirror," Physics of Plasmas **28**, 042510 (2021).

[24] M. Jimenez, A. I. Smolyakov, O. Chapurin, and P. Yushmanov, "Ion kinetic effects and instabilities in the plasma flow in the magnetic mirror," Physics of Plasmas (accepted) **29**, 000000 (2022).

[25] J. Egedal, D. Endrizzi, C. Forest, and T. Fowler, "Fusion by beam ions in a low collisionality, high mirror ratio magnetic mirror," Nuclear Fusion **62**, 126053 (2022).

[26] R. F. Post, "The "Kinetic Stabilizer": A Simpler Tandem Mirror Configuration?" Fusion Technology **39**, 25–32 (2001).

[27] V. V. Arsenin and V. A. Chuyanov, "Suppression of plasma instabilities by the feedback method," Soviet Physics Uspekhi **20**, 736 (1977).

[28] A. D. Beklemishev, P. A. Bagryansky, M. S. Chaschin, and E. I. Soldatkina, "Vortex confinement of plasmas in symmetric mirror traps," Fusion Science

and Technology **57**, 351–360 (2010).
[29]K. H. Burrell, "Effects of $E \times B$ velocity shear and magnetic shear on turbulence and transport in magnetic confinement devices," Physics of Plasmas **4**, 1499–1518 (1997).
[30]T. A. Carter and J. E. Maggs, "Modifications of turbulence and turbulent transport associated with a bias-induced confinement transition in the large plasma device," Physics of Plasmas **16**, 012304 (2009).
[31]Y. Idomura, H. Urano, N. Aiba, and S. Tokuda, "Study of ion turbulent transport and profile formations using global gyrokinetic full-f vlasov simulation," Nuclear Fusion **49**, 065029 (2009).
[32]M. Barnes, D. Dickinson, W. Dorland, P. A. Hill, J. T. Parker, C. M. Roach, S. Biggs-Fox, N. Christen, R. Numata, J. Parisi, G. Wilkie, L. Anton, J. Ball, J. Baumgaertel, G. Colyer, M. Hardman, J. Hein, E. Highcock, G. Howes, A. Jackson, M. T. Kotschenreuther, J. Lee, H. Leggate, N. Mandell, A. Mauriya, T. Tatsuno, and F. Van Wyk, "GS2 v8.1.2," (2022).
[33]The GENE team, "Gyrokinetic electromagnetic numerical experiment," (2023).
[34]J. Candy, E. Belli, and R. Bravenec, "A high-accuracy eulerian gyrokinetic solver for collisional plasmas," Journal of Computational Physics **324**, 73–93 (2016).
[35]S. E. Parker, J. J. Kohut, Y. Chen, Z. Lin, F. L. Hinton, and W. W. Lee, "Fine-scale zonal flow suppression of electron temperature gradient turbulence," AIP Conference Proceedings **871**, 193–203 (2006), https://aip.scitation.org/doi/pdf/10.1063/1.2404551.
[36]S. Ku, R. Hager, C. Chang, J. Kwon, and S. Parker, "A new hybrid-lagrangian numerical scheme for gyrokinetic simulation of tokamak edge plasma," Journal of Computational Physics **315**, 467–475 (2016).
[37]J. A. Krommes, "The gyrokinetic description of microturbulence in magnetized plasmas," Annual Review of Fluid Mechanics **44**, 175–201 (2012), https://doi.org/10.1146/annurev-fluid-120710-101223.
[38]The Gkeyll team, "The Gkeyll 2.0 Code: Documentation Home," (2023).
[39]E. Shi, *Gyrokinetic continuum simulation of turbulence in open-field-line plasmas*, Ph.D. thesis, Princeton University (2017).
[40]D. Michels, A. Stegmeir, P. Ulbl, D. Jarema, and F. Jenko, "GENE-X: A full-f gyrokinetic turbulence code based on the flux-coordinate independent approach," Computer Physics Communications **264**, 107986 (2021).
[41]M. R. Dorr, P. Colella, M. A. Dorf, D. Ghosh, J. A. Hittinger, and P. O. Schwartz, "High-order discretization of a gyrokinetic Vlasov model in edge plasma geometry," Journal of Computational Physics **373**, 605–630 (2018).
[42]E. Peterson, "The Pleiades code," (2020).
[43]R. White, A. Hassam, and A. Brizard, "Centrifugal particle confinement in mirror geometry," Physics of Plasmas **25**, 012514 (2018).
[44]N. R. Mandell, A. Hakim, G. W. Hammett, and M. Francisquez, "Electromagnetic full-f gyrokinetics in the tokamak edge with discontinuous Galerkin methods," Journal of Plasma Physics **86** (2020), 10.1017/S0022377820000070.
[45]M. Francisquez, T. Bernard, N. Mandell, G. Hammett, and A. Hakim, "Conservative discontinuous Galerkin scheme of a gyro-averaged Dougherty collision operator," Nuclear Fusion **60**, 096021 (2020).
[46]M. Francisquez, J. Juno, A. Hakim, G. W. Hammett, and D. R. Ernst, "Improved multispecies Dougherty collisions," Journal of Plasma Physics **88**, 905880303 (2022).
[47]H. Sugama, "Gyrokinetic field theory," Physics of Plasmas **7**, 466–480 (2000).
[48]A. J. Brizard and T. S. Hahm, "Foundations of nonlinear gyrokinetic theory," Rev. Mod. Phys. **79**, 421–468 (2007).
[49]P. Tamain, H. Bufferand, G. Ciraolo, C. Colin, D. Galassi, P. Ghendrih, F. Schwander, and E. Serre, "The TOKAM3X code for edge turbulence fluid simulations of tokamak plasmas in versatile magnetic geometries," Journal of Computational Physics **321**, 606–623 (2016).
[50]S. Peluchetti, "SciLua," (2022).
[51]S. Robertson, "A reduced set of gyrofluid equations for plasma flow in a diverging magnetic field," Physics of Plasmas **23**, 043513 (2016).
[52]J. D. Huba, *NRL Plasma Formulary, Supported by The Office of Naval Research* (Naval Research Laboratory, Washington, DC, 2013) pp. 1–71.
[53]The velocity drag and diffusion parts of the Dougherty operator do have a collision frequency independent of velocity, in contrasts with the LRO's $1/v^3$ dependence for equivalent terms.
[54]E. L. Shi, G. W. Hammett, T. Stoltzfus-Dueck, and A. Hakim, "Gyrokinetic continuum simulation of turbulence in a straight open-field-line plasma," Journal of Plasma Physics **83**, 905830304 (2017).
[55]R. M. Kulsrud, "MHD description of plasma," (North-Holland Publishing Company, 1983) Chap. 1.4.
[56]O. V. Batishchev, S. I. Krasheninnikov, P. J. Catto, A. A. Batishcheva, D. J. Sigmar, X. Q. Xu, J. A. Byers, T. D. Rognlien, R. H. Cohen, M. M. Shoucri, and I. P. Shkarofskii, "Kinetic effects in tokamak scrape-off layer plasmas," Physics of Plasmas **4**, 1672–1680 (1997), https://pubs.aip.org/aip/pop/article-pdf/4/5/1672/12655860/1672_1_online.pdf.
[57]A. Chankin, D. Coster, and G. Meisl, "Development and benchmarking of a new kinetic code for plasma periphery (kipp)," Contributions to Plasma Physics **52**, 500–504 (2012), https://onlinelibrary.wiley.com/doi/pdf/10.1002/ctpp.201210039.
[58]E. L. Shi, A. H. Hakim, and G. W. Hammett, "A gyrokinetic one-dimensional scrape-off layer model of an edge-localized mode heat pulse," Physics of Plasmas **22**, 022504 (2015).
[59]D. Ryutov, "Axial electron heat loss from mirror devices revisited," Fusion Science and Technology **47**, 148–154 (2005), https://doi.org/10.13182/FST05-A627.
[60]D. Jarema, H. Bungartz, T. Görler, F. Jenko, T. Neckel, and D. Told, "Block-structured grids for Eulerian gyrokinetic simulations," Computer Physics Communications **198**, 105–117 (2016).
[61]W. Taitano, L. Chacón, and A. Simakov, "An adaptive, conservative 0D-2V multispecies Rosenbluth–Fokker–Planck solver for arbitrarily disparate mass and temperature regimes," Journal of Computational Physics **318**, 391–420 (2016).
[62]W. Lee, "Gyrokinetic particle simulation model," Journal of Computational Physics **72**, 243–269 (1987).
[63]G. R. Werner, T. G. Jenkins, A. M. Chap, and J. R. Cary, "Speeding up simulations by slowing down particles: Speed-limited particle-in-cell simulation," Physics of Plasmas **25**, 123512 (2018).
[64]T. K. Fowler, "Mirror theory," in *Fusion*, edited by E. Teller (Academic Press, 1981) pp. 291–355.
[65]For example, consider a μ grid that has the same grid spacing as a uniform grid at small μ but transitions to a relative spacing grid at higher μ, of the form $\Delta\mu_j = \max(r\mu_{j-1/2}, \Delta\mu_0)$. This relative grid with a 12% relative grid spacing ($r = 0.12$) and just 36 cells can span the same range as a uniform grid with 192 cells.
[66]N. R. Mandell, *Magnetic Fluctuations in Gyrokinetic Simulations of Tokamak Scrape-Off Layer Turbulence*, Ph.D. thesis, Princeton University (2021).
[67]M. Francisquez, M. H. Rosen, N. R. Mandell, A. Hakim, C. B. Forest, and G. W. Hammett, "Dataset from: Towards continuum gyrokinetic study of high-field mirrors. ," Zenodo (2023), Identifier: 10.5281/zenodo.8125802.
[68]D. D. Ryutov, "Open-ended traps," Soviet Physics Uspekhi **31**, 300 (1988).

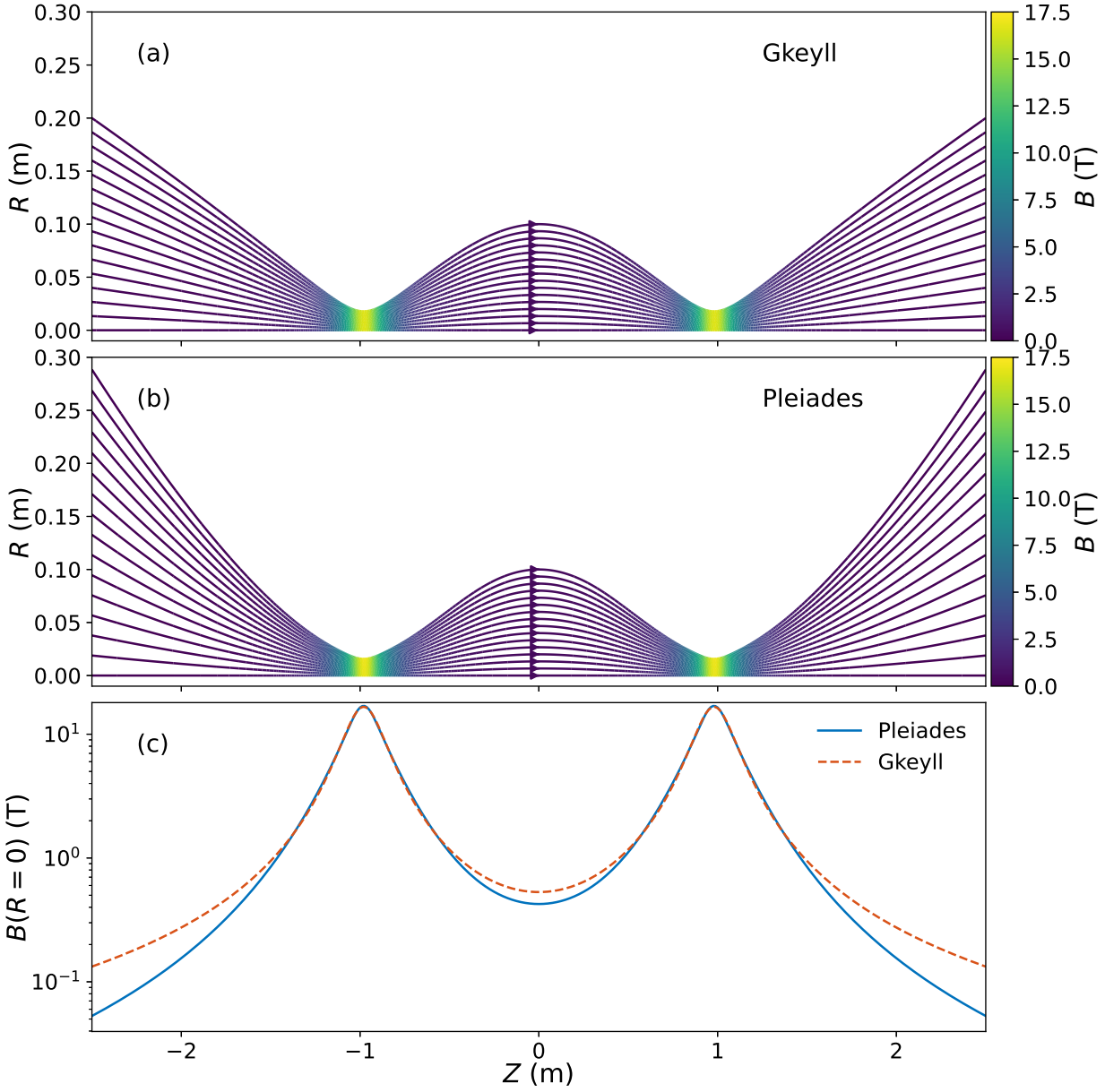
(a)
Gkeyll
(b)
Pleiades
(c)
Pleiades
Gkeyll
R (m)
B (T)
B(R = 0) (T)
Z (m)
0.30
0.25
0.20
0.15
0.10
0.05
0.00
17.5
15.0
12.5
10.0
7.5
5.0
2.5
0.0
10^1
10^0
10^−1
−2
−1
0
1
2

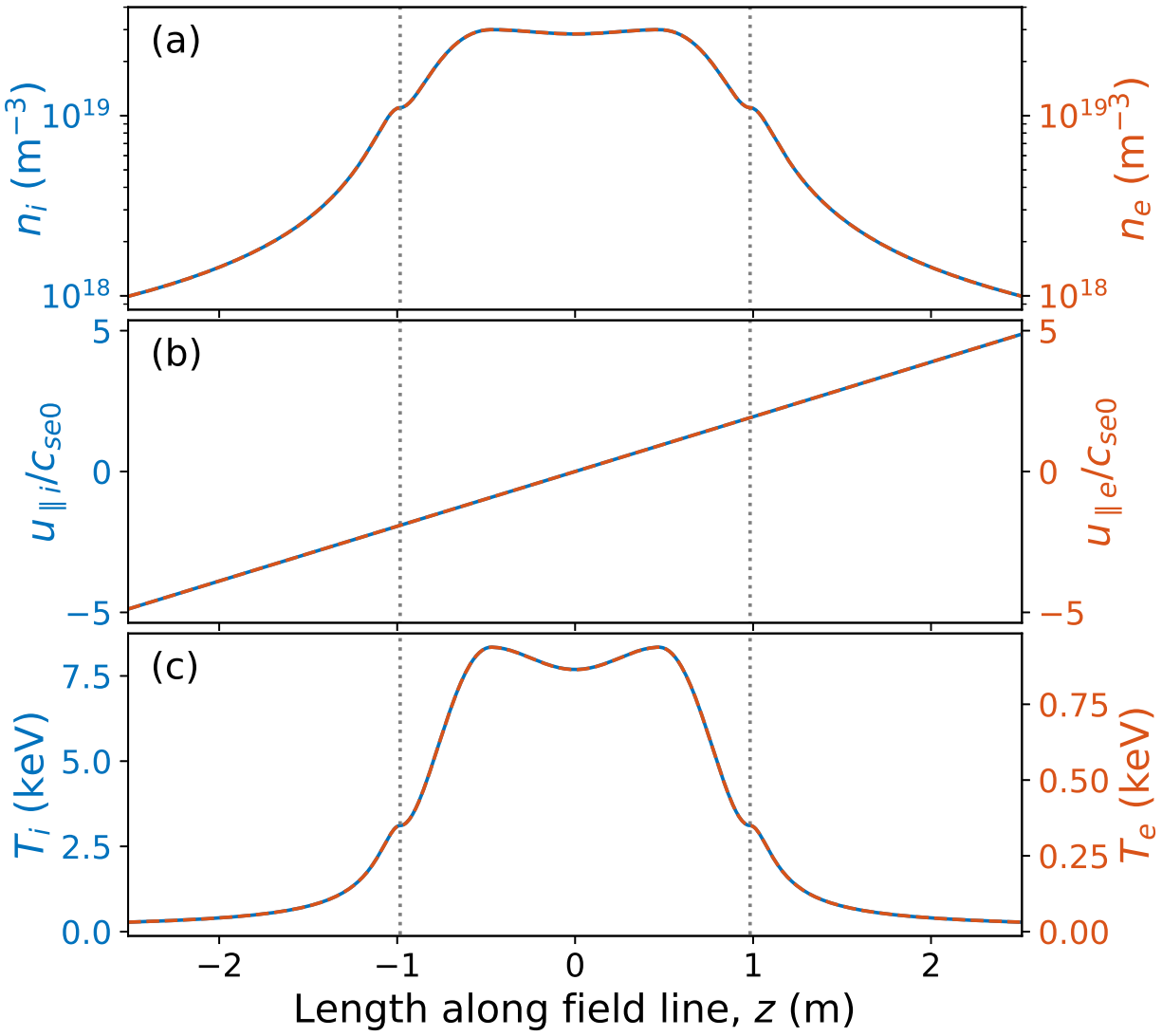
(a)
(b)
(c)
n_i (m^{-3})
n_e (m^{-3})
10^{19}
10^{18}
$u_{\parallel i}/c_{se0}$
$u_{\parallel e}/c_{se0}$
5
0
−5
T_i (keV)
T_e (keV)
7.5
5.0
2.5
0.0
0.75
0.50
0.25
0.00
−2
−1
0
1
2
Length along field line, z (m)

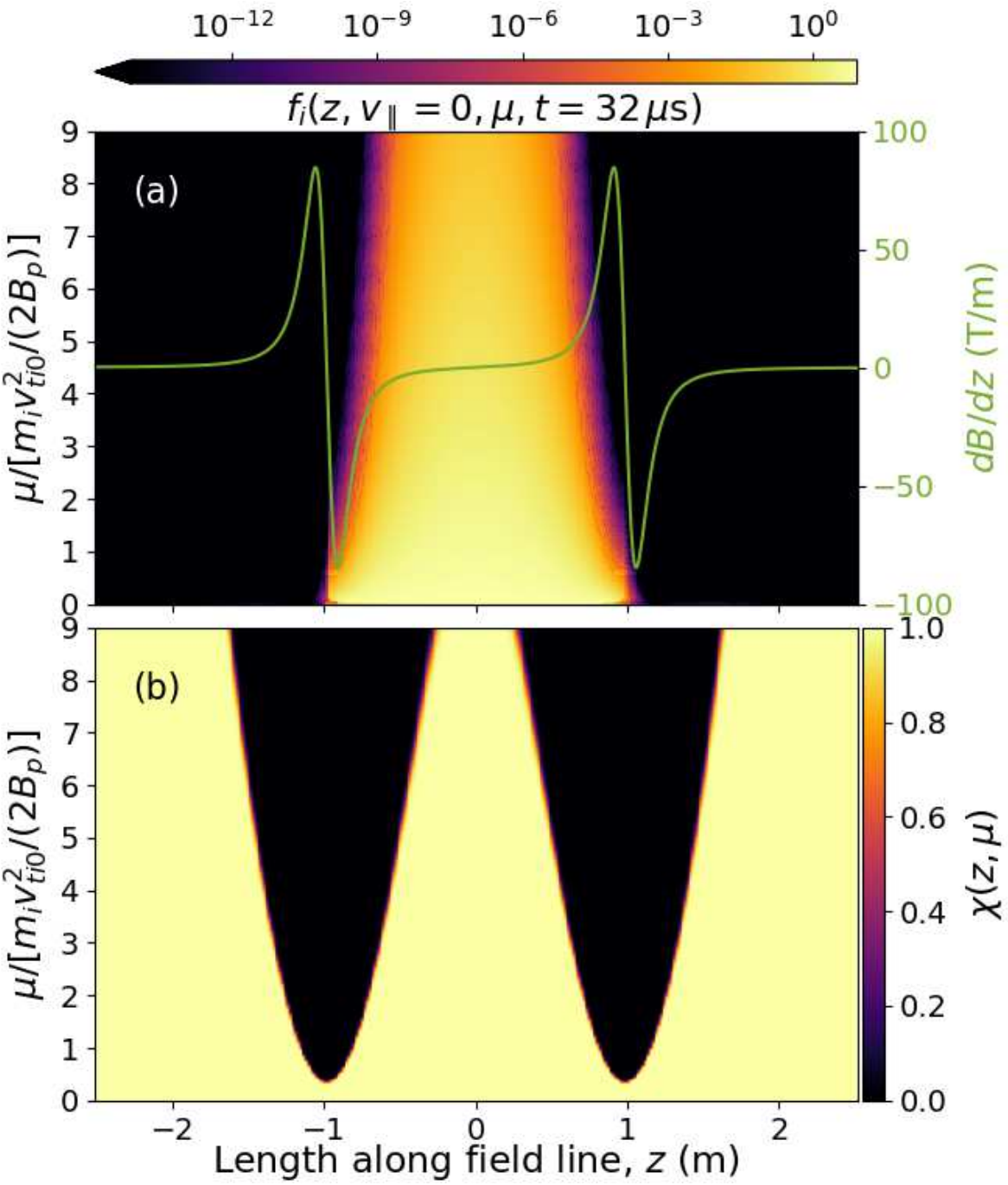
10^{-12}
10^{-9}
10^{-6}
10^{-3}
10^{0}
$f_i(z, v_\parallel = 0, \mu, t = 32\,\mu\mathrm{s})$
(a)
$\mu/[m_i v_{ti0}^2/(2B_p)]$
100
50
0
−50
−100
dB/dz (T/m)
(b)
$\mu/[m_i v_{ti0}^2/(2B_p)]$
1.0
0.8
0.6
0.4
0.2
0.0
$\chi(z, \mu)$
−2
−1
0
1
2
Length along field line, z (m)

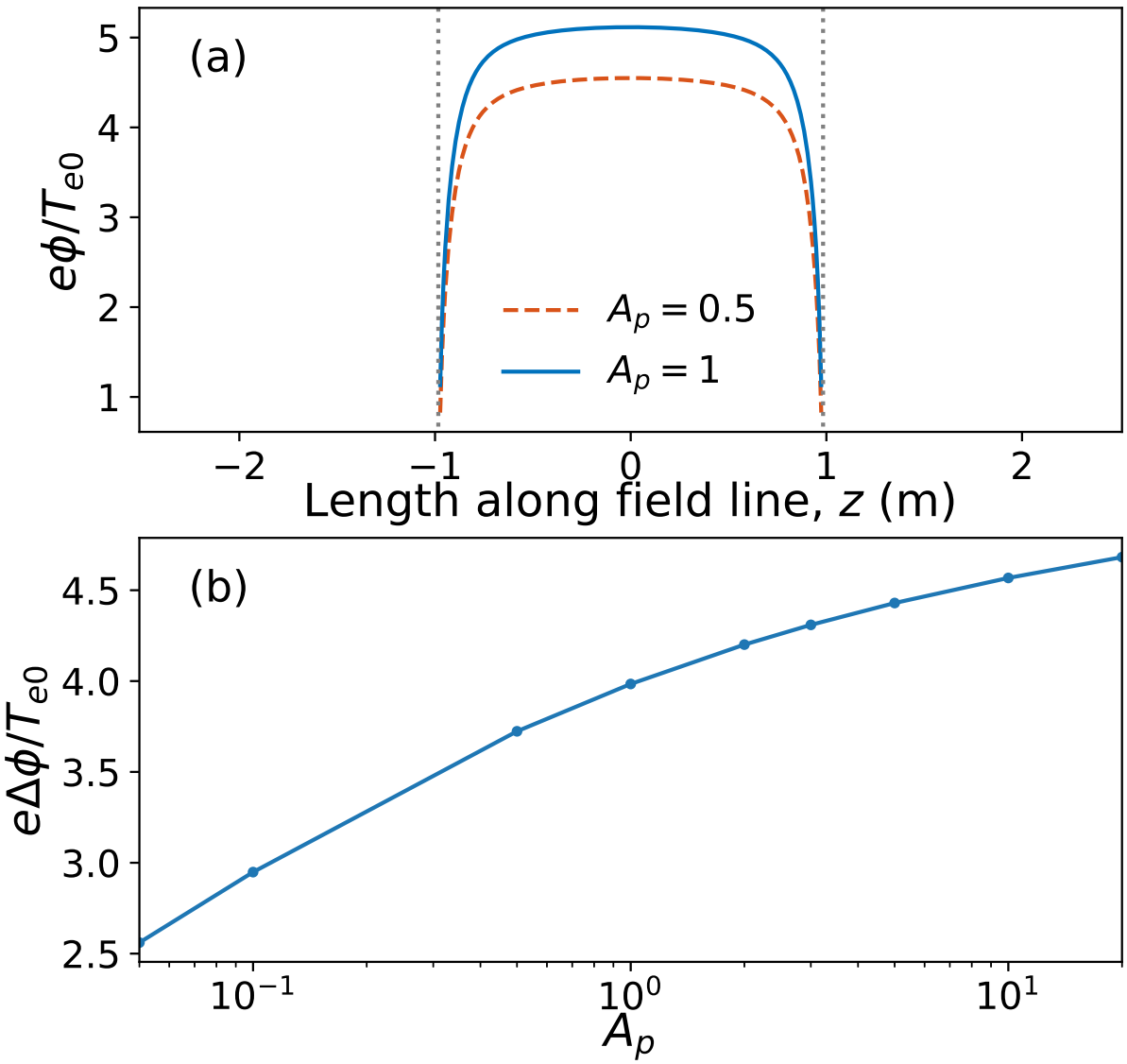
(a)
$e\phi/T_{e0}$
5
4
3
2
1
$A_p = 0.5$
$A_p = 1$
−2
−1
0
1
2
Length along field line, z (m)
(b)
$e\Delta\phi/T_{e0}$
4.5
4.0
3.5
3.0
2.5
10^{-1}
10^{0}
10^{1}
A_p

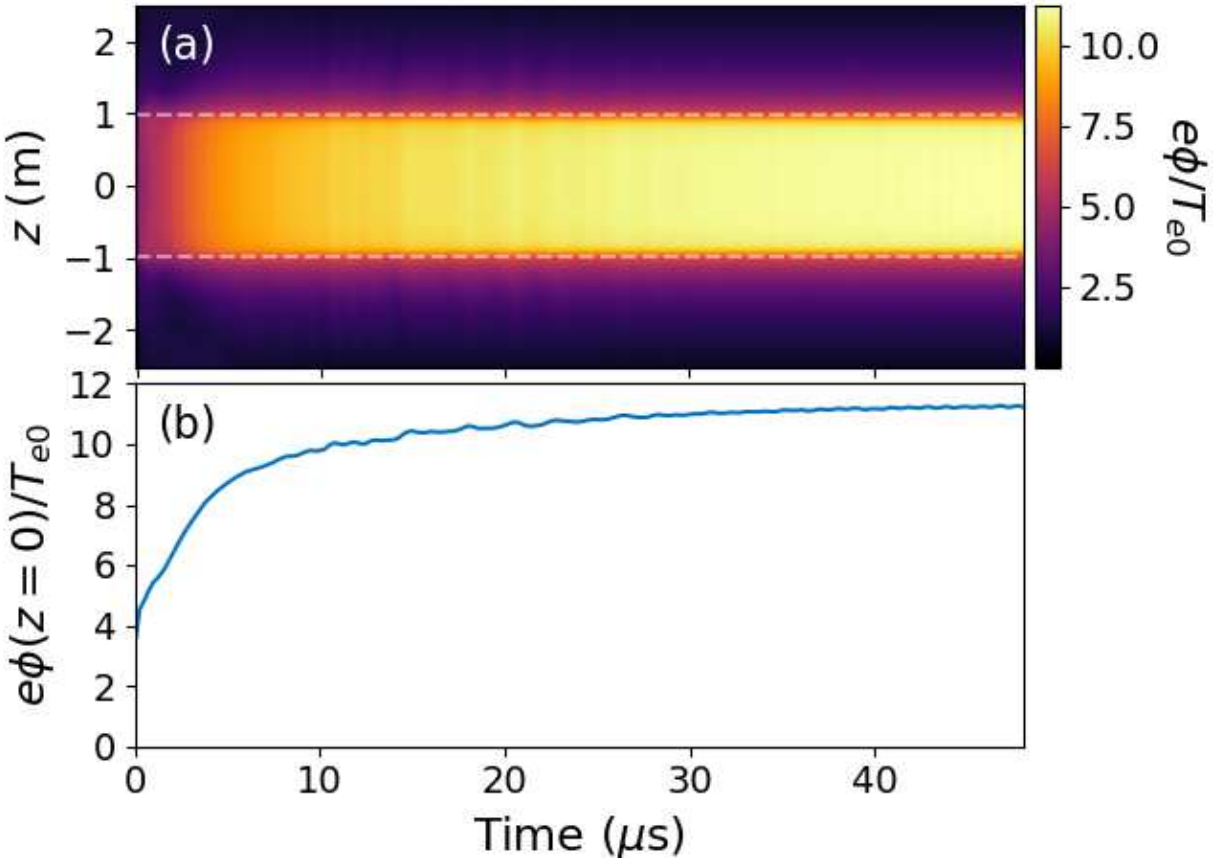
(a)
(b)
z (m)
2
1
0
−1
−2
eϕ/T_e0
10.0
7.5
5.0
2.5
eϕ(z = 0)/T_e0
12
10
8
6
4
2
0
0
10
20
30
40
Time (μs)

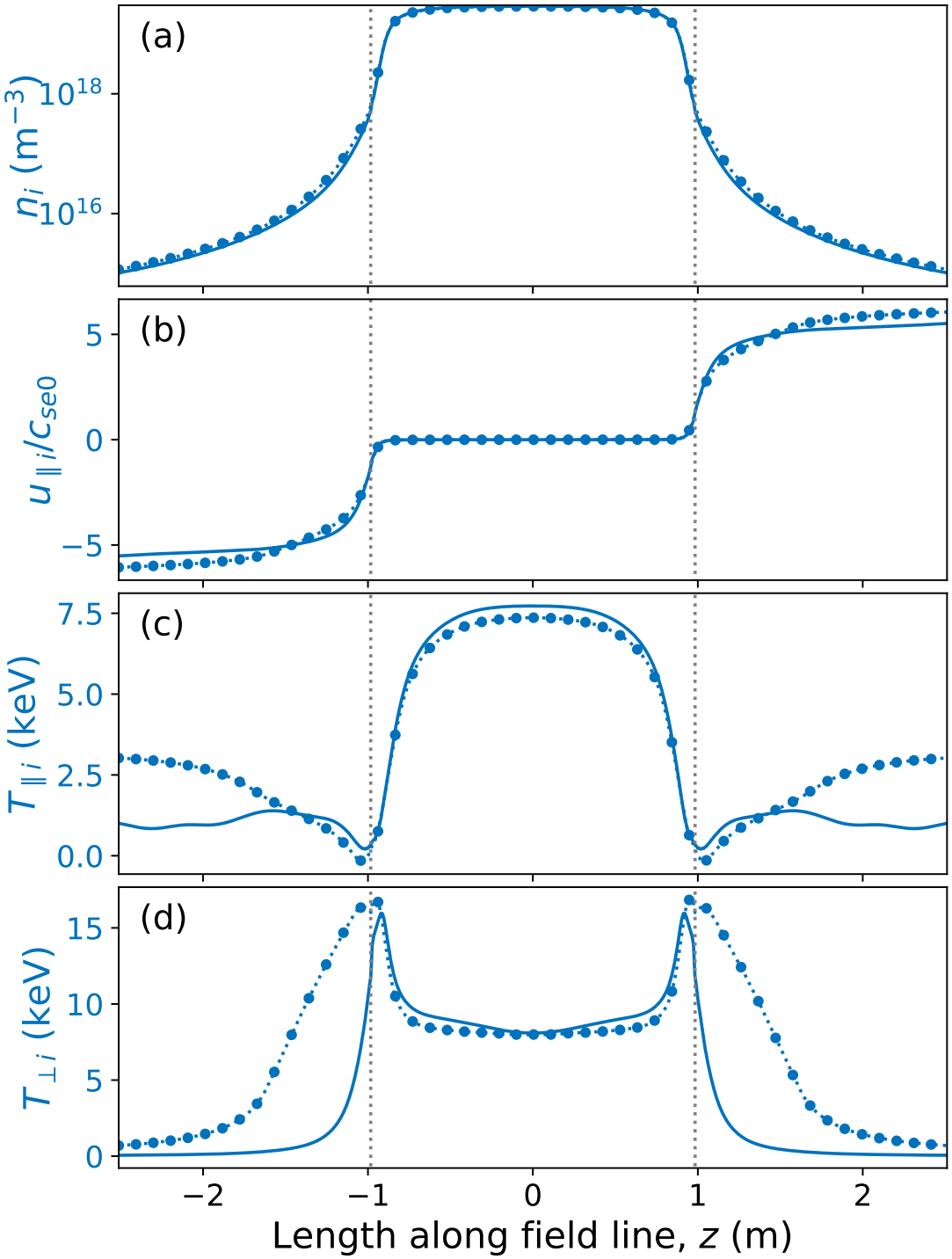
(a)
n_i (m^{-3})
10^{18}
10^{16}
(b)
$u_{\parallel i}/c_{se0}$
5
0
−5
(c)
$T_{\parallel i}$ (keV)
7.5
5.0
2.5
0.0
(d)
$T_{\perp i}$ (keV)
15
10
5
0
−2
−1
0
1
2
Length along field line, z (m)

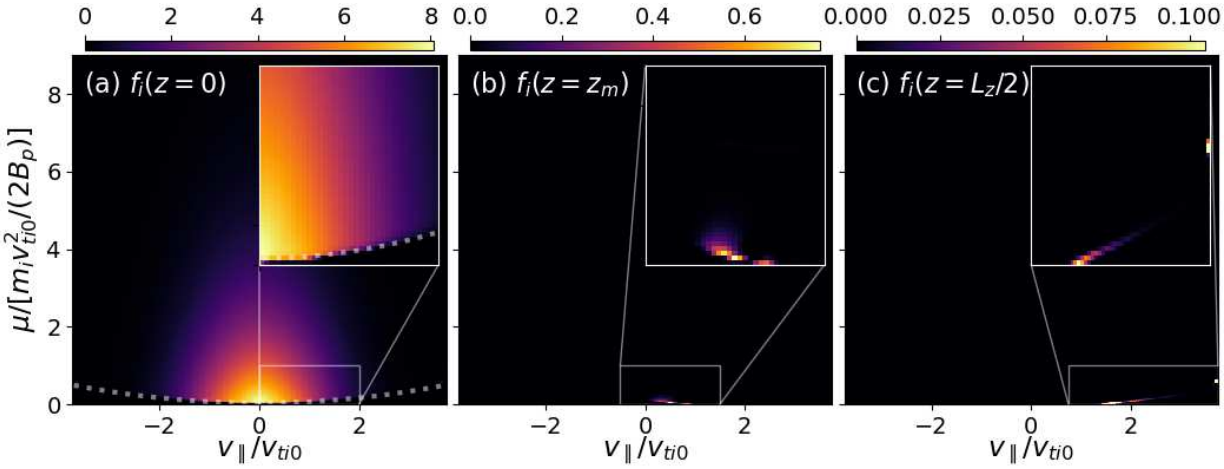
0 2 4 6 8
0.0 0.2 0.4 0.6
0.000 0.025 0.050 0.075 0.100
(a) $f_i(z=0)$
(b) $f_i(z=z_m)$
(c) $f_i(z=L_z/2)$
$\mu/[m_i v_{ti0}^2/(2B_p)]$
$v_\parallel/v_{ti0}$
$v_\parallel/v_{ti0}$
$v_\parallel/v_{ti0}$

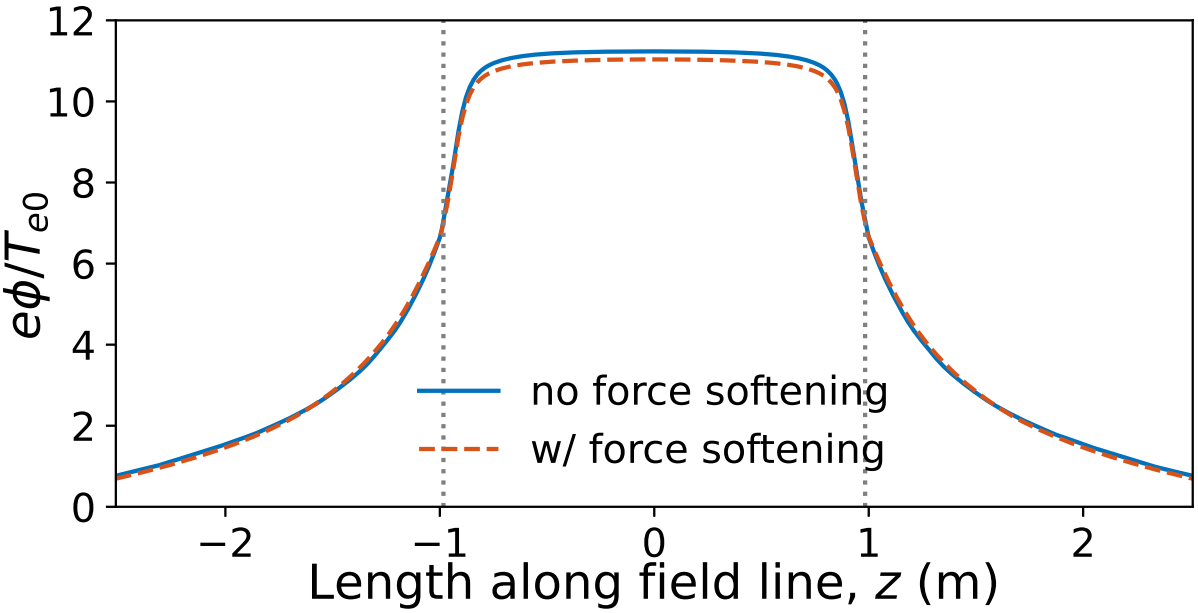
12
10
8
6
4
2
0
$e\phi/T_{e0}$
−2
−1
0
1
2
Length along field line, z (m)
no force softening
w/ force softening

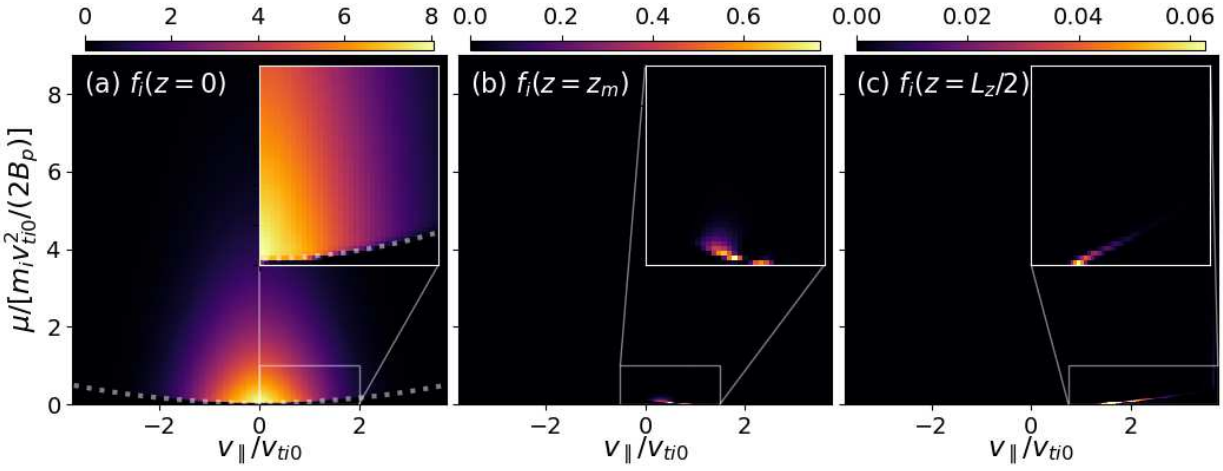
0 2 4 6 8
0.0 0.2 0.4 0.6
0.00 0.02 0.04 0.06
(a) $f_i(z=0)$
(b) $f_i(z=z_m)$
(c) $f_i(z=L_z/2)$
$\mu/[m_i v_{ti0}^2/(2B_p)]$
$v_\parallel/v_{ti0}$
$v_\parallel/v_{ti0}$
$v_\parallel/v_{ti0}$

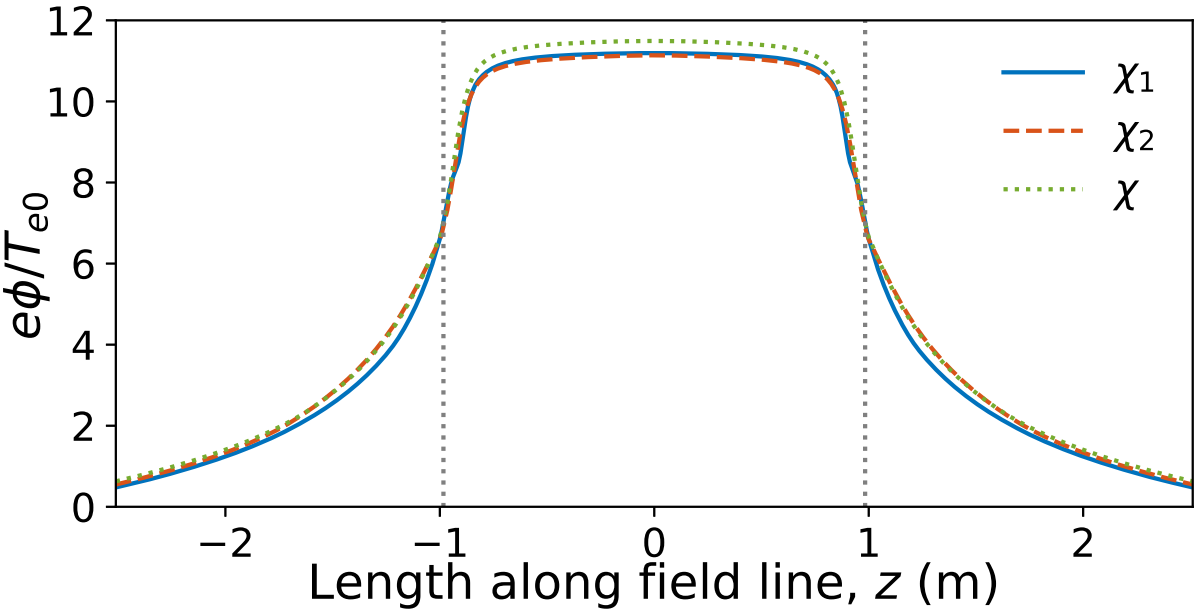
12
10
8
6
4
2
0
$e\phi/T_{e0}$
−2
−1
0
1
2
Length along field line, z (m)
χ_1
χ_2
χ

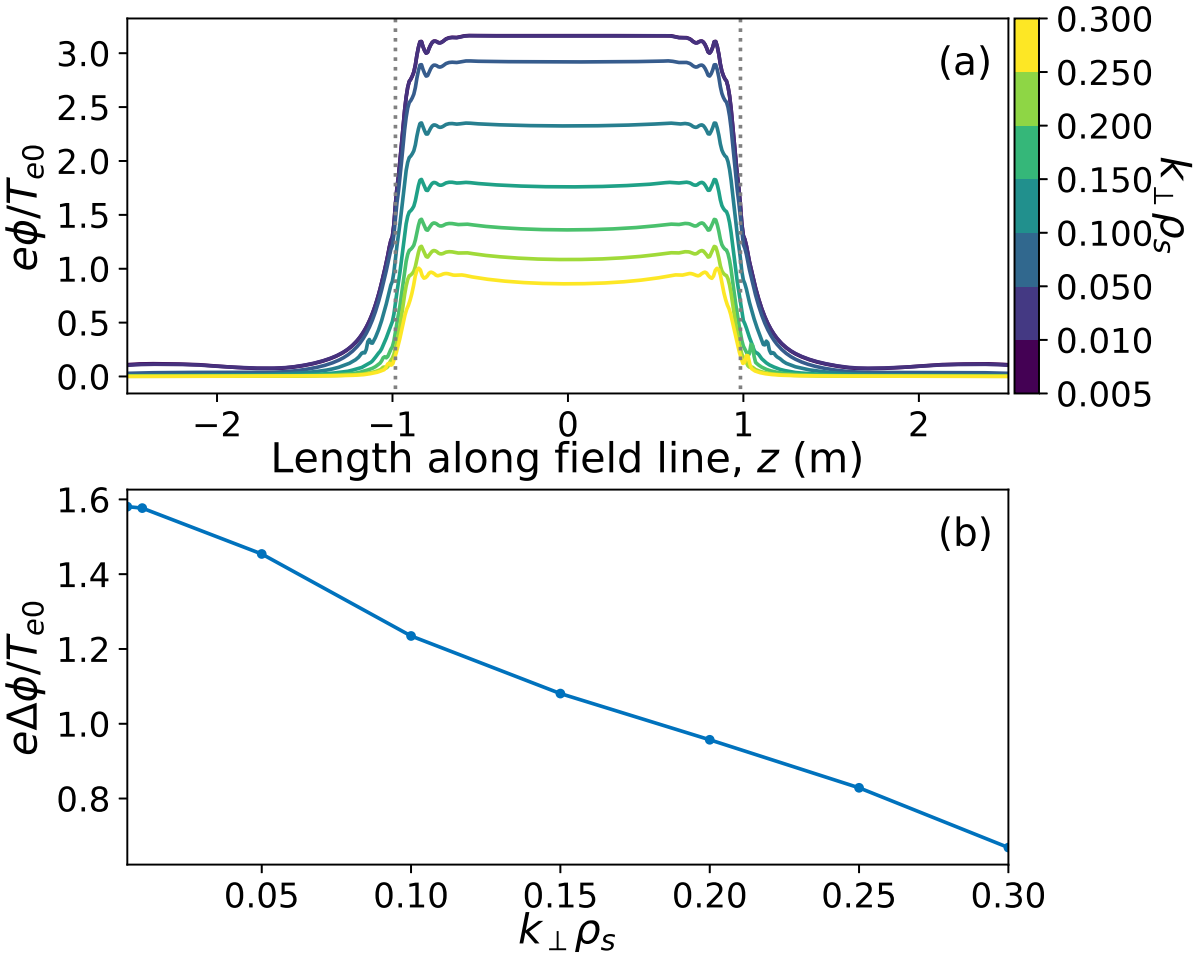
(a)
$e\phi/T_{e0}$
3.0
2.5
2.0
1.5
1.0
0.5
0.0
−2
−1
0
1
2
Length along field line, z (m)
0.300
0.250
0.200
0.150
0.100
0.050
0.010
0.005
$k_\perp \rho_s$
(b)
$e\Delta\phi/T_{e0}$
1.6
1.4
1.2
1.0
0.8
0.05
0.10
0.15
0.20
0.25
0.30
$k_\perp \rho_s$

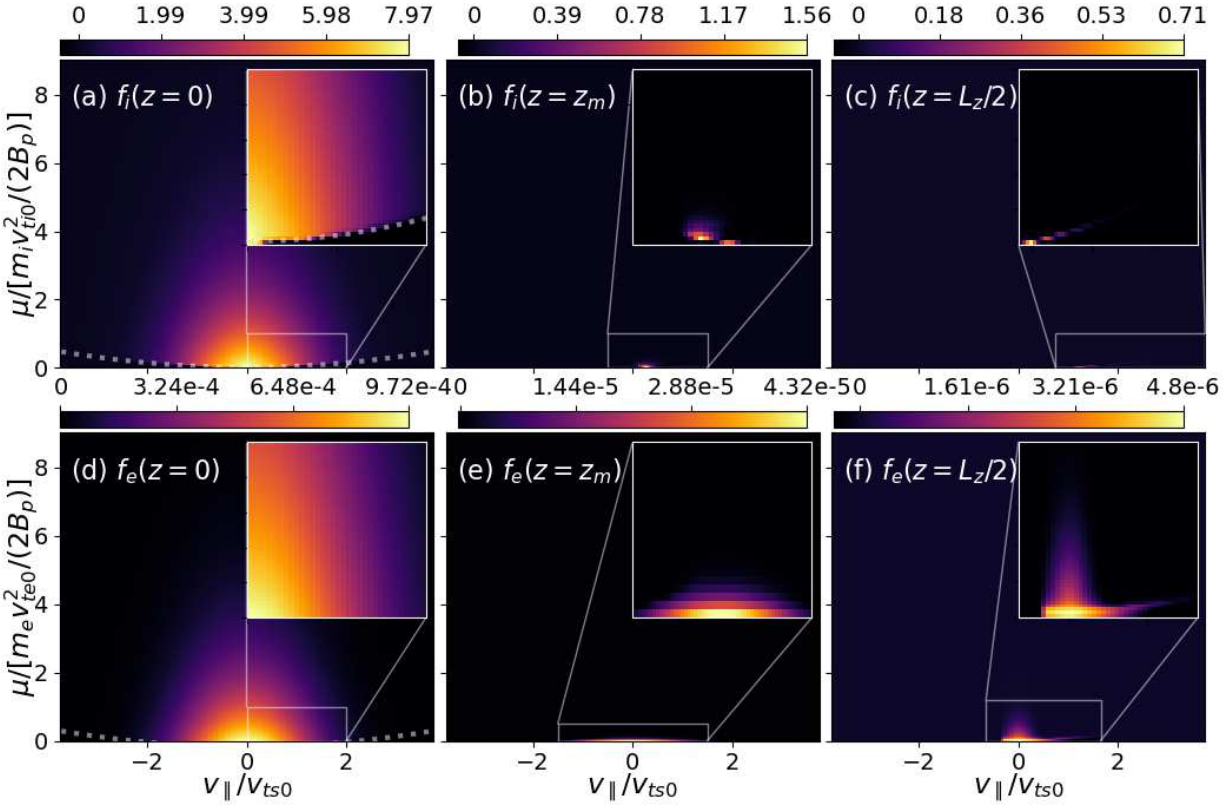
0 1.99 3.99 5.98 7.97
0 0.39 0.78 1.17 1.56
0 0.18 0.36 0.53 0.71
(a) $f_i(z=0)$
(b) $f_i(z=z_m)$
(c) $f_i(z=L_z/2)$
$\mu/[m_i v_{ti0}^2/(2B_p)]$
0 3.24e-4 6.48e-4 9.72e-40
1.44e-5 2.88e-5 4.32e-50
1.61e-6 3.21e-6 4.8e-6
(d) $f_e(z=0)$
(e) $f_e(z=z_m)$
(f) $f_e(z=L_z/2)$
$\mu/[m_e v_{te0}^2/(2B_p)]$
$v_\parallel/v_{ts0}$

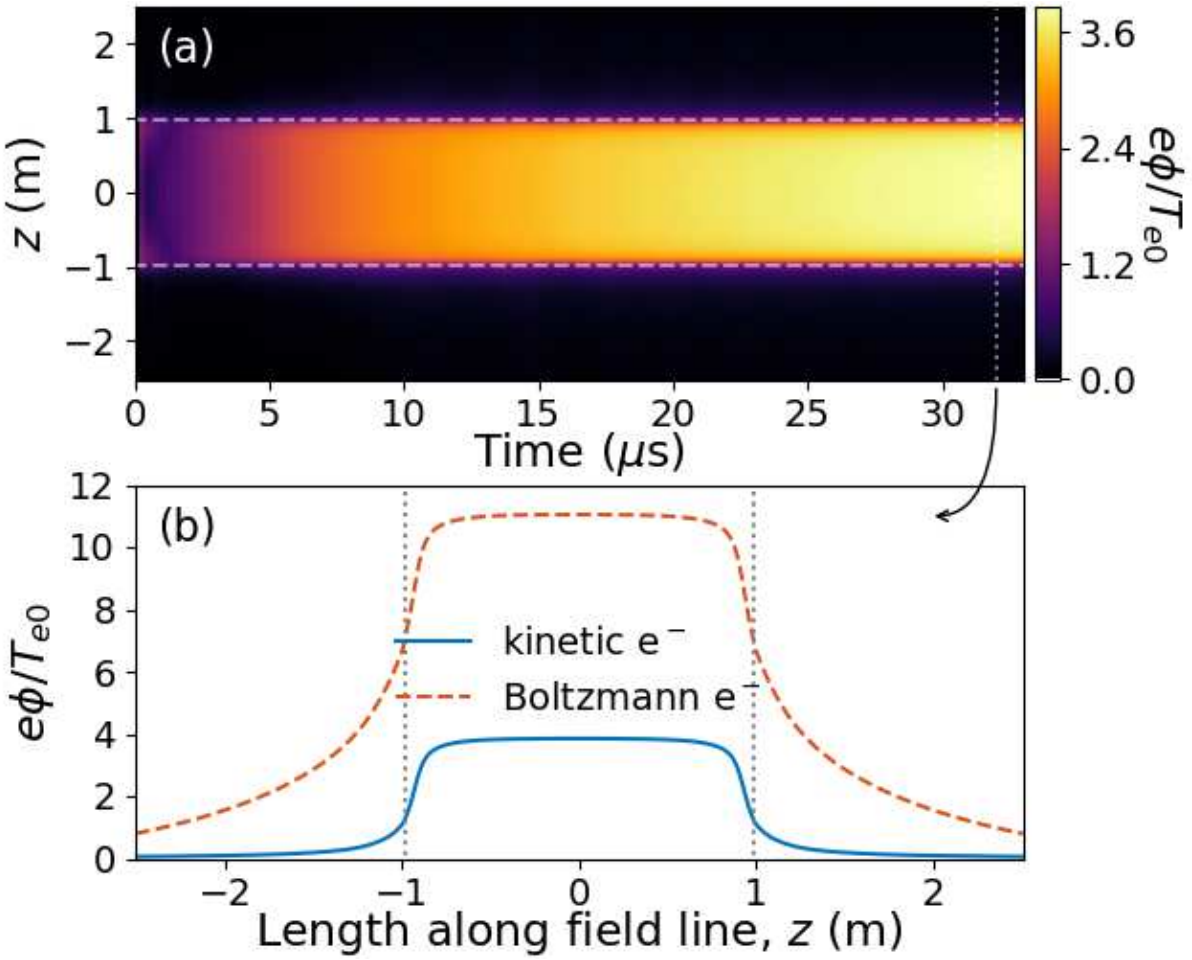
(a)
z (m)
Time (μs)
eϕ/T_e0
3.6
2.4
1.2
0.0
(b)
kinetic e⁻
Boltzmann e⁻
eϕ/T_e0
Length along field line, z (m)

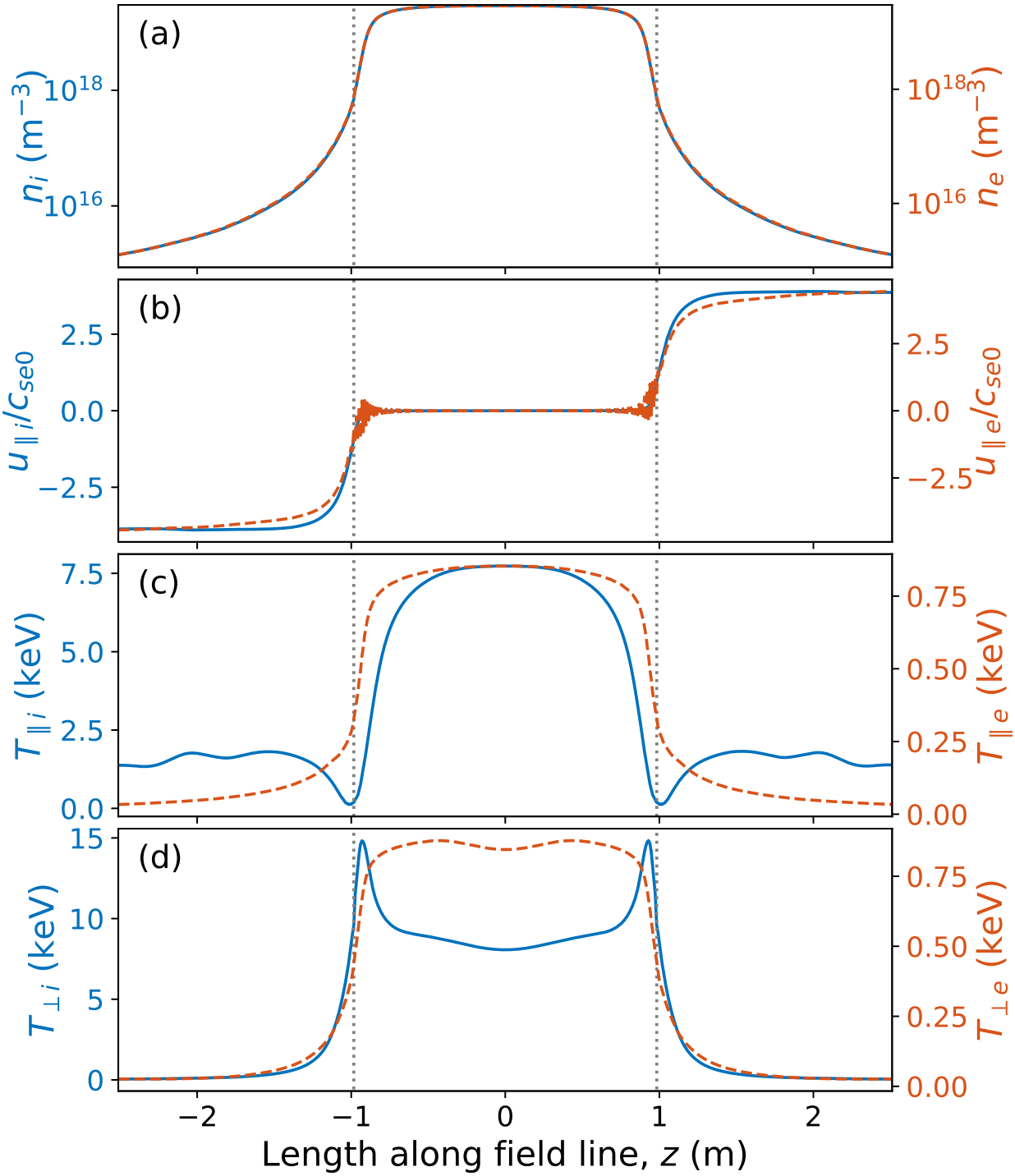
(a)
n_i (m^{-3})
10^{18}
10^{16}
n_e (m^{-3})
(b)
$u_{\parallel i}/c_{se0}$
2.5
0.0
−2.5
$u_{\parallel e}/c_{se0}$
(c)
$T_{\parallel i}$ (keV)
7.5
5.0
2.5
0.0
$T_{\parallel e}$ (keV)
0.75
0.50
0.25
0.00
(d)
$T_{\perp i}$ (keV)
15
10
5
0
$T_{\perp e}$ (keV)
−2
−1
0
1
2
Length along field line, z (m)

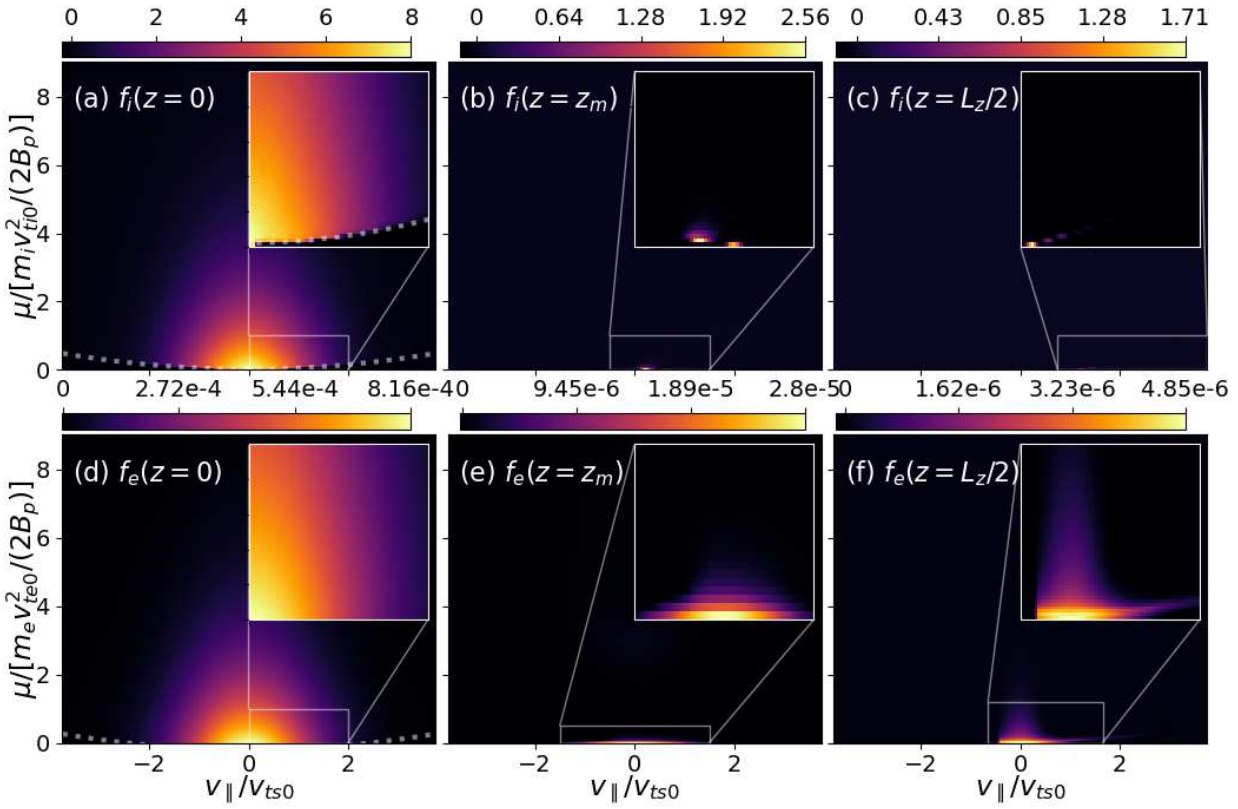
(a) $f_i(z=0)$
(b) $f_i(z=z_m)$
(c) $f_i(z=L_z/2)$
(d) $f_e(z=0)$
(e) $f_e(z=z_m)$
(f) $f_e(z=L_z/2)$
$\mu/[m_i v_{ti0}^2/(2B_p)]$
$\mu/[m_e v_{te0}^2/(2B_p)]$
$v_\parallel/v_{ts0}$
0 2 4 6 8
0 0.64 1.28 1.92 2.56
0 0.43 0.85 1.28 1.71
0 2.72e-4 5.44e-4 8.16e-4
0 9.45e-6 1.89e-5 2.8e-5
0 1.62e-6 3.23e-6 4.85e-6

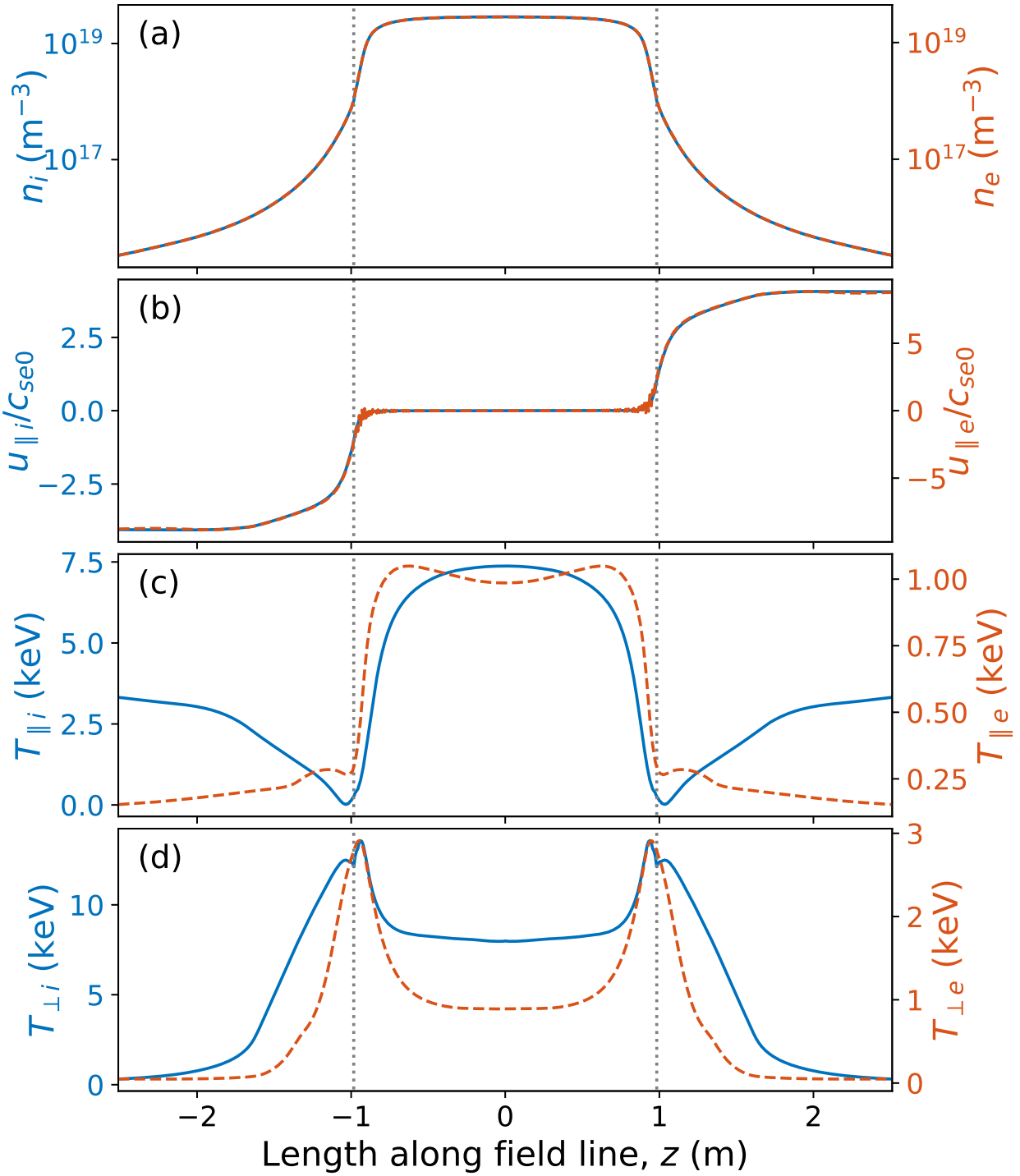
(a)
(b)
(c)
(d)
10^{19}
10^{17}
n_i (m^{-3})
n_e (m^{-3})
2.5
0.0
−2.5
5
0
−5
$u_{\parallel i}/c_{se0}$
$u_{\parallel e}/c_{se0}$
7.5
5.0
2.5
0.0
1.00
0.75
0.50
0.25
$T_{\parallel i}$ (keV)
$T_{\parallel e}$ (keV)
10
5
0
3
2
1
0
$T_{\perp i}$ (keV)
$T_{\perp e}$ (keV)
−2
−1
0
1
2
Length along field line, z (m)

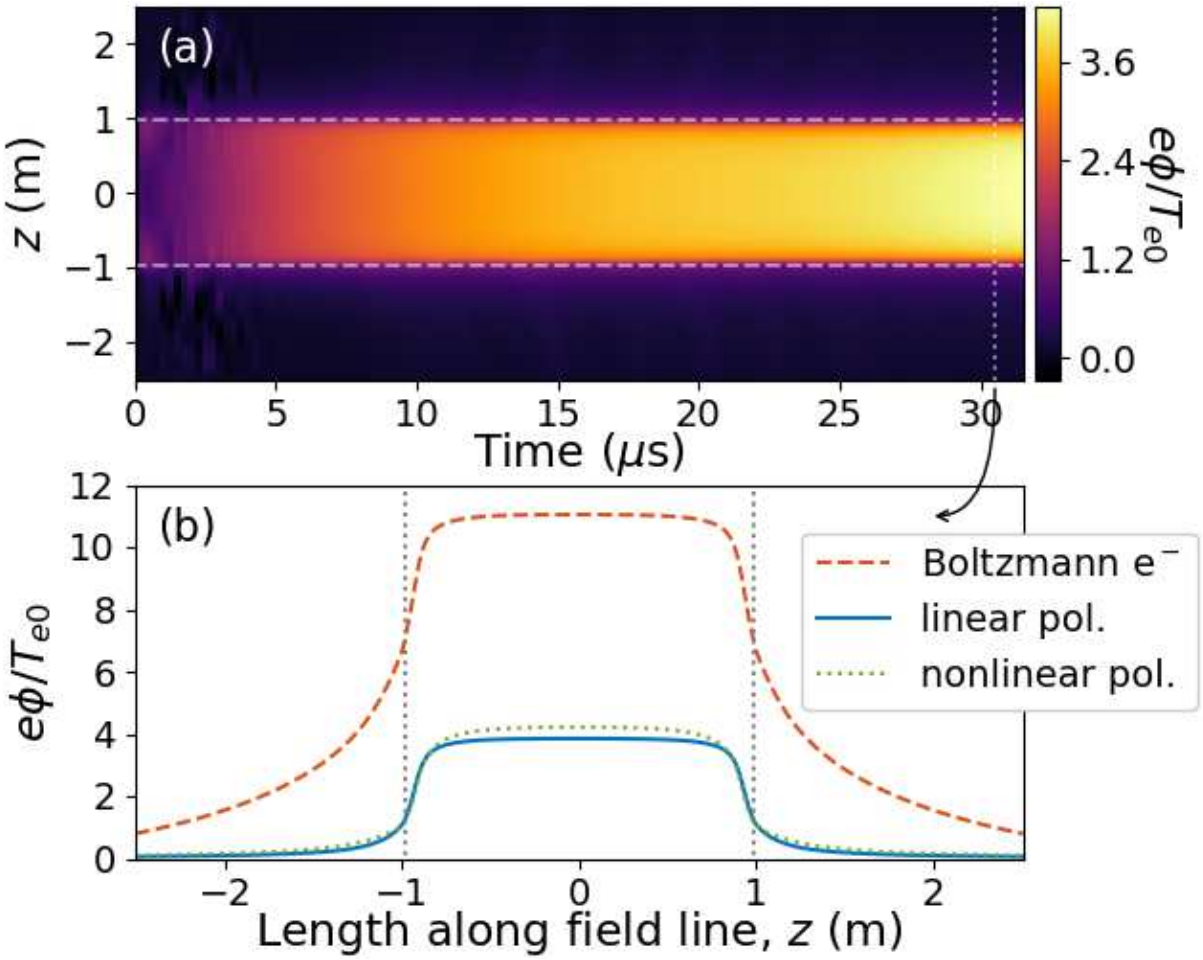
(a)
z (m)
Time (μs)
eϕ/T_e0
(b)
eϕ/T_e0
Length along field line, z (m)
Boltzmann e⁻
linear pol.
nonlinear pol.

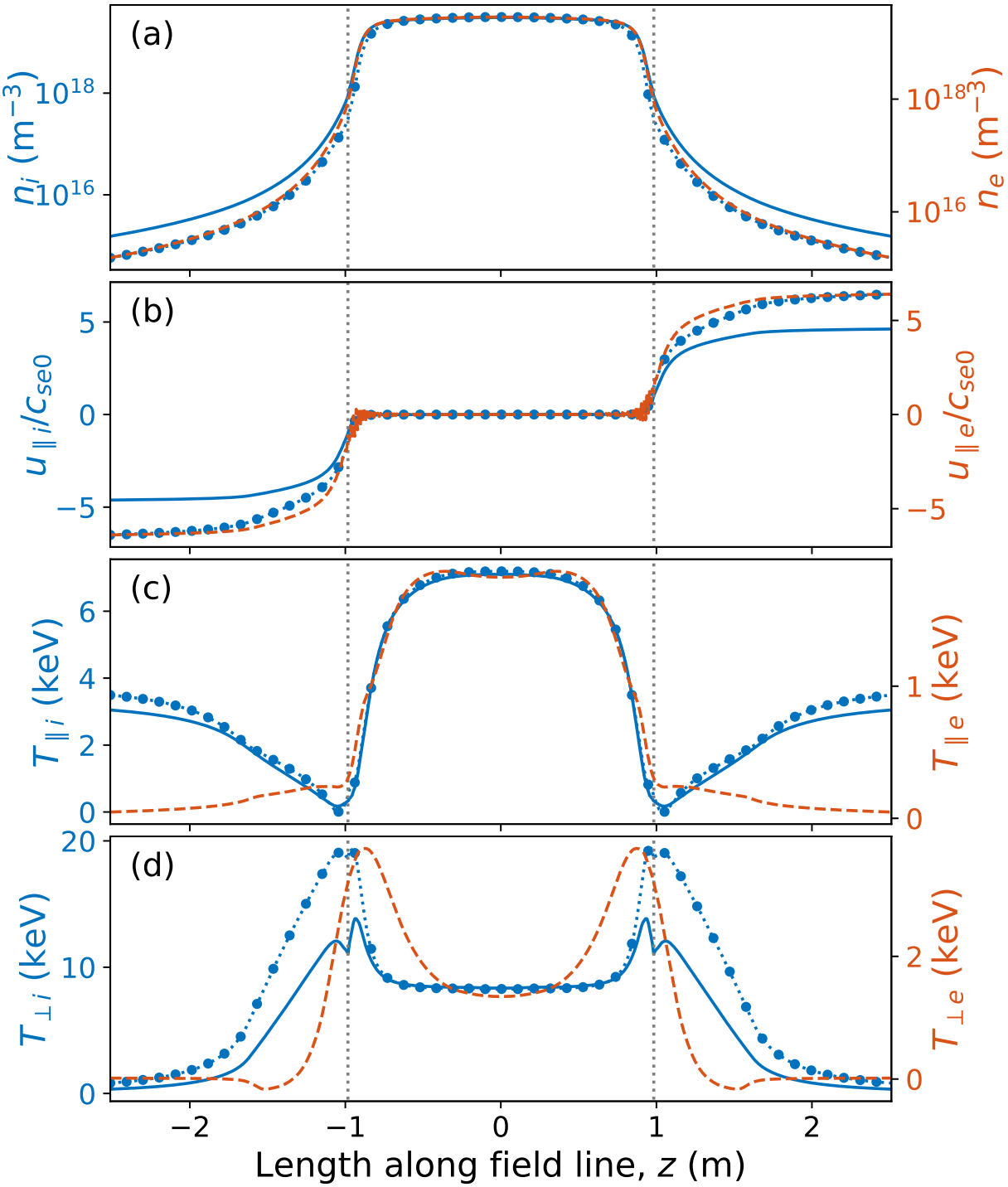
(a)
n_i (m^{-3})
10^{18}
10^{16}
n_e (m^{-3})
(b)
$u_{\parallel i}/c_{se0}$
$u_{\parallel e}/c_{se0}$
(c)
$T_{\parallel i}$ (keV)
$T_{\parallel e}$ (keV)
(d)
$T_{\perp i}$ (keV)
$T_{\perp e}$ (keV)
Length along field line, z (m)

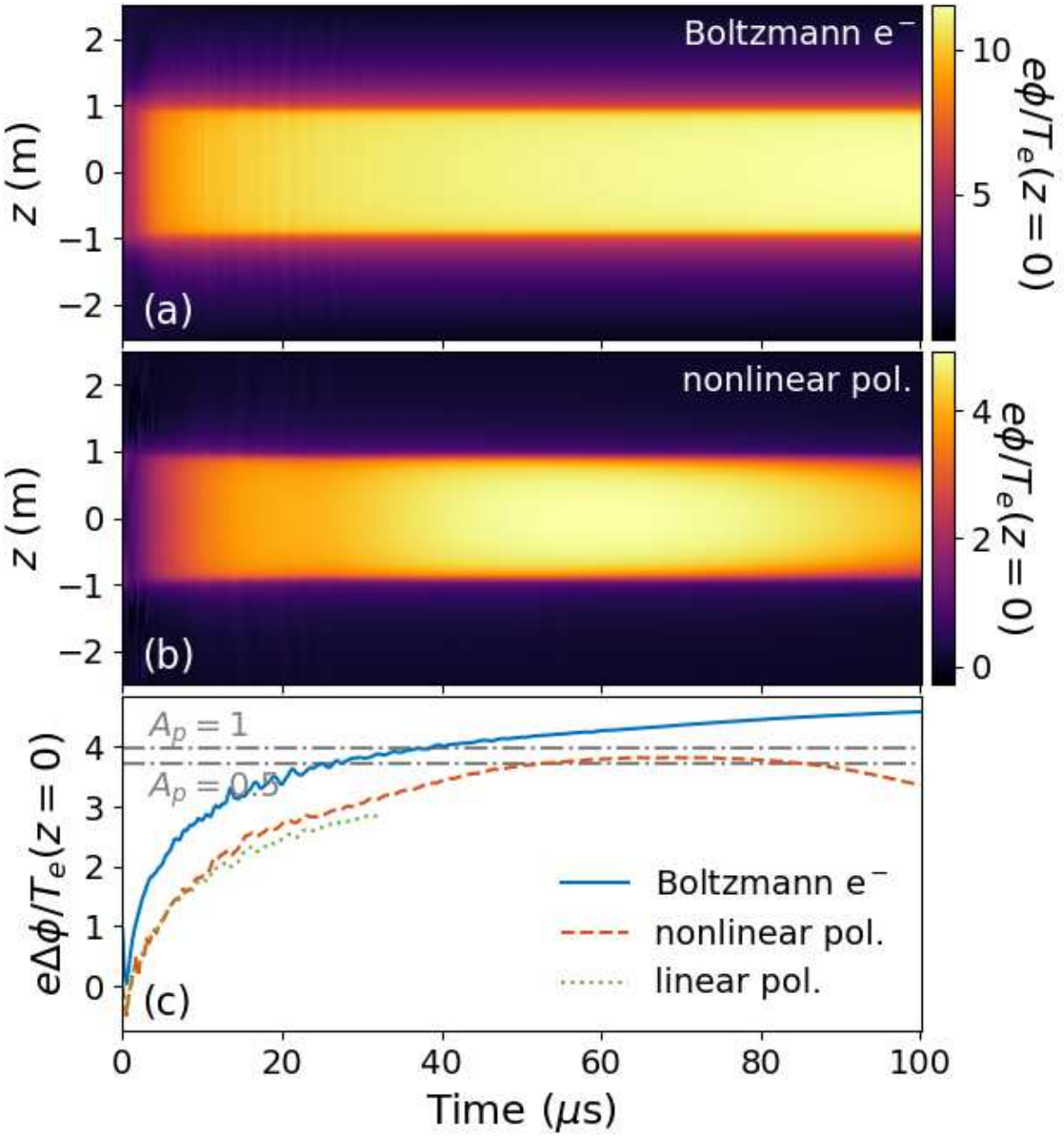
Boltzmann e⁻
(a)
z (m)
eϕ/T_e(z = 0)
nonlinear pol.
(b)
z (m)
eϕ/T_e(z = 0)
A_p = 1
A_p = 0.5
eΔϕ/T_e(z = 0)
Boltzmann e⁻
nonlinear pol.
linear pol.
(c)
Time (μs)

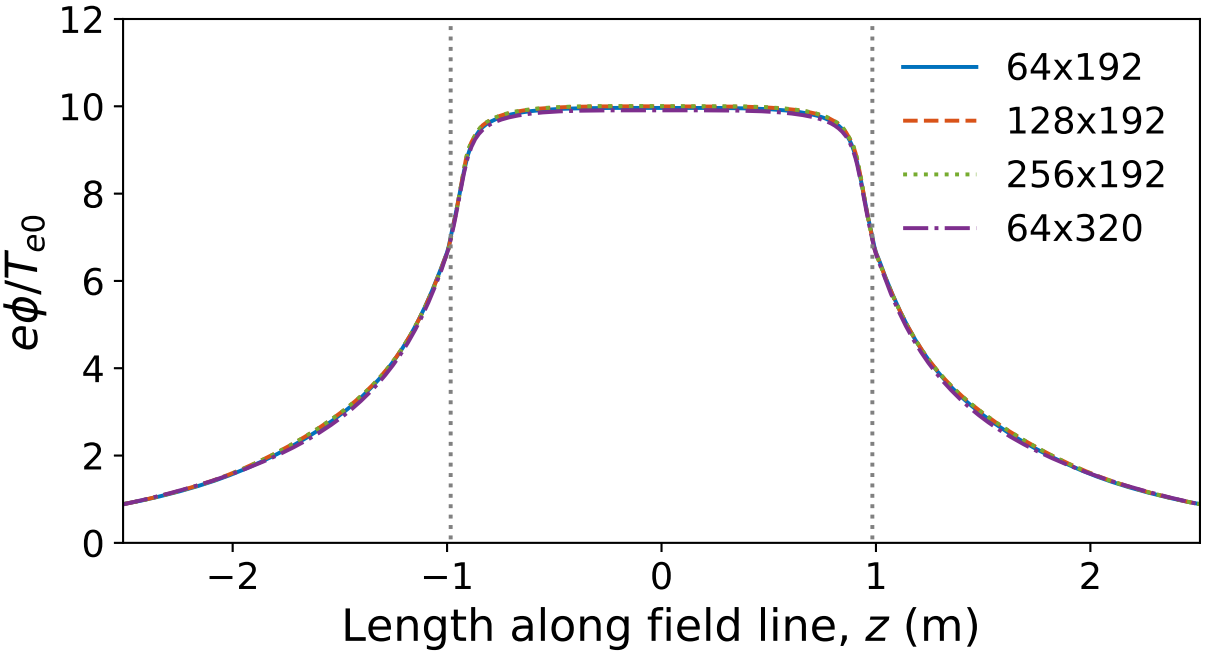
12
10
8
6
4
2
0
−2
−1
0
1
2
$e\phi/T_{e0}$
Length along field line, z (m)
64x192
128x192
256x192
64x320

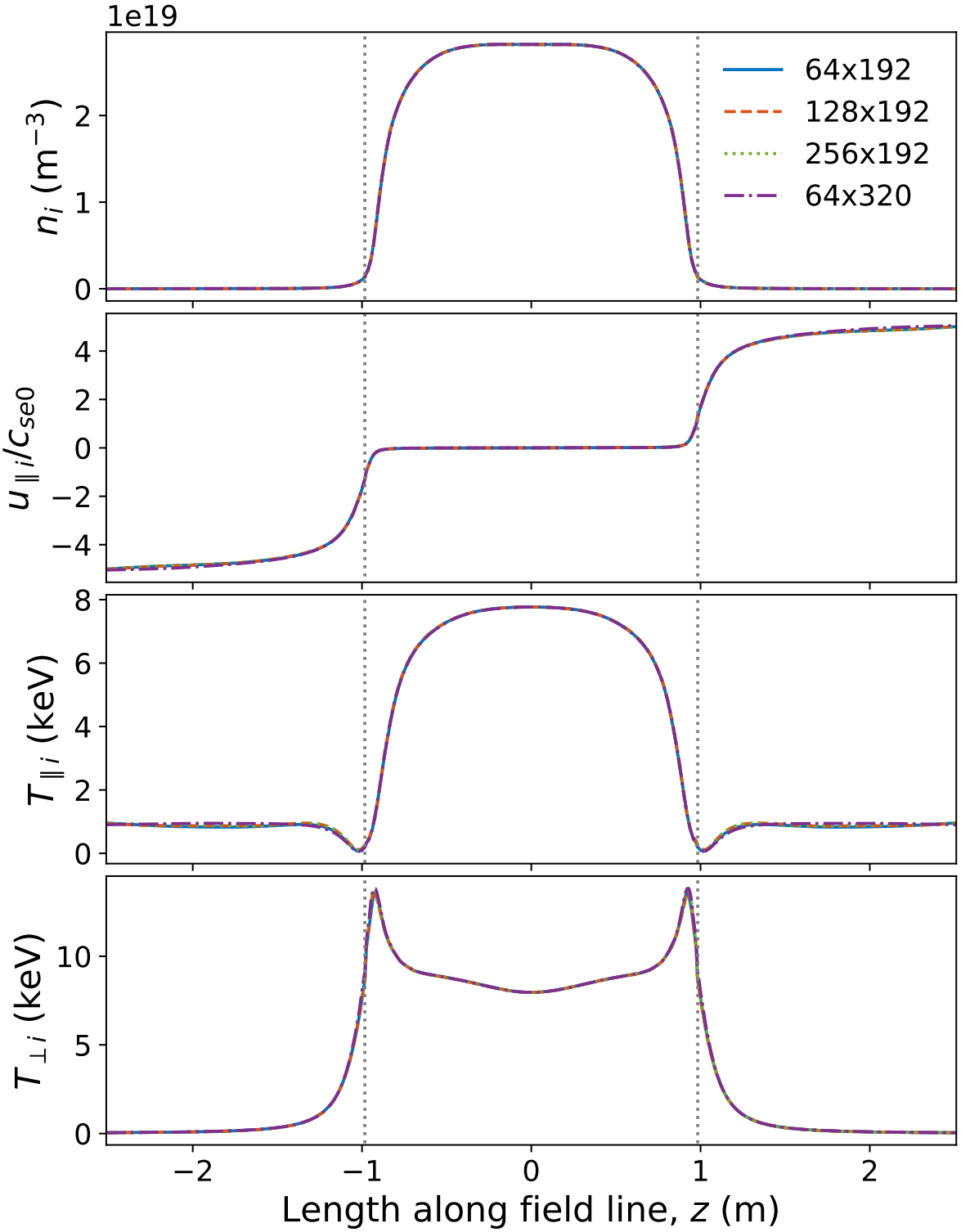
1e19
n_i (m^{-3})
$u_{\parallel i}/c_{se0}$
$T_{\parallel i}$ (keV)
$T_{\perp i}$ (keV)
64x192
128x192
256x192
64x320
Length along field line, z (m)

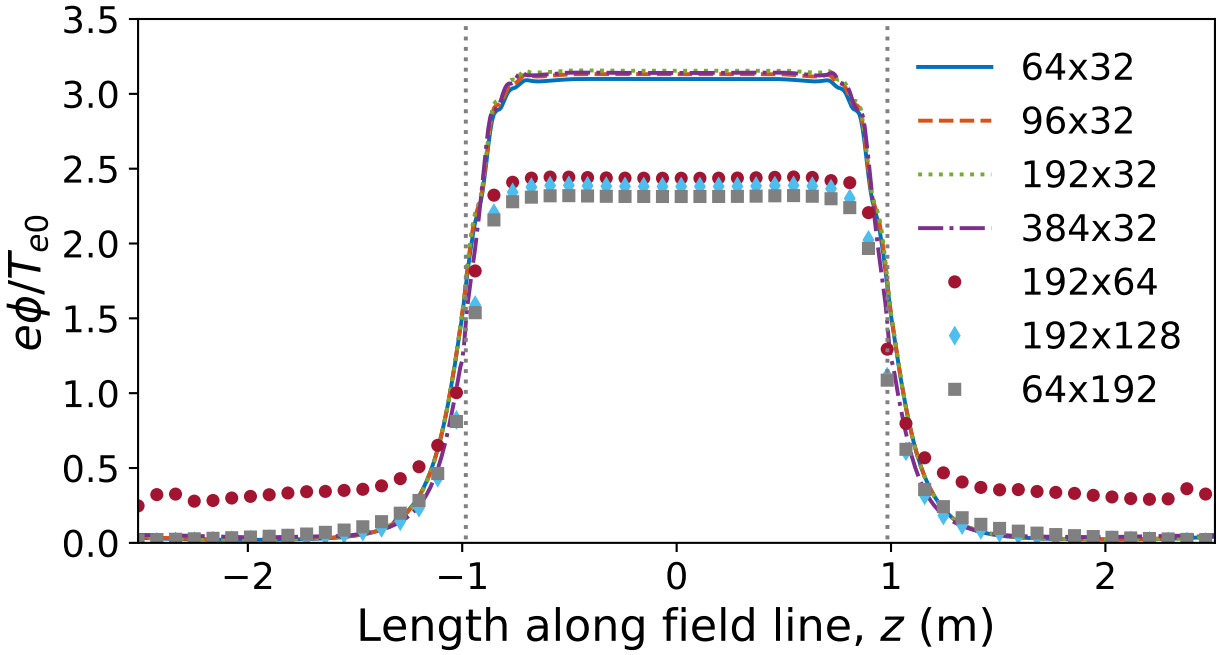
3.5
3.0
2.5
2.0
1.5
1.0
0.5
0.0
$e\phi/T_{e0}$
−2
−1
0
1
2
Length along field line, z (m)
64x32
96x32
192x32
384x32
192x64
192x128
64x192

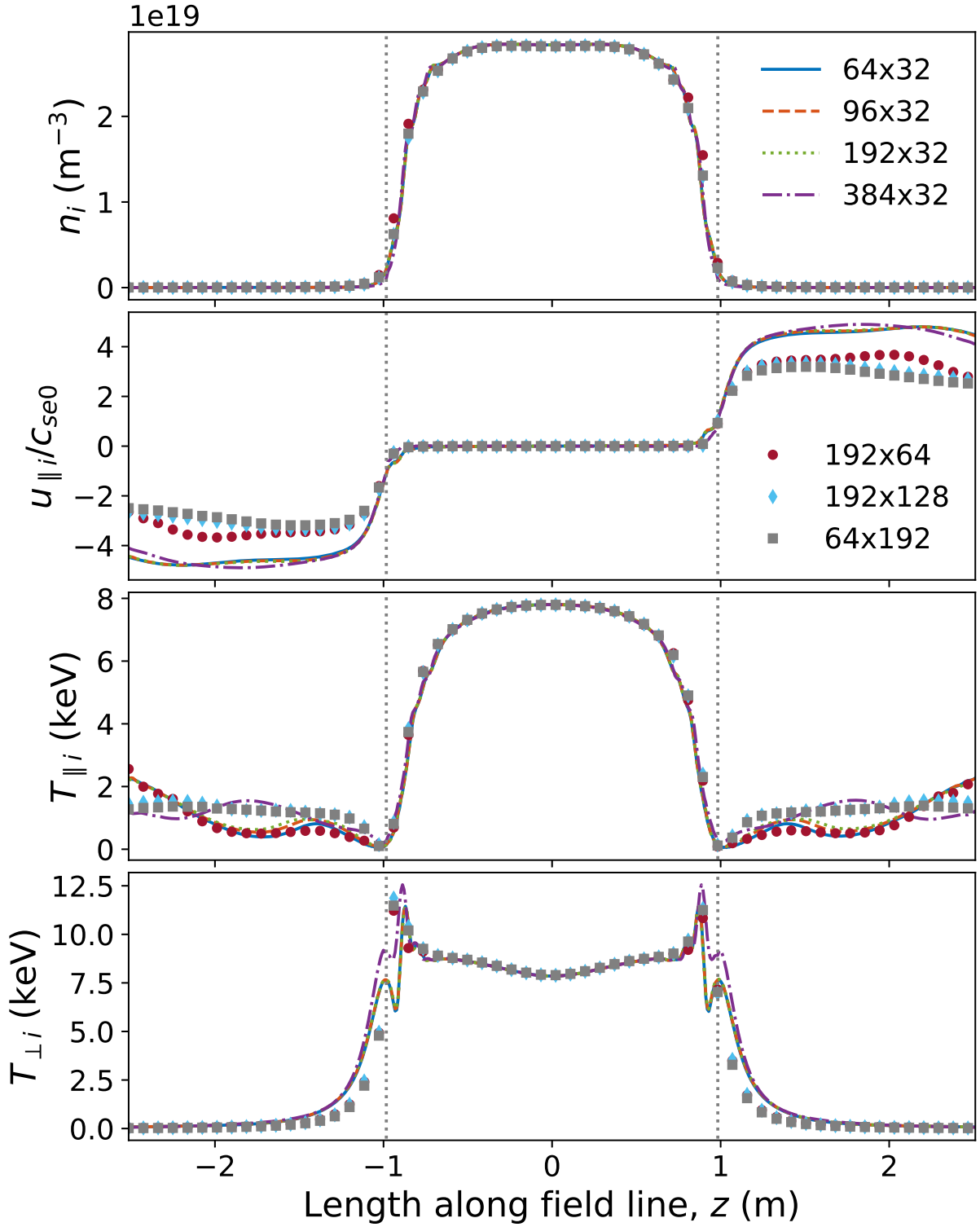
1e19
n_i (m^{-3})
64x32
96x32
192x32
384x32
$u_{\parallel i}/c_{se0}$
192x64
192x128
64x192
$T_{\parallel i}$ (keV)
$T_{\perp i}$ (keV)
Length along field line, z (m)

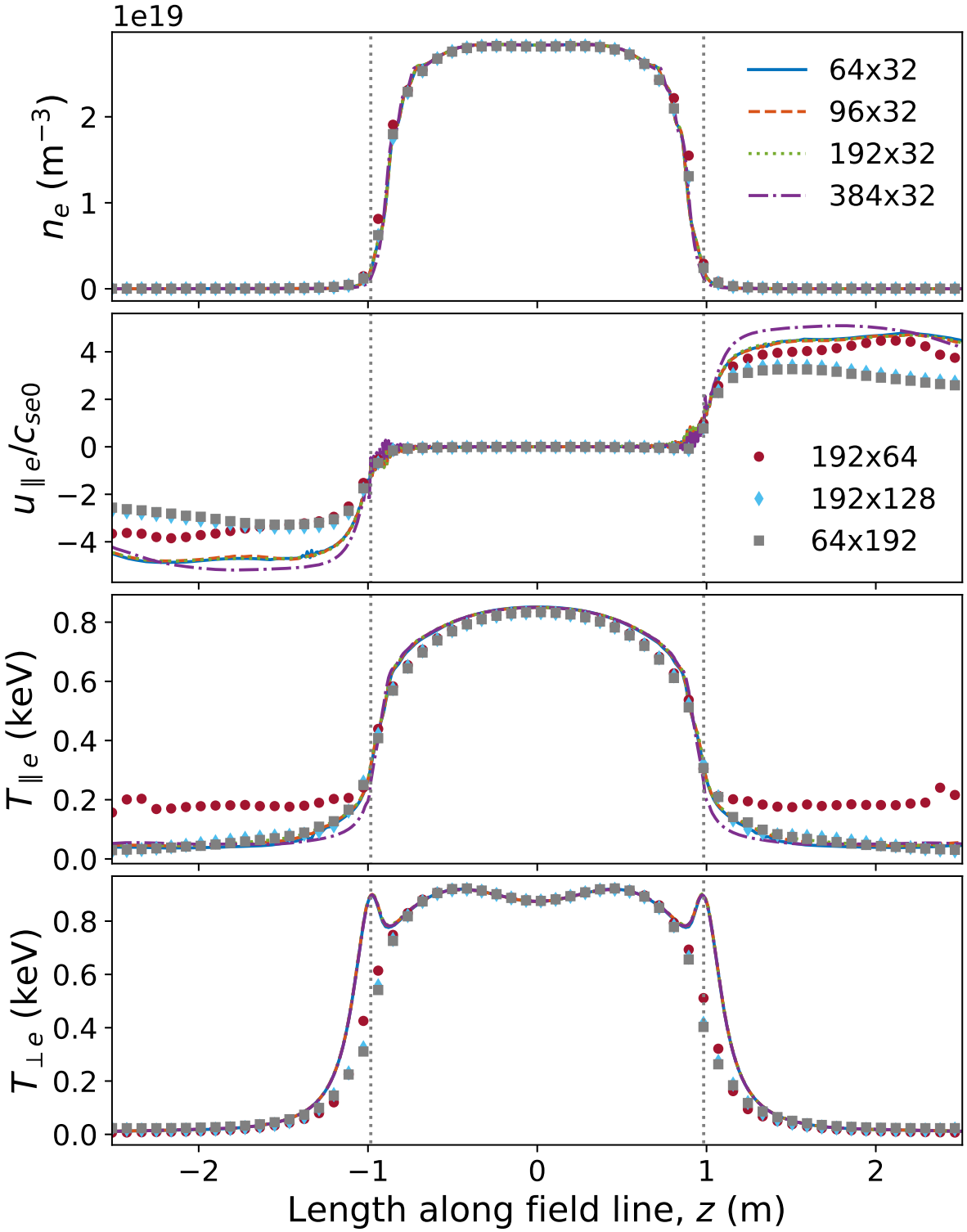
1e19
n_e (m^{-3})
64x32
96x32
192x32
384x32
$u_{\parallel e}/c_{se0}$
192x64
192x128
64x192
$T_{\parallel e}$ (keV)
$T_{\perp e}$ (keV)
Length along field line, z (m)